Institut für Kernphysik
Technische Universität Darmstadt

Beyond the Neutron Drip-Line: Superheavy Oxygen Isotopes

Vom Fachbereich Physik

der Technischen Universität Darmstadt

zur Erlangung des Grades

eines Doktors der Naturwissenschaften

(Dr. rer. nat.)

genehmigte Dissertation von

Dipl.-Phys. Christoph Caesar

geboren in Mainz

Darmstadt 2012

D17

1. Berichterstatter: Prof. Dr. Thomas Aumann
2. Berichterstatter: Prof. Dr. Joachim Enders

Tag der Einreichung: 11.07.2012
Tag der mündlichen Prüfung: 29.10.2012

We have to remember that what we observe is not nature herself, but nature exposed to our method of questioning.

Werner Heisenberg, Physics and Philosophy: The Revolution in Modern Science (1958)
Lectures delivered at University of St. Andrews, Scotland, Winter 1955-56

Abstract

The neutron-unbound ground states of ^{25}O and ^{26}O have been investigated using the LAND-R^{3}B setup at GSI in Darmstadt (Germany). Relativistic secondary cocktail beams of $A/Z \approx 3$ and $Z < 10$ at approximately 450 MeV/u have been produced using fragmentation of a primary stable ^{40}Ar beam on a 4 g/cm^2 Be target and subsequent separation using the FRagment Separator (FRS). After reaching the LAND-R^{3}B setup in Cave C, one-proton-removal reactions, i.e. X(^{27}F,^{26}O)X+p; ^{26}O→^{24}O+2n, were investigated using various targets. The decay products of the unbound ^{25}O and ^{26}O systems have been measured in inverse kinematics using a complex detector system, which allows for kinematically complete measurements including γ-ray detection. Both neutron-rich oxygen isotopes decay via the emission of neutrons, which were detected in the LAND detector. The present analysis concentrates on the relative energy between neutrons and fragments.

Structure has been observed in the 1n-continuum of the ^{24}O+n system, as well as in the ^{24}O+2n relative-energy spectrum. The ^{24}O+n relative-energy spectrum is described using a single resonance, reflecting the ground state. In the ^{24}O+2n relative-energy spectrum two resonances are used to describe the ground state resonance as well as a excited state. For both ground states the lifetimes have been extracted; for the ^{25}O ground state, the lifetime was directly measured via the width of the state, which has been obtained from a fit to the data using a Breit-Wigner line shape in the one-level approximation. For the ^{26}O ground state, an upper limit on the lifetime was determined using the Time of Flight (ToF) from the target to the ALADIN magnet. In summary the obtained results are:

1. ^{25}O ground state: $E_r = 737^{+48}_{-43}$ keV and $\Gamma = 72^{+126}_{-65}$ keV,
2. ^{26}O ground state: $E_r = 25^{+25}_{-25}$ keV,
3. ^{26}O excited state: $E_r = 4225^{+227}_{-176}$ keV,
4. $\tau(^{25}$O; GS$) = 9^{+85}_{-6} \cdot 10^{-12}$ ns and
5. $\tau(^{26}$O; GS$) \leq 5.7$ ns.

Theoretical calculations using chiral Effective Field Theory (EFT) give a perfect agreement with the experimentally determined values for the ground states of both oxygen

isotopes. Two-body (NN) and three-body (3N) interactions have been taken into account. For the three-body part the following contributions have been included: two neutrons are in the ^{16}O-core and one is in the valence space (effectice one-body part); one neutron is in the ^{16}O-core and two are in the valence space (effectice two-body part); and all three neutrons are in the valence space (so called 'residual' part) [Hol12, Sim12].

The ^{25}O and ^{26}O unbound resonances had recently also been investigated by other collaborations [HBB$^+$08, LDK$^+$12]. The location of the ^{25}O ground state resonance given in [HBB$^+$08] and the one presented here agree very well. The width determined in this analysis is smaller by factor of two than the one given in [HBB$^+$08], but it agrees very well with the single-particle width determined using the Breit-Wigner line shape. For ^{26}O, only the resonance position of the ground state had been observed before, while in that experiment an upper limit of 200 keV [LDK$^+$12] has been determined. The data presented here reduces this limit to 50 keV. It furthermore supports strongly that the emitted neutrons from the ^{24}O+n as well as in the ^{24}O+2n system have a pure d-wave character.

A disagreement between theoretical calculations and the here presented analysis can be seen in the position of the excited state in the experimental ^{24}O+2n relative-energy spectrum and the prediction for the first excited state. This discrepancy is most likely found because the excited states which are compared do not have the same origin. The experimentally found excited state is most likely not the first excited state.

The two facts, that first, the ground state of ^{25}O is more weakly bound than the ^{26}O ground state, and second, that the ^{26}O ground state resonance is rather long lived (twelve orders of magnitude compared to $\tau(^{25}\text{O;GS})$, make ^{26}O a true two-neutron decaying nucleus, a property which has been discussed in recent publications [GMSZ11, PKGR12], and which is found for very few nuclei only.

Zusammenfassung

In der hier vorgestellten Dissertation wurden die neutronen-ungebundenen Grundzustände von ^{25}O und ^{26}O untersucht. Dazu wurde das LAND-R^{3}B Experiment an der GSI in Darmstadt (Germany) benutzt. Relativistische Sekundärstrahlen, welche Kerne mit $A/Z \approx 3$ und $Z < 10$ enthielten wurden mit einer Energie von ungefähr 450 MeV/u produziert. Hierzu wurde Fragmentation eines ^{40}Ar Primärstrahls an einem 4 g/cm^2 Be Target und anschließende Separation im FRagment Separator (FRS) benutzt. Vom FRS aus wurden die Strahlen zum experimentellen Aufbau in Cave C weitergeleitet. Ein-Protonen-Knockout-Reaktionen z.B. X(^{27}F,^{26}O)X+p; ^{26}O→^{24}O+2n, wurden an verschiedenen Targets untersucht. Die Zerfallsprodukte der ungebundenen ^{25}O und ^{26}O Systeme wurden unter Zuhilfenahme eines komplexen Systems aus mehreren Detektoren gemessen. Dieses Detektor System erlaubt eine kinematisch vollständige Messung, welche auch das detektieren von γ-Strahlen beinhaltet. Beide neutronen-reiche Sauerstoff-isotope zerfallen mittles der Emission von Neutronen. Diese wurden im LAND Detektor nachgewiesen. Die vorgestellte Auswertung konzentriert sich auf die Bestimmung der Relativenergie zwischen Neutronen und Fragmenten.

Eine Struktur konnte im Ein-Neutronen-Kontinuum des ^{24}O+n Systems beobachtet werden. Auch die ^{24}O+2n Relativenergie Verteilung weist eine Struktur auf. Die ^{24}O+1n Relativenergie Verteilung wurde mit Hilfe einer Resonanz beschrieben, diese spiegelt den Grundzustand des Systems wieder. Zur Beschreibung der ^{24}O+2n Relativenergie Verteilung wurden zwei Resonanzen benutzt um sowohl den Grundzustand als auch einen angeregten Zustand zu charakterisieren. Für die Grundzustände von ^{25}O und ^{26}O wurden jeweils die Lebensdauern bestimmt. Diese ist für ^{25}O direkt mittels der Breite des Zustandes gemessen worden. Die Breite wurde durch den Fit einer Breit-Wigner-Resonanz in der 'Ein-Zustand-Näherung' an die Daten bestimmt. Für den ^{26}O Grundzustand wurde eine obere Grenze für die Lebensdauer, unter Berücksichtigung der Flugzeit eines Ions vom Target zum ALADIN Magneten bestimmt. Eine Zusammenfassung der gewonnen Resultate wird im Folgenden gegeben:

1. ^{25}O Grundzustand: $E_r = 737^{+48}_{-43}$ keV und $\Gamma = 72^{+126}_{-65}$ keV,
2. ^{26}O Grundzustand: $E_r = 25^{+25}_{-25}$ keV,
3. ^{26}O Angeregter Zustand: $E_r = 4225^{+227}_{-176}$ keV,

4. $\tau(^{25}\mathrm{O}; \mathrm{GS}) = 9^{+85}_{-6} \cdot 10^{-12}$ ns und

5. $\tau(^{26}\mathrm{O}; \mathrm{GS}) \leq 5.7$ ns.

Theoretische Berechnungen, auf Grundlage von chiral Effective Field Theory (EFT), stimmen sehr gut mit den experimentell bestimmten Werten für die Grundzustandsenergien beider Sauerstoff Isotope überein.

Zwei-Körper (NN) und drei-Körper (3N) Wechselwirkungen wurden hierbei berücksichtigt. Für den 3N-Anteil wurden folgende Beiträge berücksichtigt: Zwei Neutronen befinden sich im $^{16}\mathrm{O}$-Kern und eines im Valenz-Raum (effektiver Ein-Körper Anteil); ein Neutron befindet sich im $^{16}\mathrm{O}$-Kern und zwei im Valenz-Raum (effektiver Zwei-Körper Anteil); alle drei Neutronen befinden sich im Valenz-Raum (Residual Anteil) [Hol12, Sim12].

Die ungebundenen Resoanzen von $^{25}\mathrm{O}$ und $^{26}\mathrm{O}$ wurden kürzlich auch von anderen Kollaborationen untersucht [HBB+08, LDK+12]. Die bestimmte Lage der $^{25}\mathrm{O}$ Grundzustands-Resonanz von [HBB+08] und die Lage, welche in dieser Doktorarbeit bestimmt wurde, stimmen sehr gut überein. Die Breite der $^{25}\mathrm{O}$ Grundzustands-Resonanz ist in der vorliegenden Arbeit um einen Faktor 2 kleiner als in [HBB+08] angegeben. Die hier bestimmte Breite stimmt gut mit der Ein-Teilchen-Breite überein, welche mit Hilfe der Breit-Wigner-Resonanz bestimmt wurde. Für die $^{26}\mathrm{O}$ Grundzustands-Resonanz wurde zuvor eine obere Grenze von 200 keV [LDK+12] bestimmt. Das hier präsentierte Experiment reduziert diese obere Grenze auf 50 keV. Außerdem legen die hier vorgestellten Ergebnisse die Schlußvolgerung nahe, dass die Neutronen sowohl im $^{24}\mathrm{O}$+n als auch im $^{24}\mathrm{O}$+2n System einen reinen d-Wellen Charakter besitzen.

Die theoretischen Vorhersagen und die hier präsentierten experimentellen Werte stimmen für die Lage des jeweiligen angeregten Zustandes in $^{26}\mathrm{O}$ nicht überein. Dies ist höchswahrscheinlich der Fall, da es sich bei dem im Experiment gefundenen Zustand nicht um den ersten angeregten Zustand handelt.

Die zwei Tatsachen, dass der Grundzustand von $^{25}\mathrm{O}$ weniger stark gebunden ist als der von $^{26}\mathrm{O}$ und das zweitens der $^{26}\mathrm{O}$ Grundzustand eine eher lange Lebensdauer hat (die Lebensdauer dieses Zustandes ist zwölf Größenordnungen länger als die des $^{25}\mathrm{O}$ Grundzustandes), machen $^{26}\mathrm{O}$ zu einem Kern, welcher 'Wahren-Zwei-Neutronen-Zerfall' aufweisen könnte. Dies ist eine Eigenschaft, welche in aktuellen Publikationen diskutiert wird [GMSZ11, PKGR12] und welche nur für sehr wenige Kerne auftritt.

Contents

Chapter 1

Introduction

In May 1911 Ernest Rutherford published his discovery of the atomic nucleus and founded thereby the research field of Nuclear Physics. In 1932 the discovery of the neutron by Chadwick proved that a nucleus is build of neutrons and protons. In the past hundred years, scientists have addressed several questions concerning these building blocks of nuclei, and many experiments have led to a deeper understanding of the nucleus and the nuclear force, but there are still questions, which have not been fully answered yet [TS11], such as:

- How forces hold together protons and neutrons?
- How many neutrons can be bound in a nucleus for a given number of protons?

To address these questions it is of particular interest to investigate nuclei with large proton to neutron asymmetries. In this thesis, neutron-rich oxygen isotopes are investigated. Their particular importance is highlighted within the following two citations:

1. *'The limit of neutron-rich nuclei, the neutron drip line, evolves regularly from light to medium-mass nuclei except for a* **striking anomaly** *in the oxygen isotopes'* [OSH+10]. This feature of nuclear structure was first pointed out 1999 in a Letter by Sakurai *et al.* [SLN+99], in which *'the sudden change in stability from oxygen to fluorine'* was reported.

2. *'Therefore, ^{24}O is* **truly remarkable** *because it is hard to excite, implying that it is doubly magic and very tightly bound. But it is located at the very limits of nuclear existence, as the addition of even a single neutron is not possible'* [Jan09].

The region in the nuclear chart surrounding the neutron-rich oxygen isotopes is of particular interest from an experimental as well as from a theoretical point of view.

In the last 30 years, huge experimental efforts have been undertaken to gain insight into the nuclear structure of neutron-rich oxygen isotopes. In 1985, Langevin *et*

al. [LQB$^+$85] found that ^{25}O is unbound. As experimental technique in-flight identification of fragmentation products of a ^{40}Ar beam impinging on a tantalum target has been used. Five years later, Guillemaud-Mueller *et al.* [GJK$^+$90] showed that ^{26}O is unbound as well. The experiment was conducted using a ^{48}Ca beam and a tantalum fragmentation target. Finally, in 1997, it was shown that even ^{28}O, a nucleus which in a simple shell-model picture is doubly magic (Z=8, N=20), is particle-unstable [TAA$^+$97]. From then it took 10 years until the first spectroscopy of a neutron-rich oxygen isotope beyond the neutron drip line has been performed. Hoffman *et al.* [HBB$^+$08], found that ^{25}O is unbound by 770 keV. In 2009 it was experimentally shown that ^{24}O is doubly magic [Jan09, HBB$^+$09, KNP$^+$09]. This experimental finding implicates a shift of the magic numbers, as discussed later. The heaviest unbound nucleus for which a resonance has been measured so far is ^{28}F [CFA$^+$12a, CFA$^+$12b]. Very recently Lunderberg *et al.* [LDK$^+$12] populated the ^{26}O ground state via proton knockout from ^{27}F, and they found that ^{26}O is unbound by (150^{+50}_{-150}) keV, placing its ground state below the ^{25}O ground state.
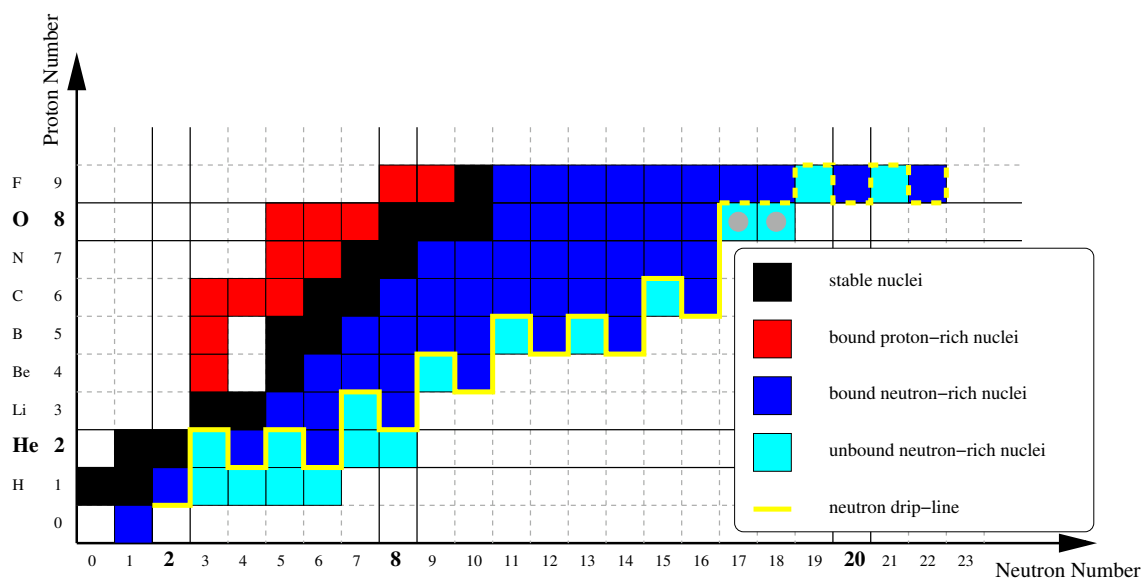

Figure 1.1: Shown is a section of the chart of nuclides. Stable nuclei are indicated by black squares. Neutron-rich nuclei by blue and proton-rich by red squares. The experimentally verified neutron drip line is shown as a yellow solid line (up to the oxygen isotopes) while the status for fluorine isotopes which has not been determined in experiments yet is indicated as a yellow dashed line. Unbound neutron-rich nuclei are represented by cyan squares. The two nuclei of particular interest within the framework of this thesis, namely ^{25}O and ^{26}O are marked by grey dots. The 'classic' magic numbers are highlighted by the solid black vertical and horizontal lines and bold numbers.

As discussed in [OSH$^+$10], shell-model calculations, based on a microscopic nucleon-nucleon (NN) force, predict ^{28}O to be bound and determine thereby wrongly the location

of the neutron drip line.

The neutron drip line is experimentally still only verified for elements up to oxygen [BST12], as shown in figure 1.1. In theoretical calculations the exact course of the neutron drip line is difficult to predict. In a Nature article from 2007 [BAB$^+$07] it is e.g. stated, that the experimental proof for the existence of two neutron-rich nuclei (^{40}Mg and ^{42}Al) *'suggests neutron drip line slant towards heavier isotopes'*. To test theoretical calculations, nuclei with an extreme proton-to-neutron ratio are especially important, because they put the most strict constraints on those theories. Therefore, it is very important to expand the study of nuclei even to nuclei beyond the neutron drip line [BST12].

The next paragraph will discuss why neutron-rich oxygen isotopes are 'special' from a nuclear-structure point of view.

The Nuclear Shell Model developed by Goeppert-Mayer [May48] and Jensen [JSH49] gives an intuitive picture of the structure of atomic nuclei. In this picture each nucleon moves independently in a mean field, which is created by all other nucleons. From this model one gains, analogously to the atomic shell model for the electrons, single particle orbits. These are the so called SPE*s. This basic picture of nuclear shell structure leads to the concept of magic numbers (Z and/or N = 2, 8, 20,...), meaning that a shell-closure leads to enhanced stability because the energy gap to the next available shell is large. In reality, the location of a certain energy level depends on the occupation number of other energy levels. This effect is included in the ESPE†s which can explain changes of nuclear structure as a function of the A to Z ratio. In figure 1.2, the ESPEs of neutrons are shown as a function of the proton number Z (from oxygen to calcium) for the N=20 isotones. It can be seen that while for the stable nucleus ^{40}Ca N=20 is a magic number the magic number is 'shifted' for the unbound-neutron-rich ^{28}O to N=16.

This effect is due to the fact that for nuclei far from stability the highest occupied neutron (ν) and proton (π) orbitals have very different quantum numbers. If a stable nucleus has neutrons which occupy the $\nu d_{3/2}$ shell, there are also protons which fill the $\pi d_{5/2}$ proton shell. This very attractive $\pi d_{5/2}$ - $\nu d_{3/2}$ interaction is missing for the neutron-rich oxygen isotopes. This can be summarized citing the following sentence from Jensens 2009 Nature article [Jan09]: *'...it seems that, as soon as protons occupy the $0d_{5/2}$ orbital (as happens when going from O to F), the gap between the neutron $1s_{1/2}$ and $0d_{3/2}$ shells decreases significantly, an indication that a tensor force - an especially attractive, spin-dependent force between protons and neutrons - is providing the additional binding.'*

The following paragraph reviews briefly how the inclusion of three-body forces in chiral EFT‡ can explain the so called 'oxygen anomaly' [OSH$^+$10] for the first time

---

*Single Particle Energy
†Effective Single Particle Energy
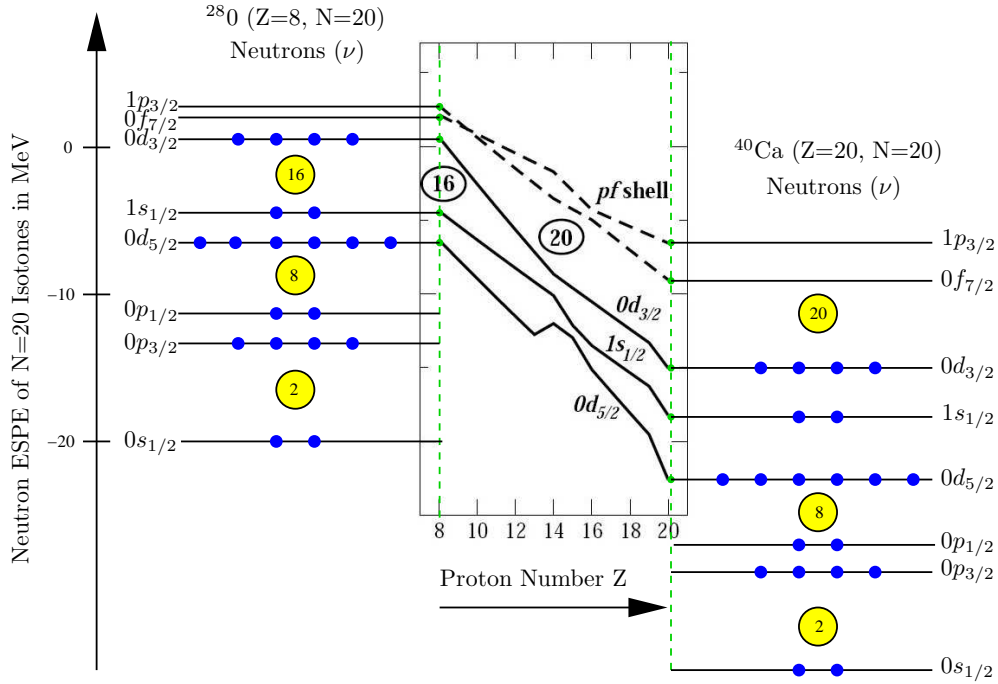‡Effective Field Theory

Figure 1.2: Shown are the neutron ESPEs of N=20 isotones for Z=8 to 20. Magic numbers are indicated by numbers in yellow circles. The middle part of the figure is taken from [OUF+02], the idea of the drawing is adapted from [Sch11].

giving a microscopic explanation.

In figure 1.3 (a), the neutron ESPEs derived from nucleon-nucleon (NN) interactions are shown as function of the neutron number N for oxygen isotopes (Z=8). Following the x-axis it is indicated by colored dots in which corresponding ESPE the new added neutron has to be filled to create the next, more neutron-rich, oxygen isotope. As long as ESPE<0 added neutrons are bound within the nucleus. As seen in figure 1.3 (a), for that type of calculation this is possible even up to ^{28}O. To correct for this wrong prediction, empirical forces can be used as shown in figure 1.3 (b). The there shown energy levels reflect very well two experimental findings:

1. The opening between the $\nu 0d_{5/2}$ and $\nu 1s_{1/2}$ levels which corresponds to the experimentally found doubly magic ^{22}O ([BR05] and references therein).

2. The ESPE of the $\nu 0d_{3/2}$ level is positive, which means that ^{24}O is the heaviest bound oxygen isotope.

However, the shown results are not obtained using ab-initio calculations, they use empirical forces which are derived from a fit to experimental data measured for neighboring nuclei. Results, which are obtained from a theory, which gives as the first one a microscopic picture and predicts that ^{24}O is the last bound Oxygen isotope [OSH+10] are
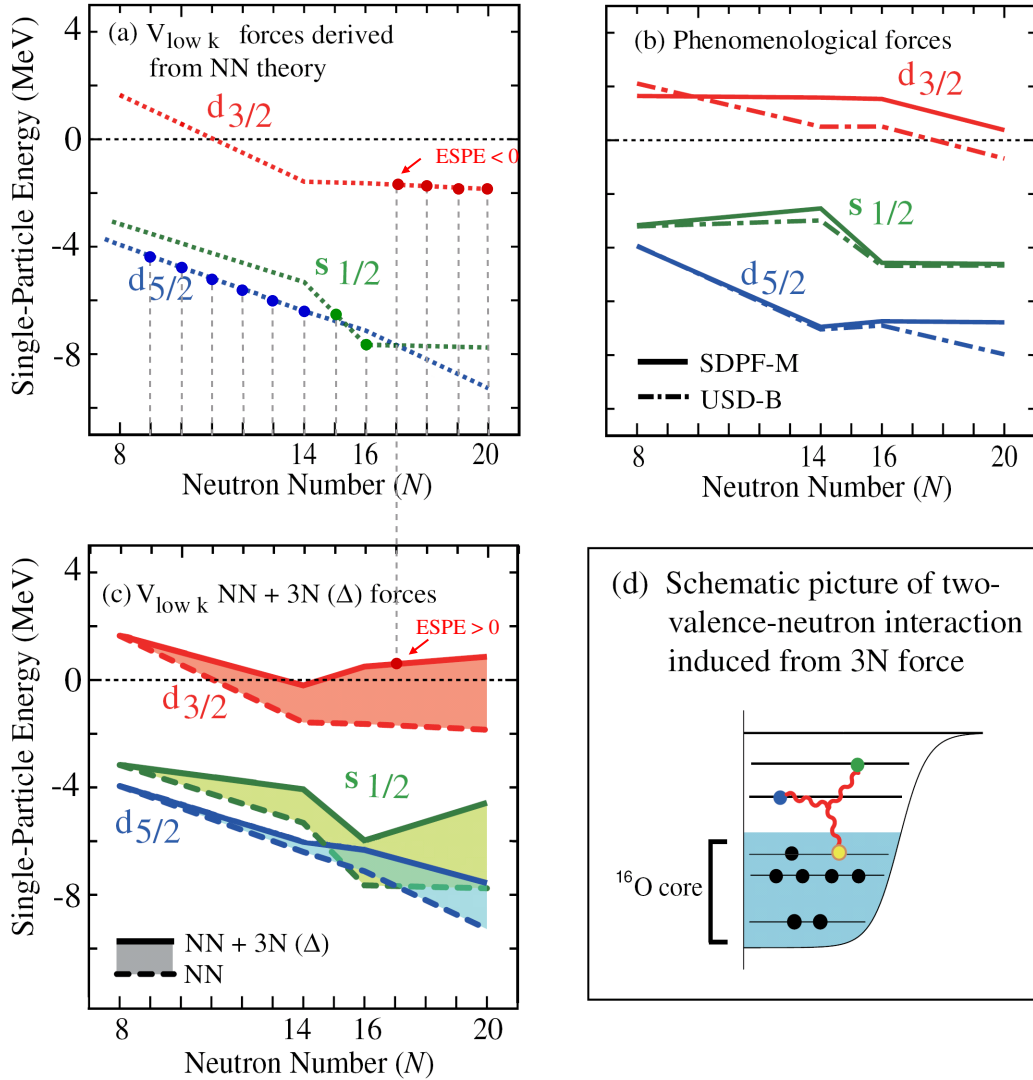
Figure 1.3: In (a),(b) and (c) neutron ESPEs are shown as a function of the neutron number N for oxygen isotopes (Z=8). (d) shows a schematic picture of two-valence-neutron interaction induced by 3N forces with a nucleon in the ^{16}O core. Details are discussed in the text. Figures are adapted from [OSH$^+$10].

shown in figure 1.3 (c). The dashed lines are the same as the dotted once shown in figure 1.3 (a), while the shaded area highlights how the neutron ESPE changes if three-body (3N) forces are included. The calculations shown here include contributions from chiral low momentum interactions ($V_{\text{low k}}$), including the changes due to Δ excitations. The three-body mechanism due to Δ excitations can be pictured in the following way, one nucleon virtually excites a second nucleon to the Δ resonance, which is deexcited by scattering off a third nucleon.

Figure 1.3 (d) represents a visualization of those three-body interactions: one nucleon belongs to the ^{16}O-core and the other two are valence nucleons. Those 3N forces, amongst two valence neutrons and one nucleon in the ^{16}O core give rise to the repulsive interactions between the valence neutrons, which make the ^{25}O unbound.

Including three-body interactions amongst three valence neutrons is a topic of current research. Contributions from three valence-nucleon interactions are in general suppressed by $\sim N_{valence}/N_{core}$ [FS11], those contributions will therefore only be important in the most neutron-rich nuclei. Making this effect significant for the here discussed oxygen isotopes. New calculations performed by Holt *et al.* [Hol12] and Simonis *et al.* [Sim12] will be discussed in chapter 6 and 7, see, e.g., figure 7.2. Those calculations include contributions from interactions amongst three valence neutrons and predict the ^{26}O ground state energy correctly.

Chapter 2

The NeuLAND Time-of-Flight Neutron Spectrometer

The investigation of short-lived radioactive nuclei has to be done in inverse kinematics, since targets for scattering experiments cannot be produced. This makes it necessary to produce radioactive beams with sufficient intensities. Two techniques are used to produce RIB*s: ISOL† and 'in-flight'. The in-flight technique was invented in the 1970s at LBNL‡ [Ct05]. Since the 1990s more neutron-rich nuclei are produced via in-flight fission or projectile fragmentation of high-energy heavy ion beams, due to higher-energy accelerators [TS11]. The main in-flight RIB facilities and their separators nowadays which produce high-energy beams via fragmentation are for example: FRS§ at GSI¶, Germany; RIPS‖ at RIKEN**, Japan; A1900 at NSCL††, USA; SISSI‡‡ at GANIL§§, France; Acculinna at FLNR¶¶, Russia [PKGR12]. As discussed in the previous chapter there is an urgent need to investigate nuclei far from stability. To be able to cover these exotic parts of the nuclei chart several second-generation facilities are being constructed. The first of these facilities, the RIBF***, started operation in 2007 in Japan, having BigRIPS as the successor of the above mentioned RIPS. Other research centers which are currently in the development stage are:

---

*Radiactive Ion Beam

†Ion Source On Line

‡Lawrence Berkeley NationalLaboratory

§FRagment Seperator

¶Gesellschaft für SchwerIonenforschung

‖RIKEN Projectile Fragment Separator

**The Institute of Physical and Chemical Research, japanese abbreviation

††National Superconducting Cyclotron Laboratory

‡‡Superconducting Intense Source for Secondary Ions

§§Grand Accélérateur National d'Ions Lourds

¶¶Flerov Laboratory of Nuclear Reactions

***Rare Isotope Beam Factory

- FAIR* in Darmstadt, Germany,
- SPIRAL†2 in Caen, France,
- FRIB‡ at MSU§ in East Lansing, USA.

The experiment and developments discussed within this thesis have been conducted at GSI. FAIR can be understood as a major upgrade of the nowadays GSI accelerator and experiments. Within the transition from GSI to FAIR the LAND¶-ALADIN‖ experimental setup will be replaced by the R^3B** experimental setup, whose start version is schematically displayed in figure 2.1. Its main components are as highlighted in the figure: the R^3B-Si-Tracker, the γ calorimeter CALIFA††, the superconducting magnet GLAD‡‡ and NeuLAND§§. The currently used setup is commonly called LAND-R^3B-setup, indicating the transition phase from GSI to FAIR. This name will also be used in this document.

The R^3B collaboration is part of NuSTAR¶¶, the reader is referred to [RCb] and [Aum07] for the full physics programs of R^3B and to [NC] for other physic topics covered by NuSTAR.

The different experimental equipment which is currently being developed for R^3B is shown in figure 2.1. One of the major components amongst the developments is NeuLAND, this detector is the successor of LAND, which will be described in detail in section 3.3.2. In table 2.1 the design goals for NeuLAND are given as well as a comparison to the existing LAND. Based on the experience with LAND during the past 20 years, two different design concepts have been investigated during the R&D*** phase of NeuLAND:

1. MRPC††† based detector concept (converter-based design).
2. Scintillator based detector concept (fully active design).

The fully active detector design, based on a highly granular plastic scintillator concept has turned out to be superior to the MRPC concept. It turned out, that its additional calorimetric properties offer a significant advantage concerning multi-neutron recognition [Bor11].

---

*‾F‾acility for A‾ntiproton and I‾on R‾esearch
†S‾ystème de P‾roduction d'I‾ons R‾adioactifs A‾ccélérés en L‾igne, in engl. System for Producing Online Accelerated Radioactive Ions
‡F‾acility for R‾are I‾sotope B‾eams
§M‾ichigan S‾tate U‾niversity
¶L‾arge A‾rea N‾eutron D‾etector
‖A‾ Large A‾cceptance DI‾pole magN‾et
**R‾eactions with R‾elativistic R‾adioactive B‾eams
††CAL‾orimeter for the I‾n F‾light detection of γ rays and light charged pA‾rticles
‡‡GSI‾ L‾arge A‾cceptance D‾ipole
§§N‾eu(engl. new) L‾arge A‾rea N‾eutron D‾etector. Successor of LAND
¶¶N‾uclear ST‾ructure, A‾strophysics and R‾eactions
***R‾esearch & D‾evelopment
†††M‾ulti-gap R‾esisitve P‾late C‾hamber

		NeuLAND	
	LAND	MRPC-Concept	Scintillator-Concept
Paddle Dimensions	$(10 \times 10 \times 200)$ cm^3	$(10 \times 50 \times 200)$ cm^3 [a]	$(5 \times 5 \times 250)$ cm^3
Number of Channels	400	1600	6000
Material	Iron Converter (5 mm)+Scintillator	Iron Converter (4 mm)+MRPC	Scintillator
Readout	PMT[b]+FaBu[c]	FOPI[d]FEE[e]+TacQuila	PMT+LANDFEE+TacQuila
Depth of Full Detector	1 m	≈ 1 m	≈ 3 m
Angular Acceptance	80 mrad @ $\sim$ 12 m	80 mrad @ $\sim$ 12 m	80 mrad @ $\sim$ 15.5 m
Time Resolution	$\sigma \sim 250$ ps	$\sigma < 150$ ps	
Position Resolution	$\sigma = 7$ cm	$\sigma \approx 1.5$ cm	
1n Efficiency	$\approx 90\%$ @ 400 MeV	$\approx 95\%$ @ 400 MeV	
Multi-Neutron Recognition	$\approx 10\%$ for 4n	$\approx 60\%$ for 4n	
Distance: Detector-Target	≈ 12 m	R^{3}B-Cave: 15-35 m	

Table 2.1: The characteristics of the existing LAND are compared to the two concepts of NeuLAND. The values given for NeuLAND represent the design goals. The multi-neutron recognition depends strongly on the neutron emission scenario and the details of the experimental setup. The value for LAND is taken from [Ebe98] and corresponds to an α+4n case. The design goals of NeuLAND are verified using simulations, e.g. one with the following conditions: Neutrons were simulated with 600 MeV, NeuLAND was located at a distance of 15.5 m to the target, neutrons were generated with a relative energy of 500 keV with respect to a medium heavy projectile fragment [Bor11]. The value given here corresponds to this scenario.

[a] paddles are segmented in 2.5 cm wide strips.
[b] Photo Multiplier Tube
[c] Fast Bus (electronics), LeCroy digitizers
[d] FOur PI experiment
[e] Front End Electronics
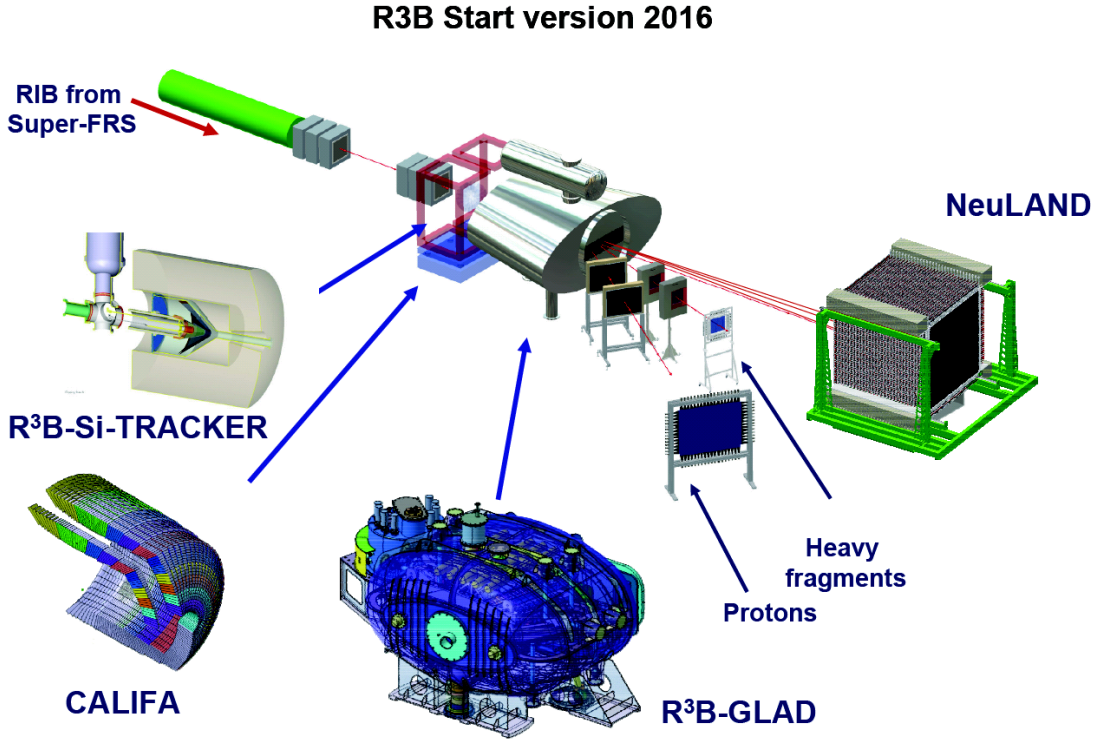
R3B Start version 2016

Figure 2.1: Shown is the start version of the R^{3}B setup. The figure is taken from [Bor11].

After NeuLAND has been completed spectroscopy of certain neutron-rich, unbound systems beyond the neutron drip line will be possible for the first time. Amongst those ^{28}O is one of the key nuclei, which could be populated via proton knockout from a ^{29}F beam. This beam will be available with high intensities at FAIR. The experimental challenge is to reconstruct the relative energy of the 5 body decay, which requires the detection of four neutrons, which are emitted with small relative energy. NeuLAND with its high 4n efficiency and its high resolving power will enable these kind of studies.

One main part of the here presented work was performed within the NeuLAND working group. In particular MRPC prototype tests and implementation of new readout electronics have been carried out. These two subjects will be briefly discussed in the following two sections.

2.1   MRPC based Neutron Detector Concept

In the R&D phase one possible design of NeuLAND, consisting of a layered structure of passive converting material (iron) and active detectors, was investigated. The detection principle then relies on neutrons inducing reactions in the iron converter. Charged particles (mainly protons) from these reactions are detected subsequently in MRPC detec-

tors. The usage of a converter to create charged particles from the neutron interactions is adapted from the LAND design.

Before detailing the MRPC design and prototype tests for NeuLAND a short review about the principle of an RPC* is given. The precursor of a RPC is a PPC†. This detector type consists of two electrodes limiting a gas volume. A charged particle which crosses this volume creates electron-ion pairs. If the field is high enough an avalanche is created leading to a sizable voltage change. The fast drifting electrons produce a prompt signal which is very well suited for timing purposes. In this simple detector design the problem occurs, that on one side a higher field is desired to get faster response but on the other side this leads to a longer recovery time (deadtime) due to the larger amount of charge released [Gon06].

To improve the detector design a highly resistive material (glass) is inserted in the plate chamber [PPP71, SC81]. This new detector type is called RPC, and offers the possibility to work at very high fields while avoiding its breakdown as result of an avalanche. The resistive plate is essentially transparent to the induced signal. The signal is measured with pickup strips, separated from the HV foil. The HV has to be applied through a non perfect conductor in order to be transparent to the induced signal. The first two-gap RPC was developed in 1988 [CSdL88] leading to an increase in efficiency and being the first so called MRPC.

Using MRPCs, several test experiments have been conducted during the NeuLAND R&D phase, at e.g. KVI‡ Groningen, using proton beams [Ros09], HZDR§ Dresden, using electron beams (ELBE¶) [YBR12, YAB+11], and TSL∥, Uppsala, using neutron beams [CAB+12]. Prototypes have been built in different member-institutes of the NeuLAND working group, namely GSI, HZDR and SINP**.

Results on the GSI-MRPC-prototypes tested at ELBE, Dresden can be found in appendix C. A short description of the experiment performed at TSL, Uppsala in November 2009 will be given in the following paragraph.

A quasi-monoenergetic neutron beam with an energy E_n=175 MeV was directed onto a 2×4 gap prototype operated at E=100 kV/cm. The neutron energy of 175 MeV used during this experiment is at the lower limit of the energy range (0.2 - 1) GeV for which the future detector is designed for. The experiment had two goals, on the one hand it aimed to proof that an RPC can be used to detect high-energy neutrons at all (this has never been done before), and on the other hand the neutron detection efficiency of the MRPC prototypes should be determined. In total, eight different detectors were tested

---

*Resistive Plate Chamber
†Parallel Plate Chamber
‡Kernfysisch Versneller Instituut
§Helmholtz-Zentrum Dresden-Rossendorf
¶Electron Linac for beams with high Brilliance and low Emittance
∥The Svedberg Laboratory
**Saha Institute of Nuclear Physics

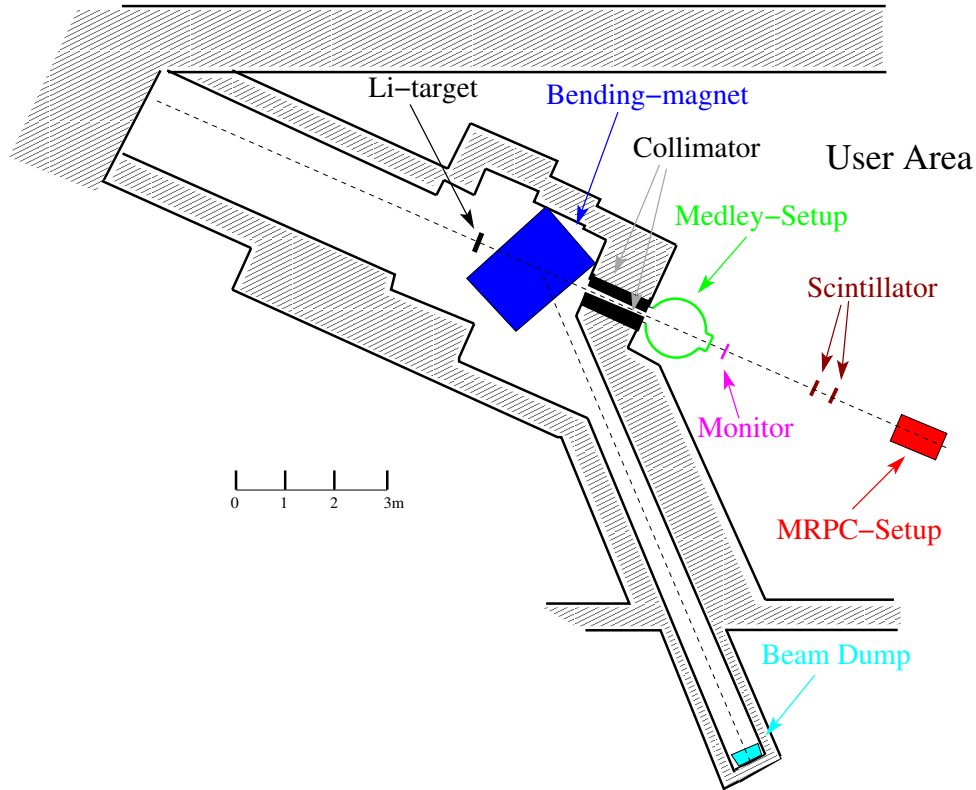investigating different designs and readout schemes.

Figure 2.2: Schematic layout of the experimental setup at the TSL neutron-beam facility [PBB+07]. The neutron production system, the proton beam dump, the neutron collimation, the position of the MEDLEY [DAB+00] and MRPC setup are shown.

A schematic layout of the experimental setup at the TSL neutron beam facility is shown in figure 2.2. A proton beam from the Gustaf Werner cyclotron was used to produce neutrons via the ^{7}Li(p,n)^{7}Be reaction (Q=-1.64 MeV). The used lithium target was 23.5 mm thick. The proton-beam current on target was typically in the range of 280 - 370 nA. The proton energy-loss in the target amounts to 2.5 MeV. Thus, the energy of the primary proton beam of 179.0 ± 0.8 MeV results in a peak-energy for neutrons of ~ 175 MeV. The produced neutron beam is shaped by a system of collimators with a cylindrical and a conical design. The collimator limits the maximum size of the beamspot at the detector position (11 m downstream of the target) to a radius of 5 cm. The remaining proton beam is bent into a beam-dump tunnel after the lithium target by a dipole magnet. The experimental area extends from about 3 to 15 m behind the neutron production target. The relative neutron beam intensity is monitored by the integrated proton beam current at the beam dump and by TFBC* [JPST01]

---

*Thin Film Breakdown Counters

mounted in the neutron beam. Another monitoring option is provided by an ICM*. Both monitors utilize neutron-induced fission of ^{238}U with the cross section adapted as neutron flux standard [PBB$^+$07]. A typical neutron rate at the detector position was ~ 4 kHz/cm^2. The long neutron flight path in the experimental area allows for several irradiation positions. The permanently installed MEDLEY [DAB$^+$00] and the MRPC setup used the neutron beam simultaneously. The MRPC setup was placed such that the first detector was 11 m behind the lithium target.
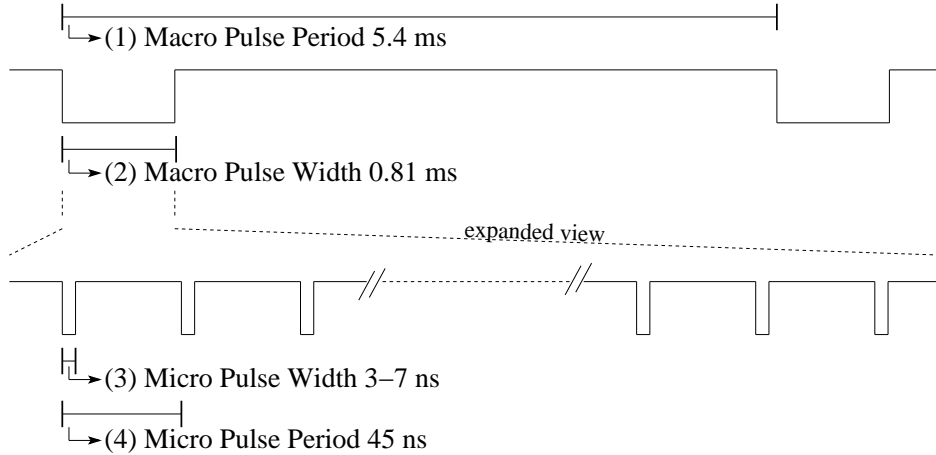
Figure 2.3: The time structure of the primary proton beam, which defines also the time structure of the secondary neutron beam is schematically shown.

The time structure of the neutron beam is defined by the time structure of the proton beam from the cyclotron. The beam has a macro-structure with a repetition rate of 185 Hz and a beam pulse duration of ~ 810 μs. Furthermore, the beam has a microstructure with a repetition period of 45 ns and a pulse duration of 3-7 ns. The uncertainty in the latter is the main contribution to the uncertainty in the measured neutron ToF†. For a visualization of the beam structure see figure 2.3. During the setup phase of the experiment two scintillators were mounted in front of the MRPC holding structure to characterize the beam (see figure 2.2). For the final characterization of the prototypes these scintillators have been removed, since the impinging neutrons would create charged particles contributing to the background.

Figure 2.4 shows the scheme of a 2×4 gap MRPC prototype built at GSI. The readout-electrodes are built from massive iron plates which serve as neutron converters at the same time. A single-ended readout was chosen, hence only the middle electrode is structured dividing the detector in 8 strips.

A thin film of conductive coating on each outermost glass plate was used to apply the high voltage. The chamber was operated at 12 kV (E=100kV/cm). Each strip is

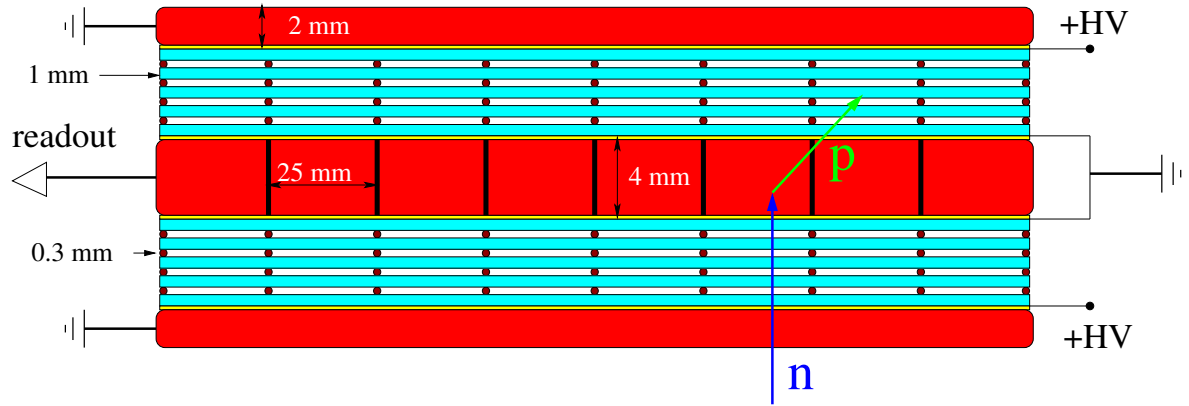---

*Ionization Chamber Monitor
†Time of Flight

Figure 2.4: Schematic representation of the MRPC prototype (not on scale). Red=iron, light-blue=float-glass, yellow=capton-foil, brown-circles=spacer (fishing line), white=gas-gap. The central iron converter is divided into eight read out (pick up) strips as indicated by the vertical black lines. The blue arrow symbolizes an incident neutron which creates a secondary proton (green arrow) via an reaction in the iron converter.

2.5 cm wide and 40 cm long. The strips are separated by 1 mm thick GRP* material. A standard gas mixture was used (85% $C_2H_2F_4$ + 10% SF_6 + 5% iso - C_4H_{10}). For a more detailed description of the MRPC prototypes see [Bor11]. The FOPI FEE card [CSC+07] was used together with a V1290N CAEN TDC[†], a V965 CAEN QDC[‡], and a V1495 CAEN FPGA[§] (used as scaler and trigger logic) to read out the prototypes.

As a first analysis step the neutron energy spectrum was reconstructed using the ToF method. The result is shown in figure 2.5. In an earlier experiment at TSL [PBB+07] the neutron energy spectrum was measured at 142.7 MeV and compared to model calculations folded with the experimental response. This theoretical curve has been extrapolated to 175 MeV (see blue circles in figure 2.5) and used for comparison to the measurement presented here, neglecting the differences in the experimental response, e.g. time resolution. Overall, a good agreement between the spectra is found.

The difference in the low-energy part can be explained with two effects:

- The ToF measurement is limited to a maximum time by the required coincidence between the detector and the beam signals.
- The efficiency of the counter decreases for lower energies. This is the case because the energy of a substantial part of the secondary charged particles, created in the iron, is too low to pass the iron and reach the active volume of the MRPC.

From the good reproduction of the neutron energy distribution for the fast neutrons,

---

[*]Glass-fibre Reinforced Plastic
[†]Time to Digital Converter; TDC = TAC+ADC
[‡]charge (Q) to Digital Converter
[§]Field Programmable Gate Array
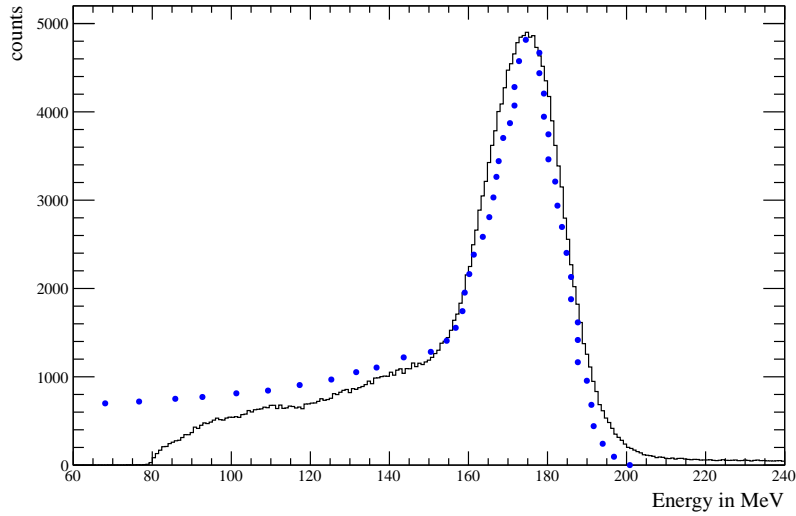
Figure 2.5: The neutron energy, reconstructed from the time of flight is shown. Continuous line ≡ measured, blue circles ≡ adapted theoretical spectrum from [PBB+07].

it is concluded that an MRPC may be used as a time-of-flight wall for high energetic neutrons.
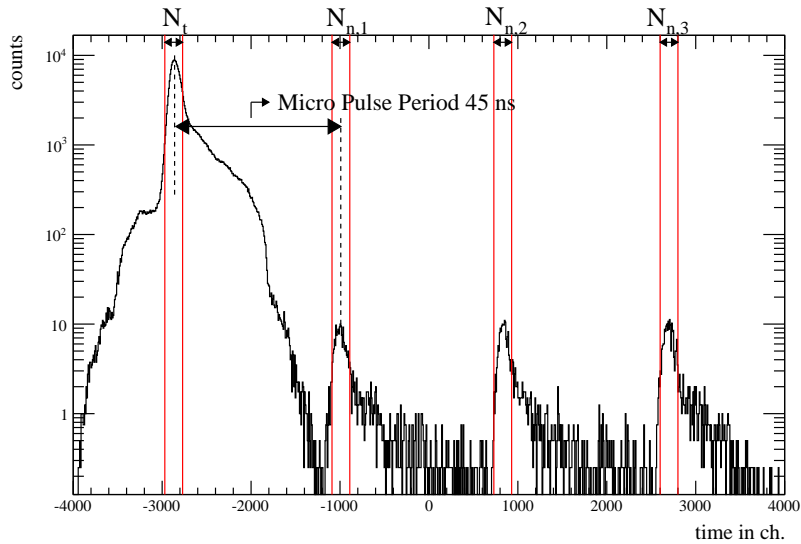

Figure 2.6: Mean time spectra of one RPC strip. The width of one channel is 25 ps, therefore the range represents exactly the 200 ns time window of the TDC. The four observed peaks correspond to four beam micropulses within the 200 ns.

The detector tests reported here were done in parasitic mode. Due to that, the neutron beam intensities could not be adjusted to the data taking capabilities. Therefore,

the dead time of the data acquisition becomes an issue. As a solution to this problem the following procedure was used to determine the efficiency. The TDC window was set to 200 ns. Within this time, the (multi-hit) TDC records data dead time free. Four beam micropulses take place within 200 ns, shown in figure 2.6. The first dominant peak represents events which caused a trigger. For the trigger a coincidence between the 'Macro-Pulse-ON-signal' and the 'MRPC-OR-signal' was used. The second, third and fourth peaks represent neutrons which arrive later at the detector and which are correlated with later beam micropulses. In the following, these events will be called *detected neutrons* while those corresponding to the first peak will be called *triggers*. The ratio of the integral of one of the *detected neutrons*-peaks (N_n) to the integral of the *triggers*-peak (N_t) represents the probability for detecting a neutron per beam micropulse. Dividing this by the number of neutrons per beam micropulse (N_{nm}) leads to the efficiency (ε) of the counter. This is represented by the following formula:

$$\varepsilon = \frac{\frac{N_n}{N_t}}{N_{nm}} \ , \tag{2.1}$$

N_t and N_n are obtained from the timing spectra, see figure 2.6. The latter one can be determined independently for the three detected neutron peaks, reducing the statistical error. The number of neutrons per beam micropulse is obtained using:

$$N_{nm} = \frac{A_i \cdot F_n}{N_{MP}} \ , \tag{2.2}$$

with :

- $F_n \equiv$ neutron flux at detector position in Hz/cm^2,
- $A_i \equiv$ irradiated area on the detector in cm^2,
- $N_{MP} \equiv$ number of beam micropulses per second.

Combining formulae (2.1) and (2.2) leads to:

$$\varepsilon = \frac{N_n \cdot N_{MP}}{N_t \cdot A_i \cdot F_n} \ , \tag{2.3}$$

N_{MP} is given by the beam structure and amounts to 3.3 MHz. The neutron flux (F_n) at the detector position is obtained using the information of the neutron monitors. A_i is, for each strip, derived from the beam profile at the MRPC detector, see figure 2.7. The vertical position of a hit is directly given by the fired strip, however, in the analysis smeared out over the 2.5 cm width of the strip. Using the time difference between the left and right signals, the horizontal position of the hit is determined and, using both, the beam profile is reconstructed. A signal velocity of 20 cm/ns is used for this purpose. The result is shown in figure 2.7. The reconstructed beam profile is in good agreement with the expected beam diameter of 10 cm defined by the collimator.
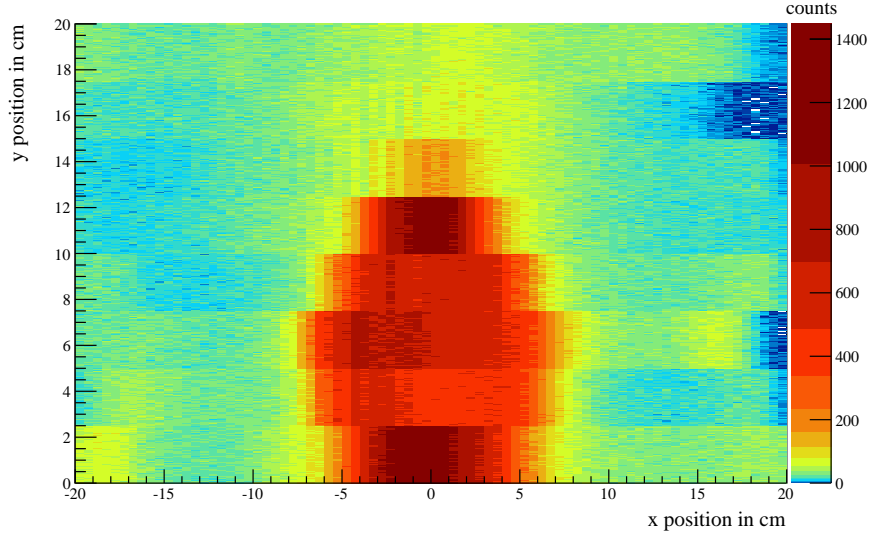
Figure 2.7: Beam profile as reconstructed from the position information of the MRPC.

The result of the efficiency analysis is summarized in table 2.2. The efficiency was determined for the lower five strips, ranging from $\sim (0.6$ to $1.1)\%$. The three upper ones were not sufficiently irradiated (see figure 2.7).

strip	1	2	3	4	5	average
efficiency in %	1.00	0.57	0.62	0.59	1.07	0.77

Table 2.2: Results of the strip-wise efficiency determination.

Figure 2.8 shows a typical charge spectrum of one MRPC channel. The black line represents the raw data. For the spectrum represented by the red line, a valid time entry is required. The sharp rise is attributed to the TDC threshold, indicated as a vertical red, dashed line. Figure 2.8 shows the strong influence of the threshold on the efficiency. Different threshold settings for the individual strips are identified as the major contribution to the variations found for the extracted efficiencies, as given in table 2.2.

For the error estimation, the following effects are taken into account:

- difference in efficiency between left and right readout of the same strip (10%).
- difference in efficiency between strips due to different effective threshold settings (40%).
- uncertainty in neutron flux given by n-monitors (10%).

The different errors are added quadratically. This leads to an efficiency of: $\varepsilon \sim (0.77 \pm 0.33)\%$.

From GEANT*4 simulations, an efficiency of $\sim 2.5\%$ [Ele09] was predicted for an MRPC prototype exposed to 175 MeV neutrons. Since the efficiency of the prototype to charged particles is $\sim 100\%$, this value is mainly reflecting the conversion of neutrons to charged particles. However, the simulation does not include experimental effects such as thresholds of the readout electronics.
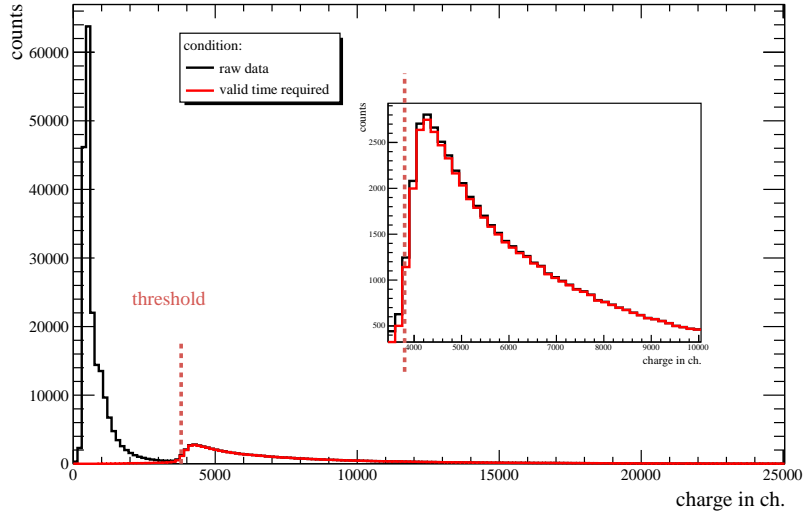

Figure 2.8: A typical charge spectrum of one MRPC channel is shown. The black line represents the raw data, while for the data shown in red a valid time is required. The TDC threshold is indicated as red dotted, vertical line. The inlay represents a zoom, depicting the threshold.

Although, NeuLAND will finally be build from fully active scintillator material, the response of MRPC neutron detector prototypes to fast neutrons will be further investigated using quasi monoenergetic neutrons at various energies, derived from the quasifree break-up reaction of a deuteron beam on a CH_2 target in an GSI experiment scheduled for autumn 2012. Efficiencies, as well as time resolutions shall be studied, and a final characterization of the MRPC prototypes will be performed.

2.2 Readout Electronics for NeuLAND

Besides the detector itself also new readout electronics have been developed to improve the performance of NeuLAND. The new readout electronic is based on the TacQuila board. The TacQuila board is an electronic readout board developed by GSI (K. Koch) for the FOPI experiment [KHS$^+$05]. The most remarkable characteristic of the board is

---

*<u>GE</u>ometry <u>AN</u>d <u>T</u>racking

the excellent time resolution of $\sim$10 ps sigma. A modified version (called TacQuila[17] because of its additional 17th channel) is from now on used in the LAND-R^{3}B-experimental setup. The TacQuila-electronic is composed out of four different electronic boards. These boards replace a whole set of other electronics like e.g.: preamplifier, splitter, multiplexer, sum-units, TDC and QDC.
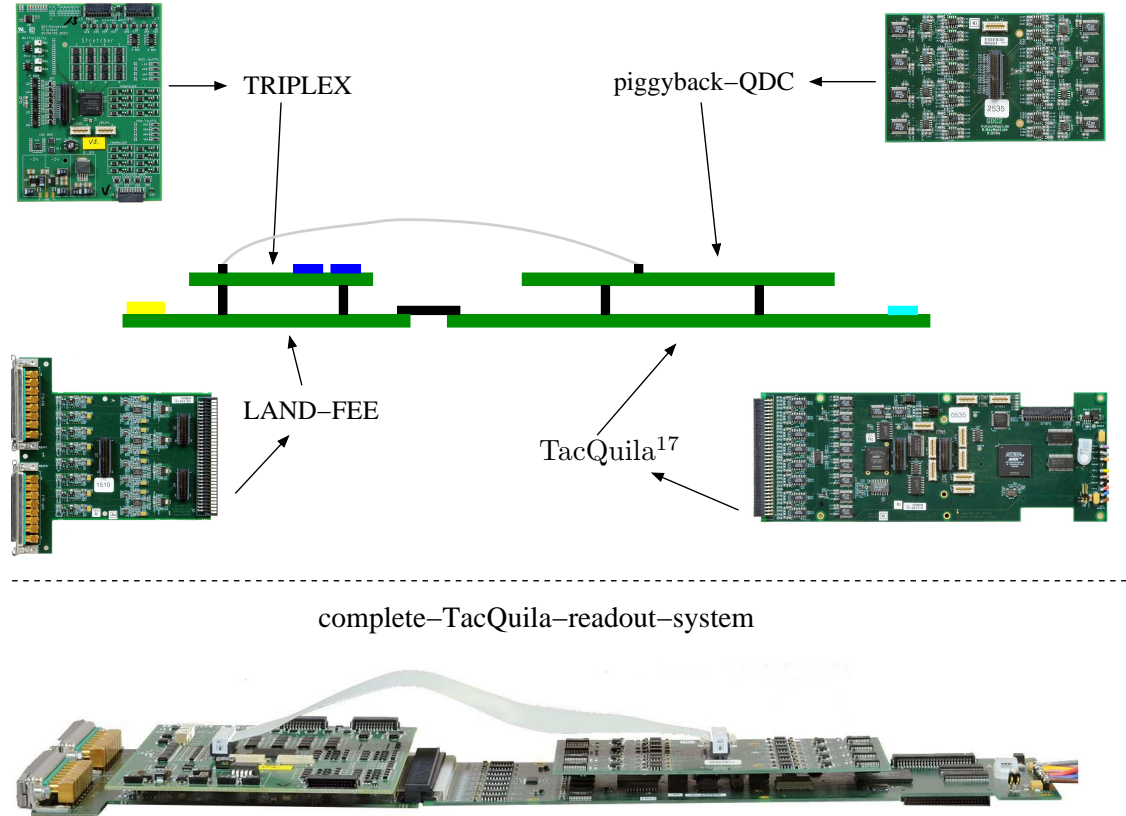

complete–TacQuila–readout–system

Figure 2.9: Upper part: Photographs of the four individual components of one TacQuila-readout-system are shown, namely TRIPLEX, FEE, TacQuila^{17} and QDC. The center indicates schematically how the four components have to be connected. Lower Part: One full assembled TacQuila-readout-system is displayed.

The four TacQuila components are shown in figure 2.9. At the moment these are:

- LANDFEE2,
- TacQuila3,
- QDC2,
- TRIPLEX2.

The numbers, appended to the name of each board, refer to the version of the corresponding electronic board. The modularity of the TacQuila system offers the usage of this readout electronics for various different signal types. Exemplary MRPCs and PMTs can both be readout using the TacQuila system changing only the FEE. A much more detailed description of the TacQuila system can be found in appendix B. Here only the main features will be explained.

Each TacQuila channel delivers a time and a charge measurement for each event. The TacQuila measures the time relative to an external clock. Each channel starts its own time measurement and the next rising edge of the clock serves as a common stop. Furthermore the time measurement is split into a fine and a coarse measure. This means in addition to the measurement relative to the next clock cycle also a measurement how many clock cycles passed between the event and the DAQ* master trigger is done. For that reason the 17th channel is a copy of the DAQ master trigger and allows therefore to measure times longer than one clock cycle, for a schematic of the time measurement see figure 2.10, this figure is also discussed in appendix B.4.
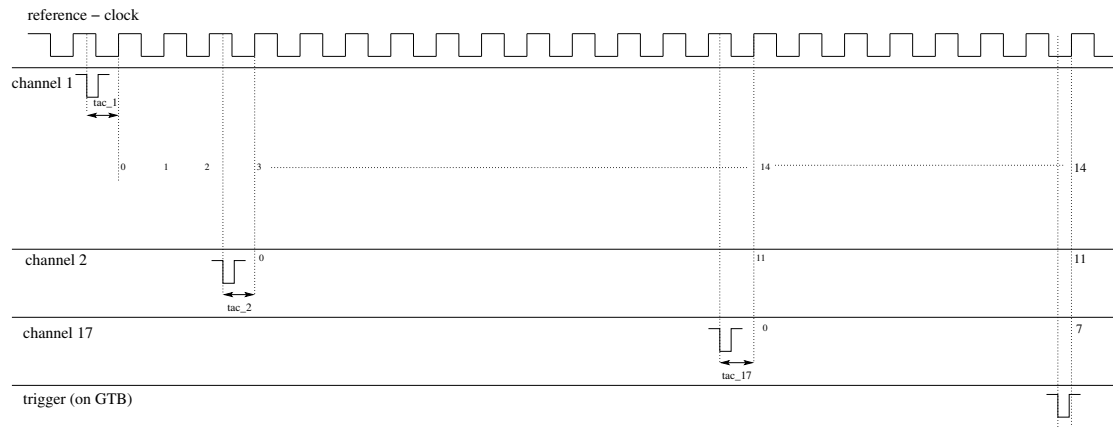

Figure 2.10: Shown is how the TacQuila timing works, for details see text.

The QDC has a virtual-gate, meaning a delay is software-wise applied in a way that the QDC is read out eight clock-cycles (200 ns) after the corresponding comparator fired. For more details on the QDC see appendix B.5.

The individual TacQuila systems are connected via a GTB†-chain and then to a VME‡ module called SAM§, which is readout using an MBS¶ based DAQ. A charge measurement is only available together with a valid time, meaning that if the threshold of the comparator has not been crossed also the charge is not read out. The TacQuila

---

*Data AcQuisition
†GeräTeBus, engl. Device Bus
‡or VMEbus Versa Module Europe
§Steuerungs und Auslese Modul, engl. Control and readout module
¶Multi Branch System; GSI Data AcQuisition software

system is no multi-hit device. If one channel fires this event is kept till either the event is picked up by the trigger or the channel is reset because the reset-time is exceeded. The reset-time can be set by the user to values between 75 ns $\leq$ reset-time $\leq$ 6375 ns; in 100 ns steps. If a second event occurs in the particular channel which triggered already it will be lost.

In nuclear physics experiments in general it is usually required to control equipment via software settings. Moreover, it is crucial to also monitor 'environmental' parameters of the experimental setup, this includes for example low and high voltages or magnetic fields. Since these environmental parameters change at relatively slow rates compared to the real physics data this control software is commonly referred to as 'slow control' [Kie81]. For this purpose EPICS[*] is used in the LAND-R^{3}B-setup. The TRIPLEX board offers the possibility to control the TacQuilas via this general slow control software. This gives, e.g., the possibility to set individual thresholds for each TacQuila channel. The TRIPLEX cards of the individual TacQuila systems are inter-connected in a tree-like structure. A Mul[†]- and OR-signal of all combined TacQuila cards is available via this TRIPLEX tree. The TRIPLEX tree offers also the functionality of a multiplexer, meaning that each individual signal of each FEE can e.g. be directed to a scope.

---

[*]Experimental Physics and Industrial Control System
[†]Multiplicity

Chapter 3

Experimental Method and Setup

In the thesis presented here neutron-unbound states of neutron-rich oxygen isotopes are investigated. The experimental technique, which is used to study neutron-unbound states, is the 'invariant-mass method' [BST12]. In this method the four-momenta of all decay products in the laboratory frame are measured to reconstruct the unbound states. Since the invariant-mass (M_{inv}) is, as suggested by the name, invariant to Lorentz transformations it gives also information on the mass of the unbound state before the decay meaning the mass of the unbound system in its rest frame.

Before the invariant mass can be reconstructed first the unbound state has to be populated. This is due to the inverse kinematics done at beam velocity and the decay products are therefore emitted at approximately beam velocity. These decay products have to be detected in coincidence which requires at least two detection systems: one for the charged particles (heavy fragments) and one for neutrons. In order to detect the neutrons and heavy fragments, which stem from in-flight breakup of the neutron-unbound state, simultaneously, a magnetic dipole field is used to deflect the charged particles from the path of the neutrons.

Future developments, which will allow spectroscopy of neutron-rich nuclei beyond the drip line with very extreme A/Z ratios, have been discussed in chapter 2. In this chapter the present experimental apparatus will be described.

The results presented in this work are obtained from data taken during the s393-experimental campaign. This experiment was conducted successfully by the R^{3}B-collaboration in August 2010, aiming at the investigation of light neutron-rich nuclei with the aid of kinematically complete measurements of reactions at relativistic energies with the LAND-R^{3}B-setup at Cave C. Using six different settings of the FRS, a very wide A/Z range was covered. For the oxygen isotopic chain for example, all existing bound isotopes, from the proton drip line nucleus ^{15}O to the neutron drip line nucleus ^{24}O ($1.9 < A/Z < 3$) have been created [RCa].

In this chapter first the invariant-mass formula will briefly be reviewed. In the

subsequent sections the experimental apparatus and technique will be discussed in detail. Starting from a description of the GSI facility and the FRS, mainly the configuration of the detectors in Cave C, namely the LAND-R^{3}B-setup will be detailed.

3.1 Invariant-Mass

The invariant-mass of a system of 'i' masses with four-momenta $P_i = (E_i/c, \vec{p}_i)$ is given by the following equation:

$$M_{inv}^2 \cdot c^2 = \left(\sum_i P_i \right)^2 ,$$
(3.1)

from which follows:

$$M_{inv} = \sqrt{\sum_i m_i^2 + \sum_{i \neq j} \frac{E_i \cdot E_j}{c^4} - \sum_{i \neq j} \frac{p_i \cdot p_j}{c^2} \cos \sphericalangle[i,j]} ,$$
(3.2)

where $\sphericalangle[i,j]$ is the angle between the momentum vectors of particle 'i' and 'j'. Using

$$E_i = \gamma_i \cdot m_i \cdot c^2 ,$$
(3.3)

and

$$p_i = \gamma_i \cdot m_i \cdot \beta_i \cdot c ,$$
(3.4)

equation (3.2) can be written as follows:

$$M_{inv} = \sqrt{\sum_i m_i^2 + \sum_{i \neq j} \gamma_i \gamma_j m_i m_j (1 - \beta_i \beta_j \cos \sphericalangle[i,j])} ,$$
(3.5)

from which the relative energy E_{rel} can then be obtained by subtracting the masses of the decay products at rest from the invariant-mass M_{inv} of the system:

$$E_{rel} = \left(\sqrt{\sum_i m_i^2 + \sum_{i \neq j} \gamma_i \gamma_j m_i m_j (1 - \beta_i \beta_j \cos \sphericalangle[i,j])} - \sum_i m_i \right) \cdot c^2 .$$
(3.6)

Applying this formula to the ^{25}O case, one obtains for example:

$$E_{rel} = \left(\sqrt{m_{^{24}O}^2 + m_n^2 + 2 \cdot \gamma_{^{24}O} \gamma_n m_{^{24}O} m_n (1 - \beta_{^{24}O} \beta_n \cos \sphericalangle[^{24}O, n])} - m_{^{24}O} - m_n \right) \cdot c^2 .$$
(3.7)

3.2 RIB Production: GSI and FRS

The s393-experimental campaign has been performed at GSI, where the RIB is produced via the so called 'in-flight' technique, meaning the radioactive ions are produced and separated in-flight. This beam production will be briefly explained in the following paragraph. The production mechanism of the RIB starts with a stable, so called, primary beam. At GSI the ions of choice are injected into the UNILAC* from an ion source. In the experiment described here, ^{40}Ar ions have been used as primary beam. From the UNILAC the ^{40}Ar^{11+} beam is injected into the SIS†-18, having an energy of ∼11.5 MeV/u.

For the future upgrade of GSI (FAIR) the SIS-18 will be used as injector. Figure 3.1 shows a schematic layout of the existing GSI accelerator on the left (blue beam line) and the planned upgrade, FAIR, on the right (red beam line). The numbers in the names of the synchrotrons depict the magnetic rigidity in Tm, so from the naming one can immediately see the ratio by how much the FAIR synchrotrons are 'larger' (see e.g. figure 3.1).

Leaving the SIS-18, the ^{40}Ar ions have been accelerated to an energy of 490 MeV/u and the primary beam is guided onto the production target at the entrance of the FRS. A 4011 mg/cm^2 thick Be production target was used. The primary beam had an intensity of 6·10^{10} ions/spill, and it was used for the proton-rich as well as the neutron-rich secondary beam settings. The beam composition delivered to the experimental cave depends on the FRS settings only. The s393-experimental campaign took place in Cave C, highlighted by a green box in figure 3.1. A detailed description of FRS can be found in [GAB$^+$92]. In addition to the FRS setting (magnetic rigidity) also the spill structure of the beam was changed depending on the rate of the secondary beam. The number of ions per spill is fixed as well as the maximum rate of ions for which the experimental setup is able to record all events. As a consequence long spills and a slow ramping mode are used for high-intensity beam settings and short spills and a fast ramping mode are used for low-intensity beam settings. In the framework of this thesis only the most neutron-rich setting ($A/Z = 3$) is of interest. In this setting a fast ramping mode and a short spill have been used due to the low intensities.

The reaction products of the nuclear fragmentation of the incoming ^{40}Ar beam, impinging on the Be target make up the, so called 'cocktail' or 'secondary' beam. A large variety of elements with masses smaller than the one of the primary beam is produced. Out of those the beam composition is then selected by means of the $B\rho - \Delta E - B\rho$ method which is applied in the FRS, see figure 3.2. '$B\rho$-selection' means, that the ions are separated according to their mass-to-charge ratio. This can be shown using

---

*$\underline{\text{UNI}}$versal $\underline{\text{L}}$inear $\underline{\text{AC}}$celerator
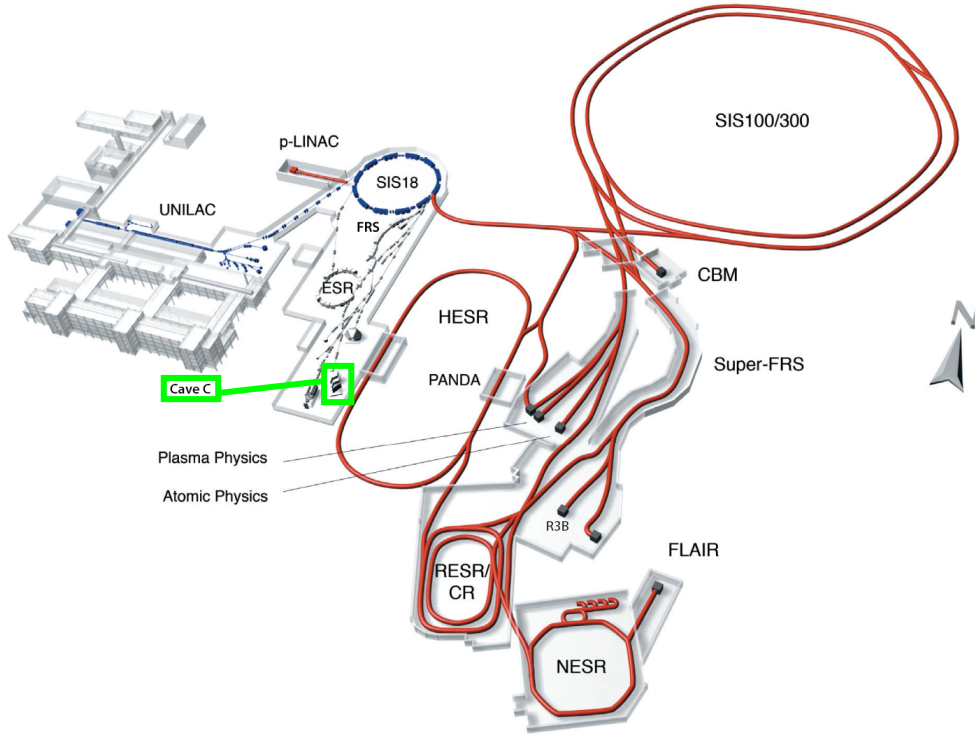†$\underline{\text{S}}$chwer $\underline{\text{I}}$onen $\underline{\text{S}}$ynchrotron

Figure 3.1: Shown is a schematic layout of the GSI accelerator complex as it exists today to the left, its beamline is depicted in blue. On the right also the planned FAIR facility (red beam line) is shown.

the following argument: The Lorentz force equals the centripetal force which keeps the particle of charge number Z and mass number A on a circular orbit with radius ρ, leading to the following condition:

$$B\rho = const \cdot \frac{A}{Z} \cdot \beta\gamma \ . \tag{3.8}$$

Formula (3.8) is only valid for high energy beams for which the ions are fully stripped. In the general representation the charge number Z of the ion has to be replaced by the charge q. The radius ρ is fixed by the given trajectory defined by the beam line. The constant is given by: $const = \dfrac{u \cdot c}{e} = 3.1$ Tm. B is the strength of the magnetic field, β is the velocity of the ion, and γ is the associated Lorentz factor. Formula (3.8) therefore means that for a certain magnetic field (rigidity) only ions with a specific A/Z can follow the trajectory determined by the beam line. The FRS momentum acceptance ($\Delta p/p = 2\%$) [GAB$^+$92] leads to the fact, that the beam contains several different nuclides. The nominal magnetic rigidity ($B\rho$) at the exit of the FRS was set to 9.88 Tm for the experiment described here.

The ΔE - selection is accomplished by inserting a degrader (wedge-shaped material),

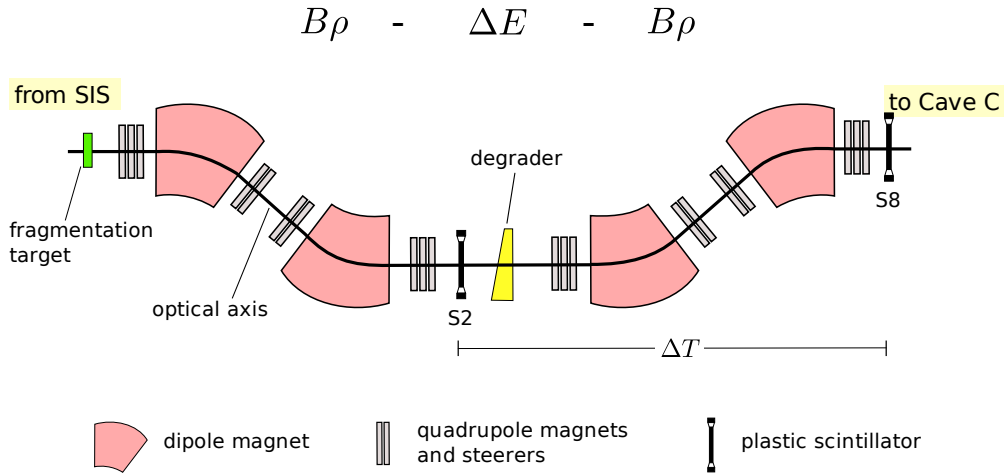$$B\rho \quad - \quad \Delta E \quad - \quad B\rho$$

Figure 3.2: A schematic layout of the FRS is shown. The $B\rho - \Delta E - B\rho$ method is applied using dipoles to 'bend' the beam ($B\rho$) and a degrader to have a position and Z dependent energy loss (ΔE). Two 3 mm thick scintillator paddles were operated in the FRS beam line by the R^{3}B collaboration at S2 and S8 to do a ToF measurement of the incoming ions. Figure is taken from [Lan12].

as shown in figure 3.2. Since, according to the Bethe-Bloch formula, the energy loss is proportional to Z^2 different isotopes will experience a different energy loss. Furthermore, the energy loss depends on the trajectory of the ion, since the depth of the material changes according to the radius of that trajectory. Therefore, unwanted isotopes are then bend out of the beam, due to the different energy loss they experienced before, while passing the second $B\rho$ stage of the FRS. Of course a degrader has on the other hand the drawback that it decreases the intensity. The beam setting used for the analysis presented here had low intensity. For that reason the incoming ions did not have to be restricted to a certain species only and consequently no degrader was used. Therefore many ions with similar A/Z ratio were present in the so called 'cocktail' beam.

The FRS beam line has been equipped with two 3 mm thick scintillator paddles. Those detectors are needed to perform a incoming ToF measurement over a long distance (FRS to Cave C) for each ion. One scintillator paddle was placed at the middle focus (the so called S2 position) and the second was situated behind the FRS (so called S8). As the scintillator at the mid-plane of the FRS (S2), about 136 m upstream of the reaction target, was overloaded with the intense beam, we have been using the scintillator at the intermediate focal plane (S8), leaving us a ∼55 m flight path to Cave C.

3.3 LAND-R^{3}B Setup at Cave C

After production, the secondary beam is transported to the experimental hall (Cave C), where the reaction target is located. The cocktail beam allows simultaneous measurements using a variety of different incoming ions, but it also makes an event-by-event incoming PID* mandatory. A schematic drawing of the detector setup, as used for the analysis presented here, is shown in figure 3.3. For the incoming PID the following two quantities have to be known event-by-event for each ion:

1. velocity (β),
2. charge number Z.

Furthermore, the incoming angle is measured for each event as well. The magnetic rigidity ($B\rho$) has for the experiment described here not been determined event-by-event. This is the case since the FRS yields a precision of $B\rho \pm 1\%$, which is good enough to resolve the light ions investigated here. As a consequence the nominal value is used for all ions, this value is defined through the chosen FRS setting.
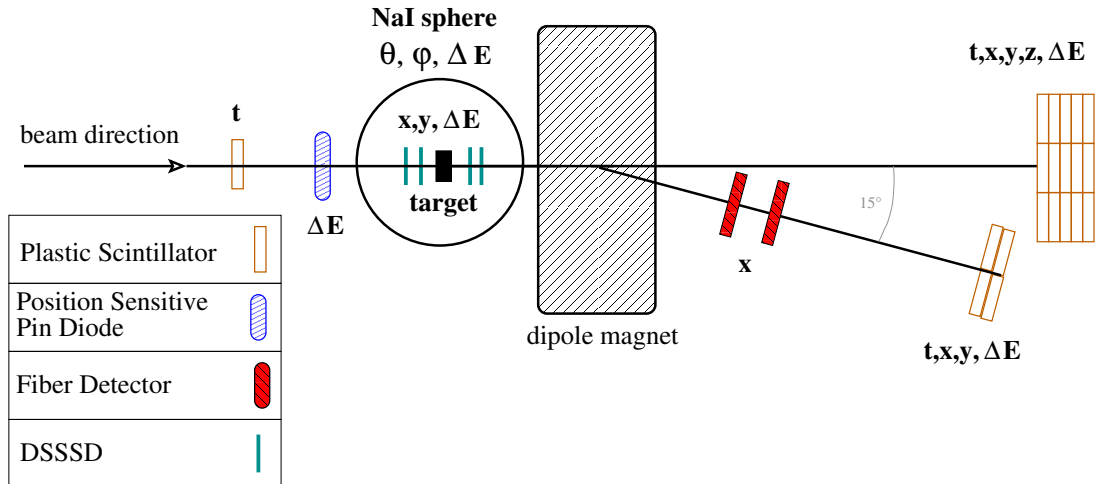
Figure 3.3: The experimental setup in Cave C as used during the s393 campaign is shown. Note that only detectors are shown which are of interest for the analysis presented here. In the figure it is also indicated which quantities are extracted from which detection system.

The final goal of the analysis is to reconstruct the relative energy of the fragment plus neutron(s) system. Therefore, the four-momenta of both, neutron(s) and fragment, have to be measured. To be able to reconstruct those, the following parameters have to be known:

1. Fragment velocity,

---

*Particle IDentification

2. Fragment charge number Z,

3. Fragment mass number A,

4. Fragment trajectory,

5. Neutron velocity

6. Neutron trajectory.

How these quantities are derived using the LAND-R³B-setup will be explained in the following section.

3.3.1 Identification of Incoming Particles

To identify the incoming ions the mass-to-charge ratio (A/Z) and the charge number (Z) are measured. From formula (3.8) one sees that:

$$\frac{A}{Z} = \frac{B\rho}{const} \cdot \frac{1}{\beta\gamma} \ . \tag{3.9}$$

Therefore, determining A/Z means measuring β and $B\rho$. The value of $B\rho$ is known from the FRS setting. The velocity of the incoming ion (β) is measured using a plastic scintillator paddle at S8 as start detector. This detector is read out with two PMTs, one at the top and one at the bottom. As stop detector a square-shaped (2.5 cm × 2.5 cm) plastic scintillator with thickness of 1 mm at the entrance of Cave C is used. This detector is called POS, and is read out with four PMTs, one for each side. The distance between these two detectors is about 55 m, which results in a very good velocity resolution. The S8 detector is shown in figure 3.2, while POS is the first plastic scintillator shown to the left in figure 3.3.

The energy loss of an ion passing through matter depends, following the Bethe-Bloch formula, on Z and β. Using this fact the charge number (Z) is derived from a ΔE measurement using a PSP* in front of the target.

The resulting two-dimensional PID plot is shown in figure 3.4 and depicts that this method allows for a very clean identification of the incoming particles. The ions of interest (^{26}F and ^{27}F) can be chosen for further analysis using two-dimensional cuts.

The beam spot on the target can be fine tuned using active slits (ROLU†). This detector system consists of four movable plastic scintillators which are each read out with one PMT. Every ion detected in this detector will be disregarded. The incoming angle is measured using two DSSSD‡s in front of the target. The coordinate system, used in the analysis presented here, is labeled in the following convention: The z-axis points in beam direction, the x-axis points to the left looking with the beam and the y-axis

---

*$\underline{P}$osition $\underline{S}$ensitive $\underline{P}$in-diode

†$\underline{R}$echts $\underline{O}$ben $\underline{L}$inks $\underline{U}$nten, german for: right, up, left, down

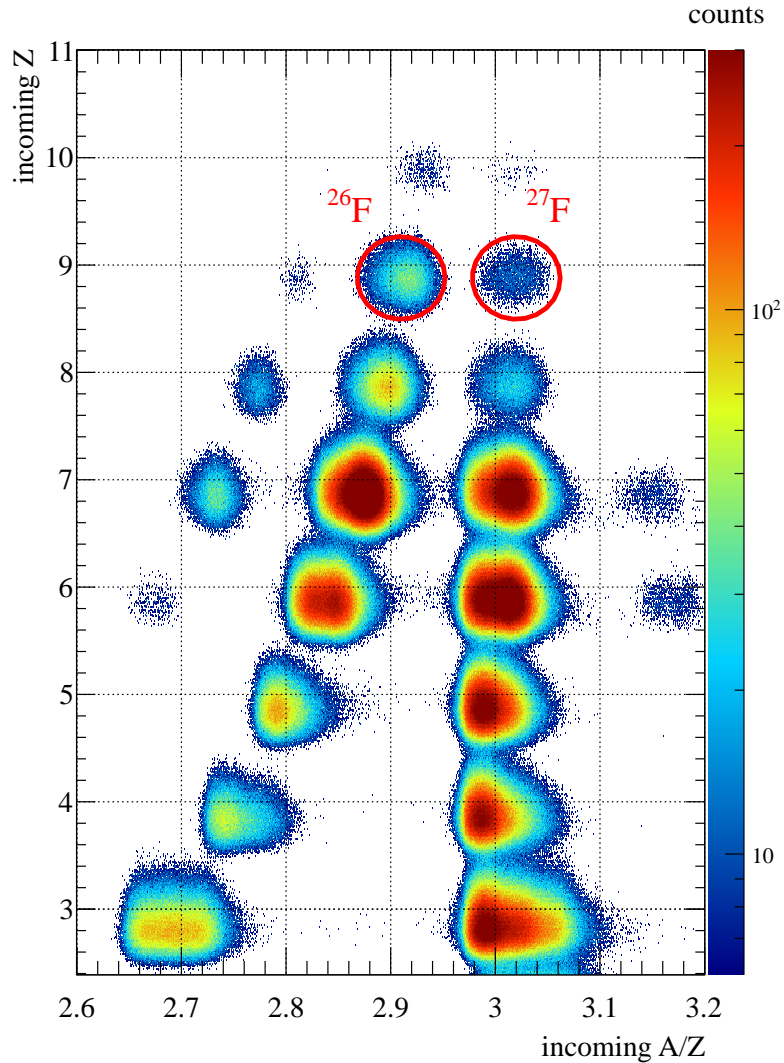‡$\underline{D}$ouble $\underline{S}$ided $\underline{S}$ilicon $\underline{S}$trip $\underline{D}$etector

Figure 3.4: Incoming PID for the most neutron-rich setting (A/Z=3) of the s393 experiment. The cuts on ^{26}F and ^{27}F are indicated as red ellipses.

points to the top. One side of each in-beam DSSSD delivers a position measurement in x-direction and the second side gives the y-position. To deduce the angle (θ) of the incoming ion, also the distance in z-coordinate between the two detectors has to be known to a very good precision. The exact positions of all detectors shown in figure 3.3 have been determined using photogrammetric techniques. The results of this procedure are shown in table 3.1 [HV11]. Having x, y and z position, θ of the incoming ion can be deduced. The next material, which the ions pass, is the actual reaction target. The targets are mounted on a remote-controlled target-wheel offering the possibility to change

the targets in vacuum without beam breaks. The used targets for the here presented beam setting are given in table 3.2.

detector name	distance to center of ALADIN in cm	error due to photogrammetric technique in cm
DSSSD-1	-266.0	∼0.05
DSSSD-2	-263.3	∼0.05
target	-259.6	∼0.05
DSSSD-3	-248.5	∼0.05
DSSSD-4	-246.0	∼0.05
GFI-1	196.6	∼1
GFI-2	351.1	∼1
TFW	874.0	∼2
LAND	1268.0	∼5

Table 3.1: Distance in z-direction of each detector along the nominal beam trajectory relative to the center of ALADIN.

target	area density in mg/cm^2
CH_2	922
C	935
Pb	2145

Table 3.2: Reaction targets as used in experiment-s393.

Since the reaction mechanism is not of major impact here, data taken with all three targets has been combined for this analysis.

3.3.2 Detection of the Reaction Products

Before coming to the question 'how the reaction products are detected' a few general things concerning the reaction shall be discussed. The high beam energy is advantageous for several reasons. The kinematical-forward focussing of the reaction products makes full-acceptance measurements possible having detectors which cover in the lab-system a considerably smaller solid angle than 4π. Furthermore, the high beam energy allows the usage of relatively thick targets, which makes the investigation of exotic nuclei possible even if such isotopes can only be produced with very low rates [Aum05b, Aum05a].

The outgoing fragments are detected in two DSSSDs directly behind the target, their charge is determined via a ΔE measurement and the outgoing angle (θ) is measured as well. The target is surrounded by four additional DSSSDs, the so called box-detectors, and a 4π NaI sphere named CB*. The CB is segmented into 162 crystals which are

---

*C̲rystal B̲all

all equipped with a high-gain readout for γ-rays and in the forward hemisphere also an additional low-gain readout for protons. This detector is, in the analysis presented here, used to tag the proton knockout via the CB-sum trigger.

The beam line was evacuated up to the target chamber. After DSSSD-4 the reaction products leave the vacuum and enter ALADIN which is filled with helium gas. The magnetic field of ALADIN bends the charged fragments but leaves the neutrons unaffected on their straight trajectories. All detectors behind ALADIN are operated in air.

In the following, we will first focus on the detection of the fragments, which is done using the so called fragment 'branch' or 'arm' of the experimental setup. The fragment branch is oriented such that the central position at each detector is at 15° with respect to the incoming beam axis. It consists of 3 detectors, see figure 3.3, two fiber detectors, GFI*-1 and 2 and the TFW†.

Each GFI is build of 480 vertical fibres covering in total an area of 50×50 cm². A position measurement in x-direction (horizontal) with a resolution of 1 mm [MJP+09] is done using this type of detectors. Having these two position measurements behind the magnet and the ones done by the DSSSDs in front of the magnetic field, the trajectory of the ions can be reconstructed. Different isotopes are deflected to different angles in the magnetic field of ALADIN according to their different mass-to-charge ratio, see formula (3.8). Therefore, the $B\rho$ of an ion is measured by reconstruction of the track of this ion through the magnetic field. The $B\rho$ value determines the mass of the ion unambiguously if the charge is already known, see section 4.1. Detailed information on the GFIs can be found in [CSG+98] and the calibration procedure is described in [MJP+09]. The last detector in the fragment branch is the TFW. This detector is build out of 14 horizontal scintillator paddles in the first plane and a second plane having 18 vertical paddles. Each horizontal paddle has the dimension (196.6×10.4×0.5) cm³, while the vertical paddles have a dimension of (154.6×10.4×0.5) cm³. All 32 paddles are read out using a PMT on each side. The time, ΔE as well as position of each hit is measured. Having the ToF between target and TFW and knowing the length of the trajectory gives the velocity of the ion, while the deposited energy determines the charge.

The neutrons are detected in LAND [BEE+92]. The characteristics of this detector are also given in table 2.1. The detector covers an area of (2×2) m² and is 1 m deep. It consists of 10 planes and every plane contains 20 paddles, which have the dimensions of (200×10×10) cm³. The detection of the neutrons is based on the use of inactive converter materials in which the neutrons create charged particles via nuclear reactions. Those secondary particels are then detected with plastic scintillators. To not stop too many of the created secondary charged particels in the converter material itself, the design of the detector is based on a sandwitch structure using thin iron layers as converter material.

---

*Großer FIber detector, german for: 'large fibre detecor'
†Time of Flight Wall

One paddle has eleven iron and ten scintillator sheets of 5 mm thickness each. Only the two outermost iron layers have a thickness of 2.5 mm adding up again to 5 mm while stacking two paddles. LAND measures the ToF of neutrons as well as the position of interaction. Using this information the momentum of the neutron is reconstructed. As an additional quantity also the deposited energy of neutrons is reconstructed, see chapter 4.2.

3.4 Data Acquisition

Using the detectors described in the last section the interaction of nuclei/nucleons with matter is used to create (electrical) signals. In the most common detector type, a plastic scintillator coupled to a PMT, the visible light created by the scintillation is converted to an electrical pulse. Those electrical charge pulses are stored as digital data by the DAQ. In most applications, the quantities which one wants to derive are the energy deposited by the 'particle' in the detector and the time of arrival. The DAQ accomplishes this task via signal processing, conversion from analog signals into digital numeric values and in the final step writing the data files. Those files can later on be analyzed. The DAQ is build from hardware as well as software. The LAND-DAQ software is based on MBS [EK03]. The hardware is composed of various different digitizers (ADC*s, QDCs and TDCs), having specific characteristics for the different detectors.

The route of a signal will be discussed briefly in the next paragraph to explain the individual steps, one example for such a signal flow can also be seen in figure B.3. Traditionally, the electronic readout systems consists of two chains: The timing chain made out of a discriminator, a TDC and/or a scaler for the timing/counting acquisition and an energy chain which holds a delay line and a QDC.

The discriminator generates, if its threshold is exceeded, an logical output from the analog input pulse. A TDC can be pictured as the combination of a TAC† and an ADC (TDC=TAC+ADC). A TAC needs as inputs a start and a stop pulse. The start pulse initiates the linear ramping of a voltage, while the stop pulse stops this process. As a consequence the generated amplitude is proportional to the time interval between the start and the stop pulses. This generated voltage can be given to an ADC, which converts it to a digital number. In combination the TAC and the ADC create a digital value which is proportional to the time interval between two pulses, meaning they act as a TDC.

In the energy branch cable-delay is commonly used to delay the signal. The QDC can be pictured as being built from a capacitor plus an ADC. An ADC converts the input voltage to a digital value, meaning it is sensitive to the amplitude of an input

---

*Analog to Digital Converter
†Time to Amplitude Converter

pulse. Adding a capacitor an integrator is build, meaning a QDC measures the charge (the area below a pulse). This quantity represents the energy information of the incident particle. The working principle of a QDC requires a gate signal to define the integrating window. This is why a delay line on the signal path to the QDC input is necessary. The input pulses have to be matched with the gate, which arrives with some latency in respect to the analog pulses that produced it. The QDC gate and the TDC start or stop signal are issued by the so called trigger. The term 'trigger' refers here to a signal issued by the DAQ which delivers the gates, starts and stops to the corresponding digitizers, but also causes all digitizers to deliver the data to the data stream.

During the analysis of the data it is very important to know how the data has been recorded, in particular the trigger conditions have to be known. Having a signal in only one detector channel refers most likely to noise. To avoid collecting noise in the data stream a trigger is constructed requiring coincidences between several signals. One step is, for example, to combine signals from one detector building a detector-trigger. But also more complex triggers can be build combining the information from several detectors. The least restrictive coincidence, which is required in the LAND-DAQ is the so called 'minimum-bias' (see table 3.3), which ensures that the ion impinges on the reaction target. To trigger on reactions additional conditions to the minimum bias are required, e.g., a LAND-trigger.

The reaction rate of incoming ions in the reaction target is in the order of $\sim 1\%$ and data acquisition rates are limited. This leads to the fact that the unbiased triggers are downscaled. These downscale factors have to be known very precisely to be, e.g., able to calculate a cross section later on. The most important triggers as well as their downscale factors for the most neutron-rich beam setting are given in table 3.3. The information on the trigger type is written to the data in a bit-pattern.

The experiment described here was the first LAND-R^{3}B experiment which used a VULOM*4-based trigger logics (called 'TRLO II'). This means the trigger matrix/coincidences were set via FPGA-software.

Besides the physics triggers, which all include a 'spill-ON' condition, two calibration triggers are used. Namely, one trigger which is used for time calibration (tcal) of all TDCs and a second trigger which issues a zero charge measurement for all QDCs, called 'clock' trigger. For more details on the LAND-Cave C DAQ the reader is referred to [Joh10] and [Joh06].

---

*VME Universal LOgic Module

| trigger bit | 'objective' | input to TRLO | | | | | downscale |
		17 on-spill	11 CB-sum	5 TFW	3 LAND	1 POS.!ROLU	
1	minimum bias	x				x	2^6
2	fragment	x		x		x	2^4
5	CB-sum	x	x	x		x	2^0
8	LAND	x		x	x	x	2^0

Table 3.3: A part of the trigger matrix is shown to present the most important triggers. The full matrix contains 20 input signals and 16 different generated triggers as output. Requirements for coincidences (x) between input signals lead to different triggers. The left column shows the trigger bit which is set if this trigger is issued. The second column holds the 'name' of the trigger. The middle part, separated with the double vertical lines shows how the inputs are connected to build a certain trigger, a blank field means that this input is not considered. The last column holds the used downscale factors for the different triggers.

Chapter 4

Identifying the Reaction Channel

Signals delivered from the detectors are, as described in the previous chapter, stored as event-wise data words into so called lmd* files (MBS data format developed at GSI). While this file format is very handy to write the data to during the experiment it is not suitable for the analysis later on. The process going from a lmd file to e.g. a `ROOT` [Cer] file is called 'unpacking'. This process is done using the `land02` software package written by H. Johansson. Without calibrations the data delivered by this step is present in RAW level, see figure 4.1, this means a quantity has commonly a value between 0 and 4095 since the data is stored as 12 bit words, this data format is referred to as having a value in 'channels'. To enable a subsequent physics analysis those values have to be converted into physical quantities like for example times in ns. Furthermore, the individual channels of one detector have to be synchronized to each other, the detectors have to be synchronized amongst each other and if present the time dependence of these synchronization and conversion parameters has to be corrected for. Synchronizing channels refers to the procedure in which times are shifted using an offset in a way that all channels have a common zero, and energies are scaled, using gain factors, such that they have the same range for all channels. For all these higher data levels calibration steps are needed and for that purpose the `land02` software package offers routines, as shown in figure 4.1. To determine the time dependence of calibration parameters a set of `Perl` scripts was added to this software package by D. Rossi.

The different data levels, steps required, and programs involved in going from one to the next level are shown in figure 4.1. The calibration/synchronization procedures applied for the detectors of the LAND-R^{3}B-setup have been described before, see e.g. [Ros09], [Joh10] and [LB09], they will not be detailed here. The calibration parameters used for detectors in front of the target (incoming PID) were obtained by M. Heine. The calibration of the DSSSDs was done using a set of scripts written by V. Panin [Pan12] and modified by M. Holl. To select a certain reaction channel several conditions on,

---

*list <u>m</u>ode <u>d</u>ata
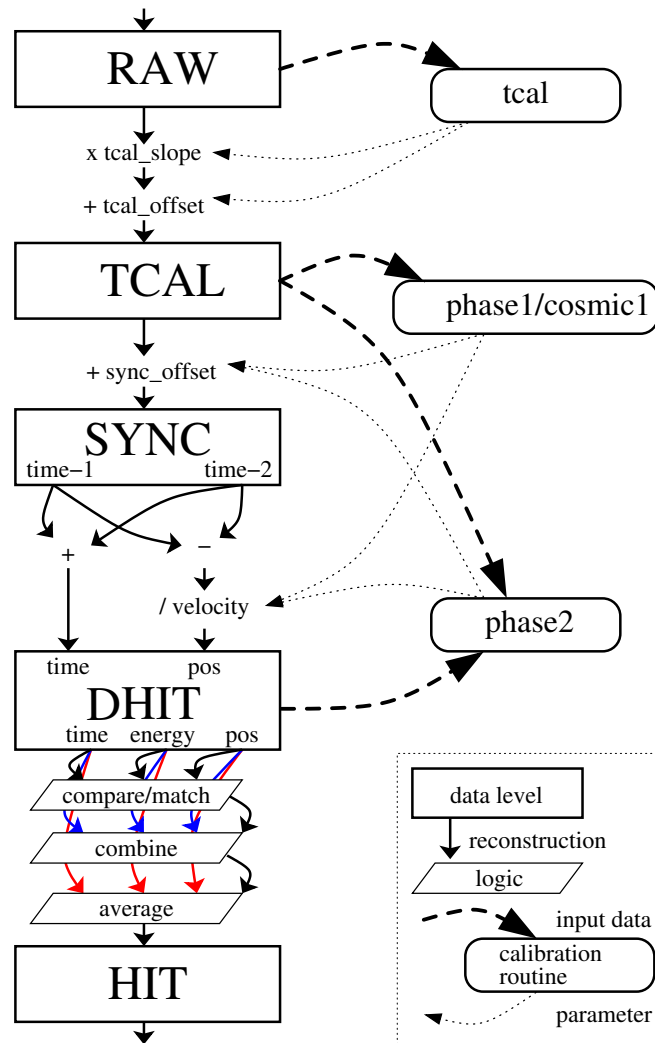
Figure 4.1: Shown are the different data levels as well as the routines and parameters which are involved in transforming the data from one to the next level. The different levels contain data in the following status:

- RAW: Values are given in channels and are stored as integer.
- TCAL: Times are converted to ns, and for energies the pedestal is subtracted. Data is from now on stored as floating point.
- SYNC: A time offset synchronizes all channels, energies are synchronized using a gain factor.
- DHIT: Reconstructed hits are given in a detector specific coordinate system (e.g. indices of a matrix defined by a position sensitive PMT).
- HIT: The position of a hit is given in a detector internal coordinate system with its origin (normally) at the center of the detector. Position, time and energy are given in physical units.

e.g., charge and mass have to be applied to the data. The two following reactions are of particular interest here:

1. ^{26}F + T $\rightarrow$ ^{25}O $\rightarrow$ ^{24}O + n,

2. ^{27}F + T $\rightarrow$ ^{26}O $\rightarrow$ ^{24}O + 2n.

Where T can be any of the target nuclei given in table 3.2. First the appropriate incoming isotope has to be selected, this is done via a 2d elliptical cut on A/Z vs. Z as shown in figure 3.4.

Knowing the charge and the mass of the incoming ion, the next step is to identify the fragment. This procedure is split in two parts. First, the charge number (Z) is identified and second, the mass has to de determined. The charge number can be identified via ΔE measurements. As shown in figure 4.2 two ΔE measurements are applied, one directly behind the target and a second one at the end of the fragment branch.
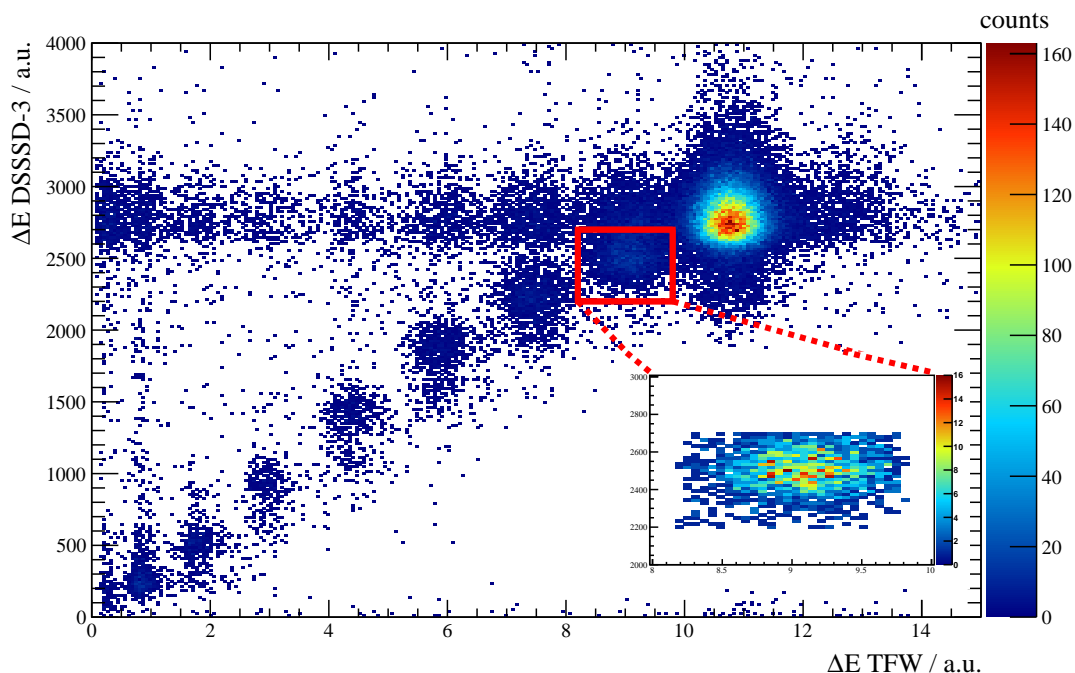
Figure 4.2: Energy loss in the first DSSSD behind the target (DSSSD-3) vs. energy loss at the end of the fragment branch in the TFW. The incoming cut on ^{26}F has been applied already. The most intense peak is the unreacted ^{26}F. On the diagonal one can see that isotopes of all lower charges are produced in the target. The horizontal band contains products of breakup reactions behind the target, e.g. in air. The small inlay in the right, lower corner depicts the cut which is applied to select oxygen ($Z = 8$) isotopes.

Knowing the charge, the mass is fixed as soon as one knows the mass-to-charge ratio, which on the other hand can be determined via the trajectory of the fragments through

the magnetic field of ALADIN. The procedure of determining the mass of the reaction products will be described in the following chapter.

4.1 Fragment-Mass Identification via Tracking

Two standard ways for fragment-mass (A_F) identification via tracking are commonly applied while analyzing data taken with the LAND-R^{3}B-setup.

1. generic tracker,
2. reference tracking.

The first method (e.g. described in [Wam11]) uses a tracking technique based on the knowledge of the magnetic field and absolute detector positions and can be employed using a standalone program developed by R. Plag. The second approach (e.g. described in [Ros09]) uses the trajectory of a known beam (A/Z) as reference and translates deviations from this trajectory into $\Delta(B\rho)$ and therefore mass values using a first order transport matrix.

For the light nuclei used in the presented experiment, a third method, called here 'empirical mass' becomes applicable [ZHN$^+$97]. It will be described in detail in this section. The reference tracking is mostly used if outgoing and incoming (reference) ions have the same charge number, and hence is not suited for the physics channels analyzed here. The empirical mass formula has two advantages compared to the generic tracker, the usage of an external program is not needed, and it easier to use, since the procedure of calibrating the tracker is not needed.

By looking at the position of one ion on one GFI vs. the angle of its track relative to the beam axis measured with both GFIs like shown in figure 4.3, the different masses can be separated already without applying full 'tracking'. To prepare the shown figure an incoming cut on ^{15}B was applied as well as a cut on the outgoing charge ($Z = 5$) and therefore allowing only boron fragments.

To be able to understand this structure in more detail, the generic tracker was used as simulation tool to reproduce the hit positions and investigate the dependence on certain parameters. The tracker can be run using the 'sim' option, giving A, Z, β, x_0, y_0, dx and dy. Where x_0 and y_0 denote the postion on target, while dx and dy are the angle at which the ion enters the magnetic field.

The locations of the detectors in Cave C are given as determined by the photogrammetry, see table 3.1. The magnetic field of ALADIN has been measured before for different currents, these field maps are used here to simulate the magnetic field. For the given parameters of the setup (detector positions and magnetic field) the track of the defined ion (A,Z, β and incoming angle) is fully determined and the tracker gives hit positions in detector coordinates as in the experimental data.
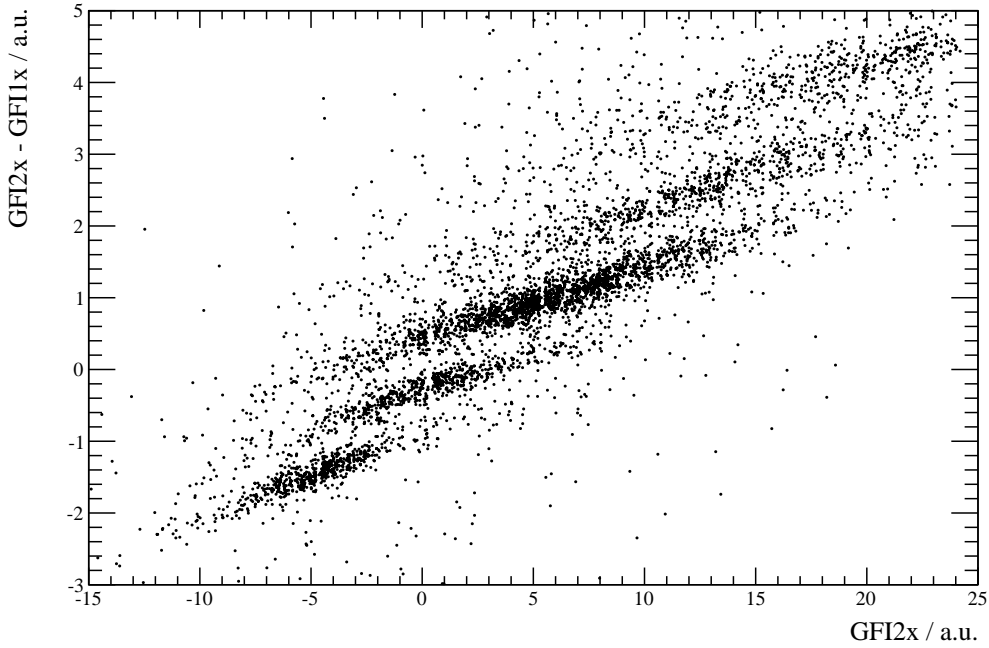
Figure 4.3: Shown is the x-position on the second GFI vs. Δx between the two GFIs (which is essentially the angle: $\alpha \sim \tan \alpha = \dfrac{\Delta x}{\Delta z} \propto \Delta x$). The here shown data represents incoming ^{15}B and outgoing boron isotopes. This test case was chosen since the structure can clearly be seen due to higher statistics.

To investigate conditions closer to the reaction channels of interest a second test case was investigated using incoming ^{20}O ions. For the simulation the charge number was fixed ($Z = 8$) while the mass number was changed from $A = 16$ to $A = 20$, resulting in the five bands visible in figure 4.4. The other parameters have been varied according to values which are comparable to deviations found in the data for unreacted beam. The position on target was changed by ± 0.35 cm ($=$ one σ), which translates one-to-one in a horizontal shift on the GFIs. The velocity (β) of the incoming ions deviates only very little from the mean value. In the ^{20}O case a gaussian with $\beta_{mean} = 0.7226$ and $\sigma = 0.0005$ was found. The value of β was changed in a range $\beta_{mean} \pm 2\sigma$ which results in a small increase in the width of each band. The most influential parameter is the angle in the x-z plane under which an ion enters the magnetic field. The angle was changed in a range $\pm 1\sigma$ for the spectrum shown in figure 4.4, being responsible for most of the visible spread. A quite good agreement between simulation and data is found, in particular the width for unreacted beam can be explained, for this the deviations have been determined from the data. For the reaction fragments the position and slope can be reproduced. The width of each band is as expected much wider in the experiment
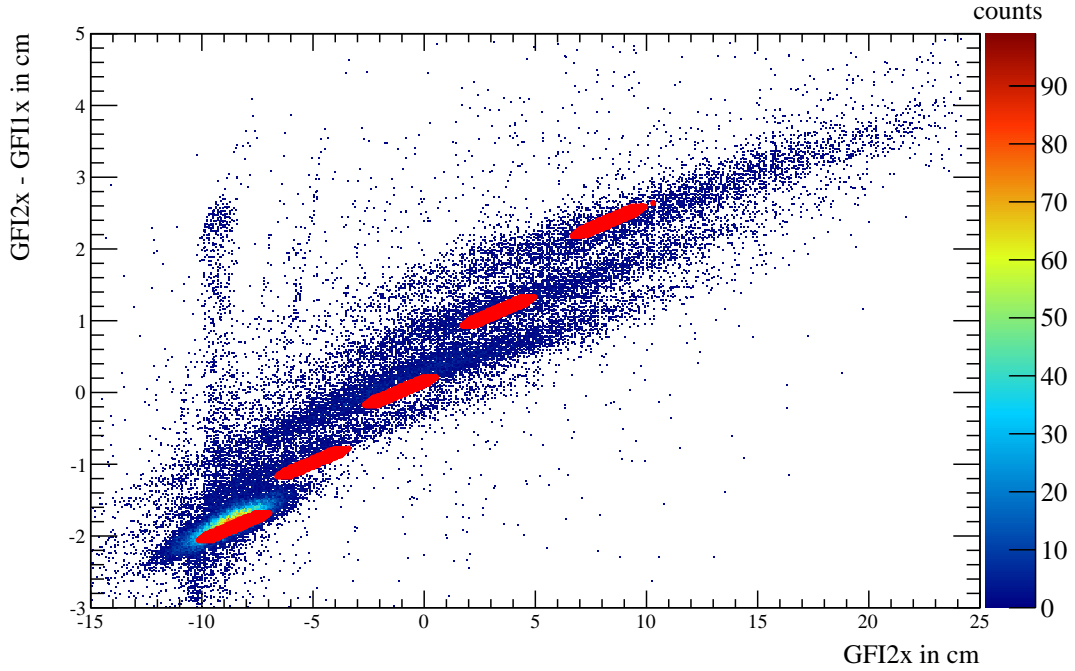
Figure 4.4: Shown is the x-position on the second GFI vs. Δx between the two GFIs. The data shown in color represents incoming ^{20}O and outgoing O isotopes. On top, the results of a simulation are shown in red. For more details see text.

than in the simulation as a result of the reaction and straggling.

On the basis of the correlation shown in figure 4.4 the fragment mass can be reconstructed using an empirical formula. Besides the dependence on the angle (α), two further 'corrections' have been included covering the correlation to β as well as the target position (x_0), resulting in the following formula for the fragment-mass (A_F):

$$A_F'' = \alpha - a_1 \cdot GFI_x , \tag{4.1}$$

$$A_F' = A_F'' - a_2 \cdot \beta_F , \tag{4.2}$$

$$A_F = A_F' - a_3 \cdot x_0 . \tag{4.3}$$

The coefficients a_i have been determined empirically using the experimental data. The result obtained using the empirical formula for the fragment mass (A_F), see formula (4.3) is exemplary shown in figure 4.5. In this spectrum, the peaks were shifted and scaled to match the mass number. However, this is not done for the analysis of the ^{25}O and ^{26}O channel.

To check that the empirical mass formula is correct, it is compared to the results obtained from the generic tracker. A good agreement is found for the test case shown
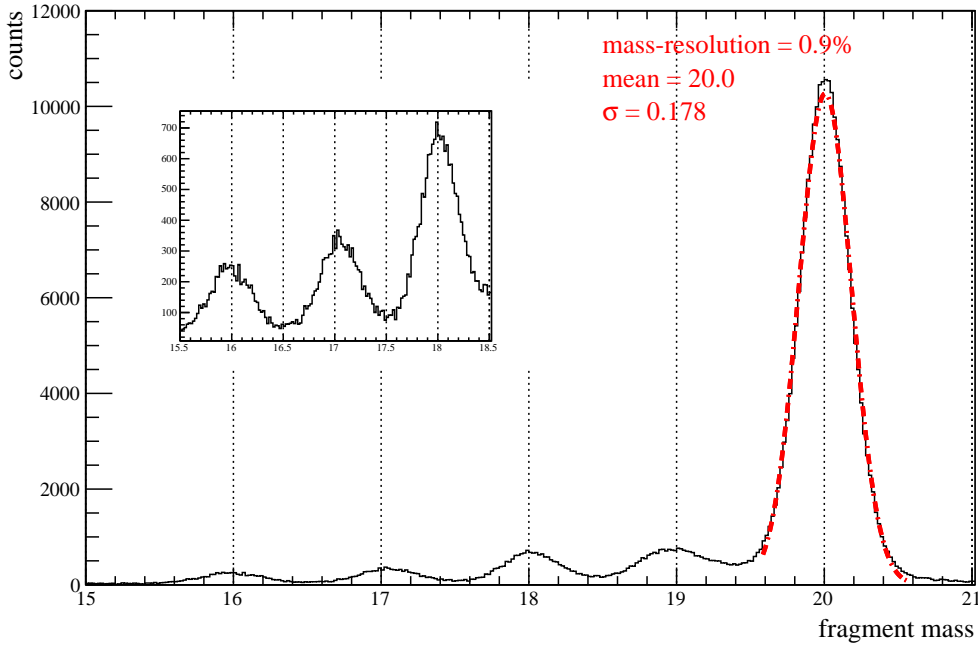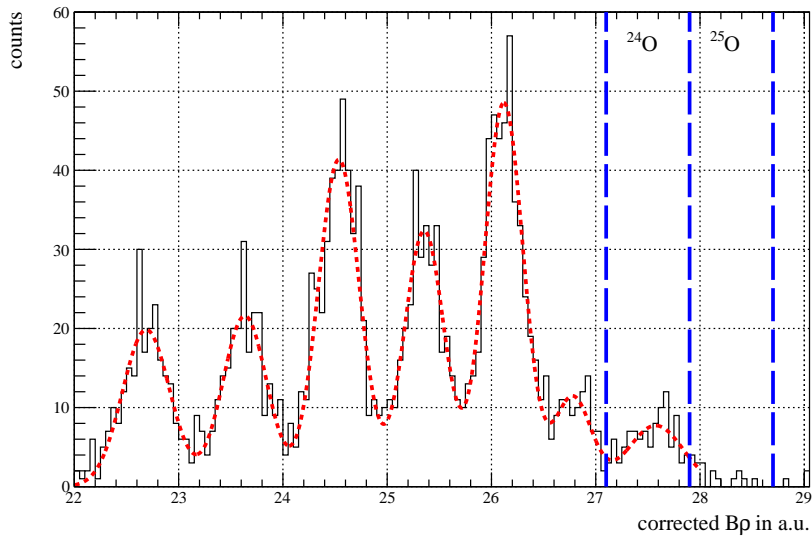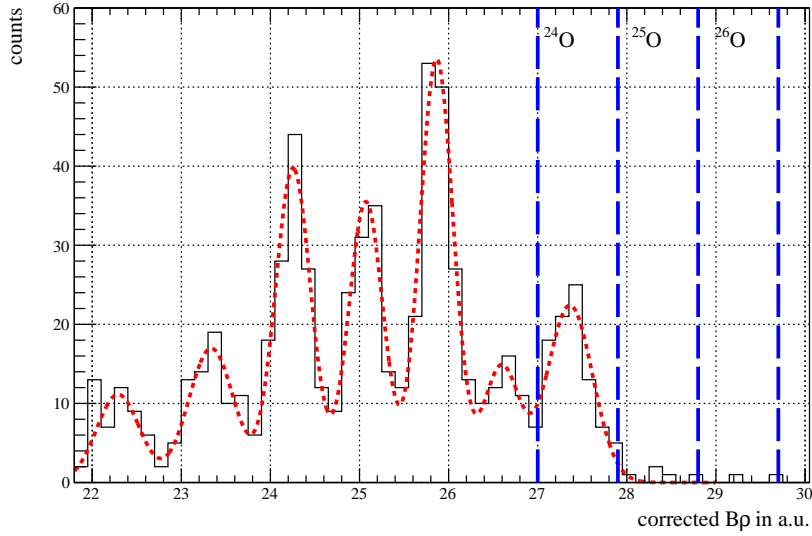
Figure 4.5: Fragment mass distribution for incoming ^{20}O and outgoing oxygen isotopes, derived from tracking of the fragment through the magnetic field. A gaussian fit to the unreacted ^{20}O peak shows that a mass resolution of 0.9% is achieved. In the inlay a zoom on lower masses is shown to present that also in this mass region the separation is very good.

in figure 4.6.

The mass distributions for incoming ^{26}F and ^{27}F and outgoing ions with charge number $Z = 8$ (oxygen isotopes) are shown in figure 4.7 and figure 4.8. Applying the mass cut shown in these two spectra completes the selection of the reaction channel as far as fragments are concerned.

One remark has to be made: All three tracking methods suffer from wrongly reconstructed positions on the GFIs. Meant are the events which e.g. in figure 4.4 are visible as the vertical band at GFI2x $\approx$ -10. But combining two methods like shown in figure 4.6 these events are not correlated, and can therefore be excluded from the analysis.

The consequence of the potential ^{25}O and ^{26}O in the fragment mass spectra, shown in figure 4.7 and figure 4.8, is discussed in chapter 7.

Besides the mass and the angle, also the velocity of the fragment has to be known; this quantity can be determined from the measured ToF. Since the fragment passes through material (air and detectors) on its way from the target to the TFW, the velocity is not constant; therefore the measured ToF can not directly be converted into the velocity at

45
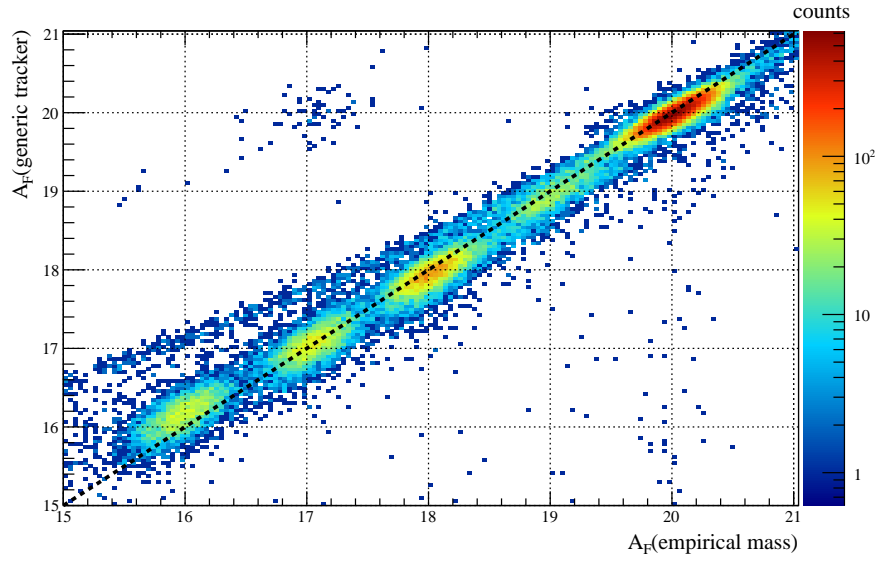
Figure 4.6: Two dimensional fragment mass distribution for incoming ^{20}O and outgoing oxygen isotopes. The fragment mass is once determined using the generic tracker and once using the empirical mass formula.

Figure 4.7: Fragment mass distribution for incoming ^{26}F and outgoing oxygen isotopes ($Z = 8$), derived from tracking of the fragment through the magnetic field. The gate on ^{24}O is indicated by the blue dashed lines, it is also indicated in which region heavier oxygen isotopes would be expected. The spectrum was generated requiring a CB-sum trigger only, to not decrease statistics even further.

Figure 4.8: Fragment mass distribution for incoming ^{27}F and outgoing oxygen isotopes ($Z = 8$), derived from tracking of the fragment through the magnetic field. The effect of the so called 'odd-even-staggering', meaning even nuclei are more stable due to pairing, is visible. The cut on ^{24}O is indicated by the blue dashed lines. The spectrum was generated requiring a CB-sum trigger only, to not decrease statistics even further. Applying the condition that no neutron is detected in LAND one event remains in the ^{25}O oxygen and zero in the ^{26}O oxygen gate.

the middle of the target. Using ATIMA* [Wei] the energy loss, which is itself velocity (energy) dependent, is taken into account and a look-up table is generated which converts a measured ToF into a velocity at the center of the target. The energy and β, respectively, at the center of the target for the two incoming species of interest were:

- ^{26}F: E=442 MeV/u $\rightarrow \beta$(E)=0.735,
- ^{27}F: E=414 MeV/u $\rightarrow \beta$(E)=0.722.

---

*<u>AT</u>omic <u>I</u>nteraction with <u>MA</u>tter

4.2 Neutron Tracking

The unbound ^{25}O and ^{26}O nuclei decay in-flight and the neutrons fly undisturbed by the magnetic field straight into LAND. The detection mechanism of LAND consists of a two-step process:

1. Neutrons are converted into charged particles and γ-rays in the iron sheets.
2. Those secondary particles are then detected in the scintillator sheets.

A neutron induces therefore a shower of secondary, particles in the detector. The first analysis step dealing with LAND data is hence to reconstruct those showers and to distinguish primary from secondary hits. Meaning e.g to make sure, if two hits are recorded inside LAND whether they belong to one neutron or two. The term 'hit' refers here to the fact that both PMTs of one paddle did fire in coincidence.
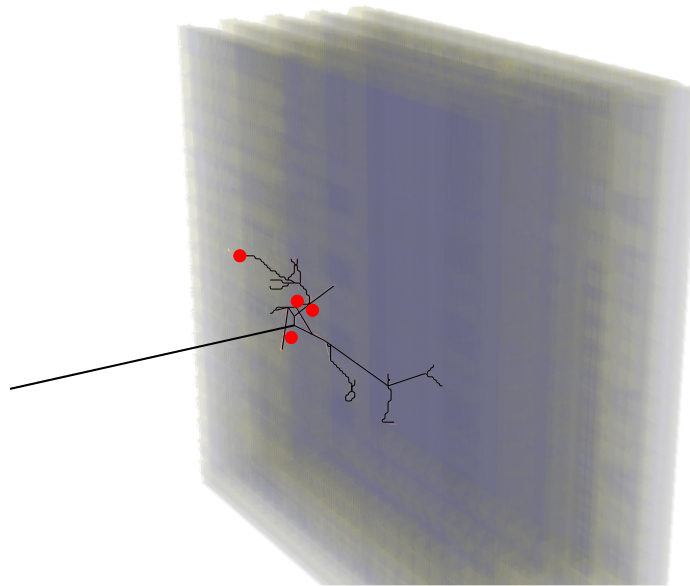
Figure 4.9: Shown is a particle shower in LAND induced by one neutron (1n-event). The picture was generated by D. Kresan using a R^{3}B-`ROOT` simulation. The tracks are shown as black solid lines. The red dots represent a hit, meaning that both PMTs of one paddle fired in coincidence.

The described task of sorting hits into showers and therefore neutrons is done by a routine called 'shower algorithm' in the LAND analysis framework. A shower in LAND induced by one neutron (1n-event) is exemplary shown in figure 4.9, in which

four hits belonging to a 1n event are depicted. The first such algorithm used by the LAND collaboration was developed in the early 90s by J. Keller and is called 'tracking algorithm' [KM91]. The first 'shower algorithm' was written by Th. Blaich. Attempts to improve it by using for example the deposited energy [Lei97] did not lead to further improvement. The main difference between the tracking and the shower algorithm is that the tracking algorithm has the better performance concerning charged particle identification [Lei11, Sim11, Ros11]. A recent 'review' covering this topic can be found in [PBL+12]. The shower algorithm uses HIT-level data (see figure 4.1) as input. Various conditions and sorting methods are applied on the data to identify neutrons, photons, cosmic muons, and charged particles. The output of the shower algorithm contains θ, ϕ and β of the neutron, instead of the original information present at HIT level (time, position and energy); this format is more useful for the subsequent physics analysis. The different conditions which are applied to identify neutrons will be discussed here.
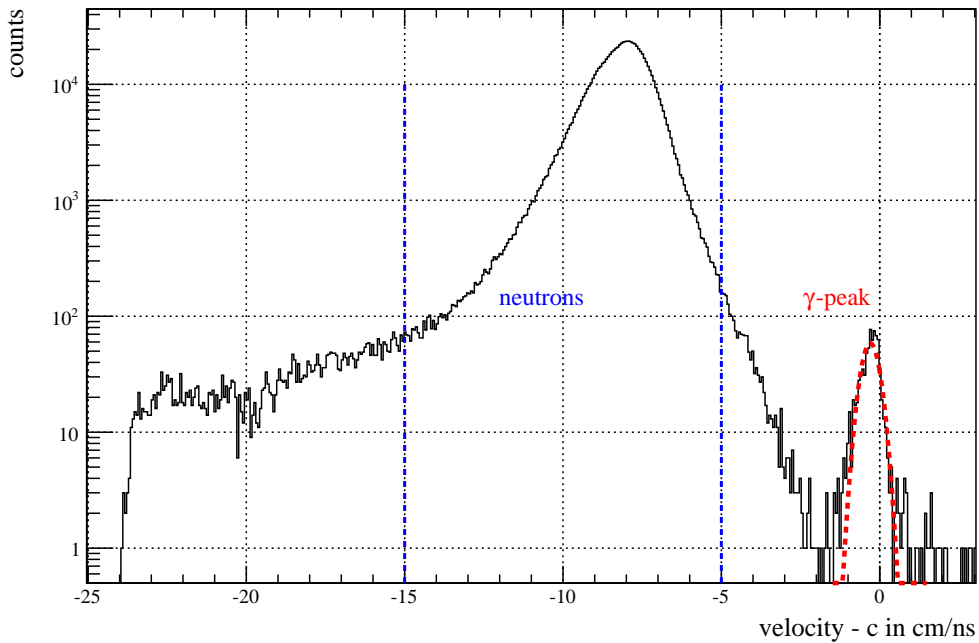
Figure 4.10: Shown is the reconstructed velocity of particles detected in LAND minus the speed of light (c). No incoming cut is applied meaning reactions from all different isotopes in the cocktail beam are allowed. The data represents events recorded using a carbon reaction target. The γ-peak which serves to calibrate the time axis is clearly visible, its width is $\sigma \sim 450$ ps. The resolution for the ToF measurements of the neutrons can not be directly determined, but this value is smaller than the resolution determined from the γ-peak since the light output is larger for neutrons.

The magnetic field of ALADIN guarantees that only uncharged particles reach LAND; photons (γ) can be distinguished from the neutrons immediately using the ToF, see figure 4.10. Since there is a small probability that a γ produces secondary particles, the shower algorithm uses a small cone behind the first hit as well as a short time window to look for further hits which could be assigned as secondaries [Ebe98].

When analyzing a 1n channel the further tasks are rather trivial. The algorithm sorts all hits according to their hit-time. The first one is used as primary hit and all others are assigned as secondary hits. But since for the ^{26}O channel the detection of two neutrons is necessary, the procedure has to be more elaborated. To find all primary hits which characterize a neutron, the following procedure is applied event-by-event:

1. Choose the first hit in time as primary hit.
2. Check all remaining hits if they can be secondaries of the first hit.
3. Continue at (1) until all hits are either declared secondary or primary hits.
4. If several neutrons have been found, check the distance between each first hit and all secondary hits and assign the secondary hits again to the closest primary hit. This step is needed to get a correct deposited energy of the shower.

A hit has to fulfill the following conditions to be considered as a secondary hit:

1. The distance in space to the primary hit has to be smaller than R_{max}.
2. The distance in time to the primary hit has to be smaller than T_{max}.
3. Due to the time resolution of LAND (σ_t), it is not possible to discriminate hits which come too close to each other. For that reason, all hits which are inside a sphere determined by the time resolution and the speed of light and in which therefore causality cannot be checked are assigned as secondary hits.
4. A cylindrical cut is applied. The cylinder is defined by a depth which is given by a distance in beam direction Z_{max} and against beam direction Z_{min}, and as third parameter the radius R_{cyl}. Within this cylindrical cut, it is checked if the location of the hit can be reached from the primary hit by a velocity smaller than the speed of light. If this condition is fullfilled the hit is treated as a secondary.
5. A further condition called 'backward Fermi' tests two requirements. First the velocity connecting two hits has to be smaller than v_{Fermi}, which is the velocity corresponding to the fermi momentum of a nucleon inside the nucleus. And second it is tested, if the relative distance between the two hits is negative, meaning that the potential secondary hit is backward relative to the beam direction.
6. The last condition checks if the neutron was scattered forward elastically. This is done by comparing the momentum which connects the two hits to the momentum one would get if a elastic scattering had taken place.

The described seven parameters of the shower algorithm have to be optimized such that the performance of the algorithm is ideal for the analyzed physics channel. In the

analysis presented here it is crucial that as few 2n events are shifted to the 1n channel as possible. To investigate the optimum shower parameters, simulations using the LEG[*] were done. A three-body decay (fragment and two neutrons) was simulated, the LAND shower algorithm was used to reconstruct neutrons, and the two most crucial parameters R_{cyl} and σ_t were changed. Having a real 2n event, one will with a certain probability detect 1n, 2n, 3n and so on. The probability to detect 1n for a generated 2n event as a function of R_{cyl} and σ_t is shown in figure 4.11.
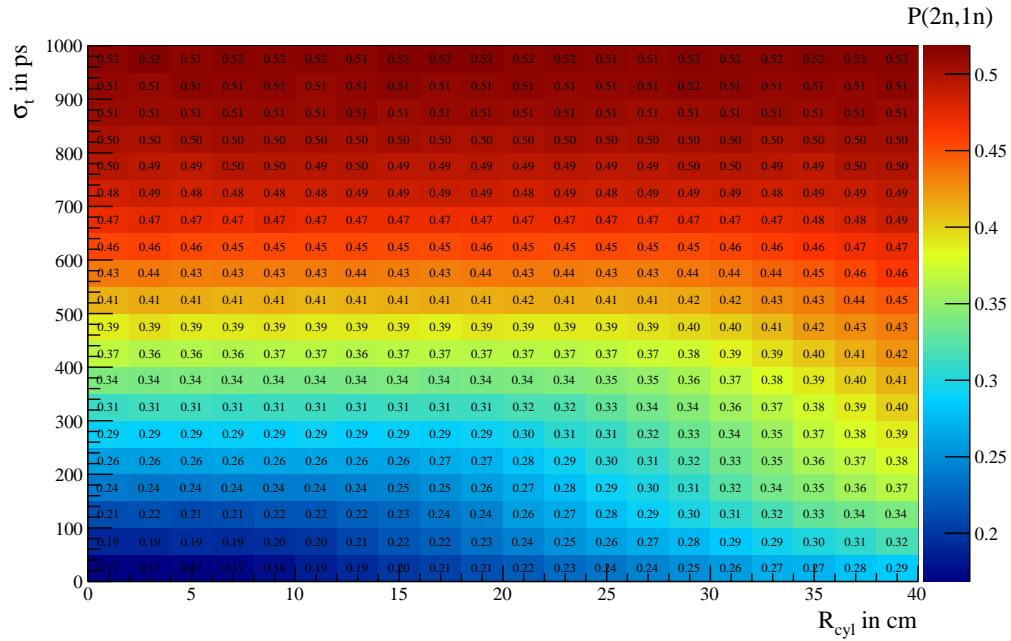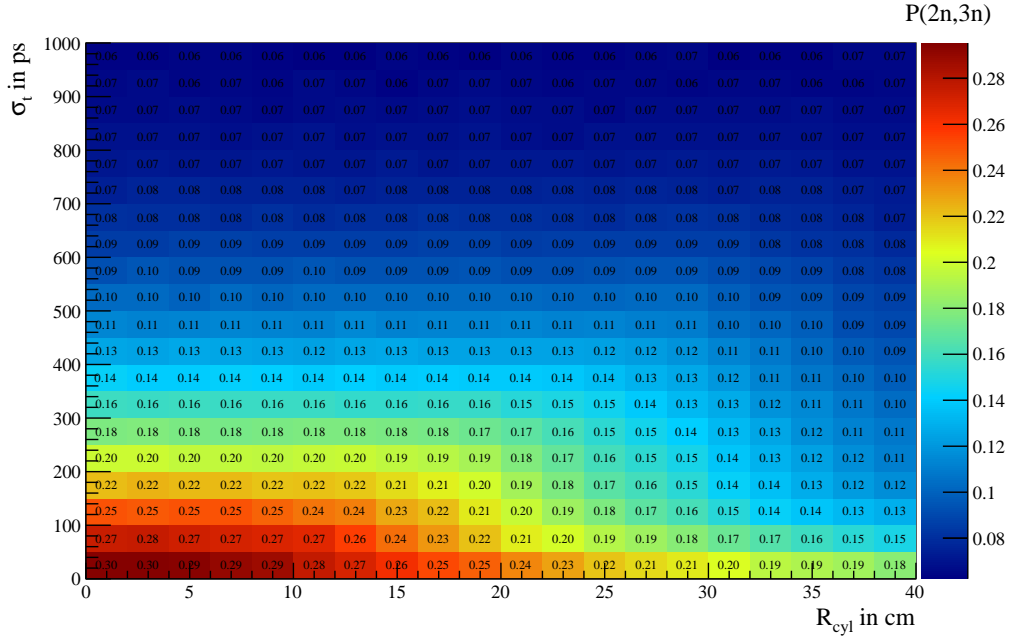
Figure 4.11: Probability to detect one neutron for two generated neutrons (P(2n,1n)) as a function of the two parameters σ_t and R$_{cyl}$ used in the shower algorithm.

The probability to detect 2n for a generated 2n event as a function of R_{cyl} and σ_t is shown in figure 4.12. In this figure two effects are clearly visible: having a large shower volume, the events are shifted to the 1n channel, while having a very small shower volume shifts events to the 3n channel. It can clearly be seen that in the area in which in figure 4.12 the values drop (left lower corner), the probability increases in figure 4.14. As mentioned earlier, the parameters have to be chosen such that as few 2n events as possible are shifted into the 1n channel. Following this argument that shifting to a higher neutron multiplicity is acceptable but shifting events to lower multiplicity is forbidden, one would simply take the smallest shower volume possible. But this would lead to the effect that one uses each hit as a primary hit and gets therefore wrong primary hits meaning wrong parameters describing the neutrons. To find the optimum parameters

---

[*]<u>L</u>AND <u>E</u>vent <u>G</u>enerator

the following ratio was used: $P(2n,2n)^2/P(2n,1n)$. Where $P(2n,2n)$ is the probability to detect a real 2n as 2n and $P(2n,1n)$ is the probability to detect a real 2n as 1n. The ratio is shown in figure 4.13
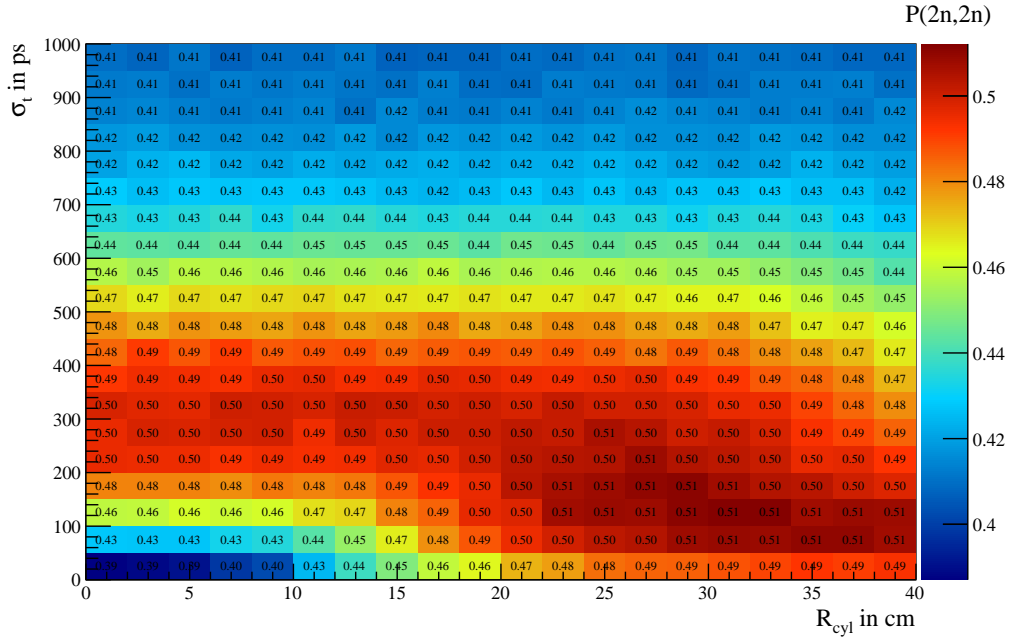
Figure 4.12: Probability to detect two neutrons for two generated neutrons ($P(2n,2n)$) as function of the two parameters σ_t and R_{cyl} used in the shower algorithm.

As a compromise between shifting as few events as possibly to the 1n but on the other hand also not to create fake primary hits, R_{cyl}=20.0 cm and σ_t=0.2 ns were used; this 'point' is also highlighted in figure 4.13. The full set of used parameters of the shower algorithm is shown in table 4.1.

parameter-name	used value
R_{max}	20.0 cm
T_{max}	5.0 ns
σ_t	0.2 ns
Z_{max}	20.0 cm
Z_{min}	-12.0 cm
R_{cyl}	20.0 cm
v_{Fermi}	8.0 cm/ns

Table 4.1: parameters used for the LAND shower algorithm.

Using a too large shower volume in the shower algorithm leads to the fact that small relative angles between the neutrons are not possible. Figure 4.15 shows the relative
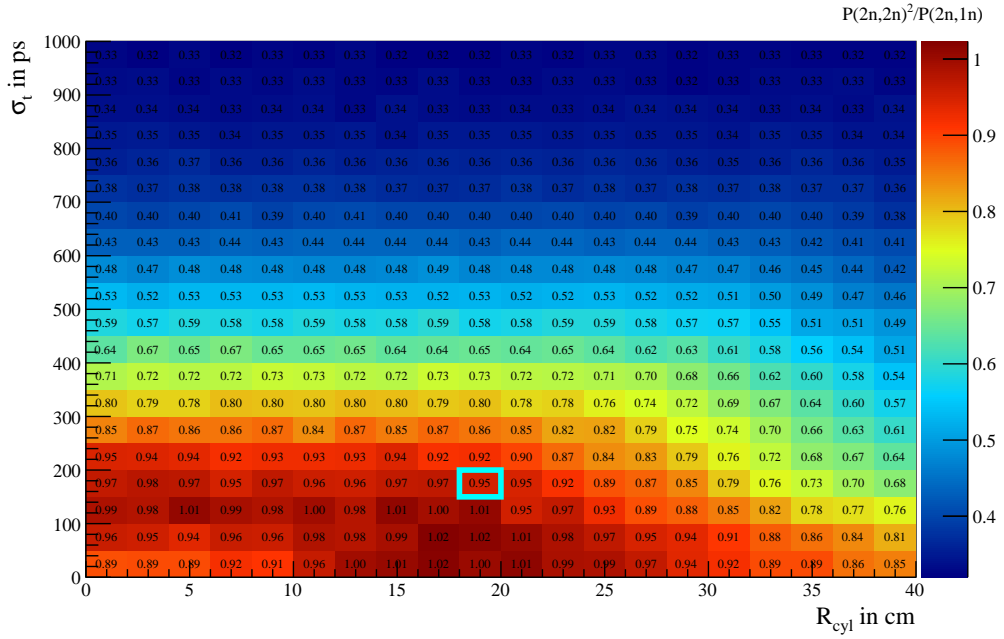
Figure 4.13: Ratio of $P(2n,2n)^2/P(2n,1n)$ used to optimize the shower parameters. The optimum is indicated as light-blue box.

Figure 4.14: Probability to detect three neutrons for two generated neutrons ($P(2n,3n)$) as a function of the two parameters σ_t and R_{cyl} used in the shower algorithm.

53

angle between two neutrons seen from the breakup of ^{6}He into an α and two neutrons. The same is shown in figure 4.16 but for a simulation which uses a flat distribution for the ^{6}He decay between S_{2n} and 2 MeV. In both cases it is clearly visible that the large shower volume cuts the small relative angles and therefore small energies in the E_{rel} spectrum making this set of shower parameters unusable for the physics channels analyzed here.
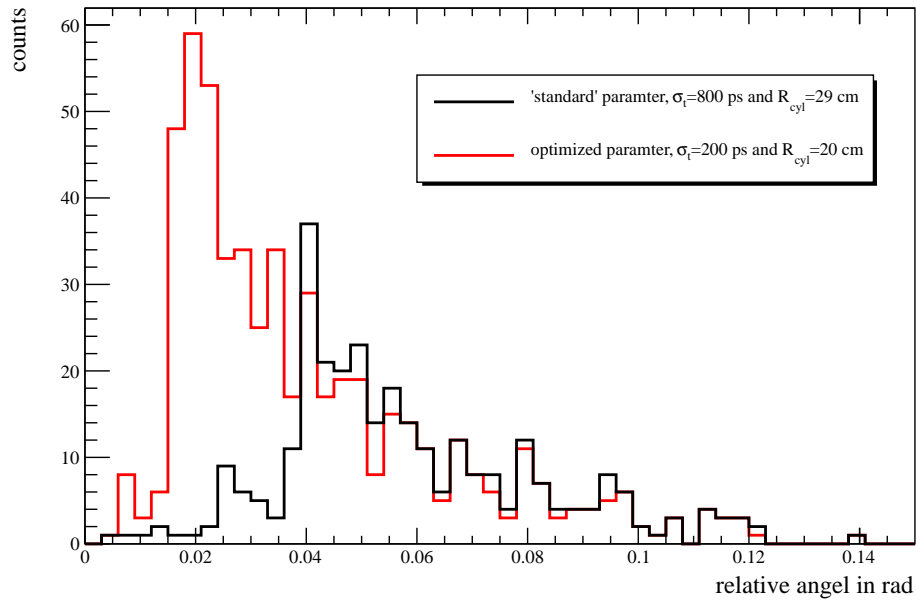
Figure 4.15: The relative angle between two neutrons seen from the breakup of ^{6}He into an α and two neutrons obtained from experimental data using two different sets of parameters for the shower algorithm is shown.
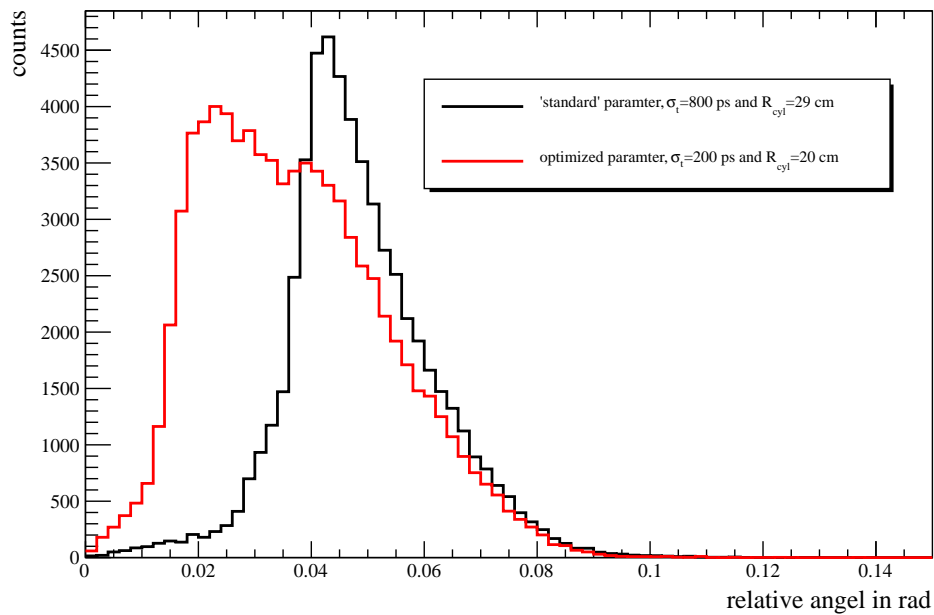
Figure 4.16: The relative angle between two neutrons seen from the breakup of ^{6}He into an α and two neutrons obtained from simulations using LEG with two different sets of parameters for the shower algorithm is shown.

Chapter 5

Analysis

In the last chapter it has been discussed how to select the outgoing fragments and neutrons as well as how to determine their four-momenta. Using these quantities together with formula (3.6), the relative energy can be reconstructed. The obtained energy spectrum is still affected by efficiency, acceptance and response of the experimental apparatus. These effects have to be accounted for to determine the real resonance position and width. The individual steps from the measured data to the final interpretation will be described in the following sections.

5.1   Detector Response / LEG Simulation

Analyzing data taken with any detector rarely gives directly the original physics quantity. The response of a detector to a monoenergetic source will, e.g., distribute the energy over many channels according to the gain and energy resolution of the detector and readout electronics. This resolution function is usually relatively complicated and depends on the input distribution as well as on the detector settings (threshold, HV[*], etc.) and the analysis procedures (in case of LAND e.g. on the shower parameters, see section 4.2). Since the final goal of the analysis is to reconstruct the real energy, it is convenient to table the response of the detector while the real energy serves as a parameter. This lookup table is simply a matrix and gives the data set the name *detector response matrix*. Often the detector response matrix is normalized to the number of simulated events. A detector response matrix is commonly determined by using known values as input for a simulation and generating the output including all individual steps, e.g., neutron conversion to charged particles, scintillation process, light transport through the paddle, etc. Using a complex experimental setup like the LAND-R^{3}B-setup which is composed of several detectors, one would have to combine the response of all detectors to extract physics from the measured data. However, in the analysis presented here, the

---

[*]<u>H</u>igh-<u>V</u>oltage

experimental response of the full setup is mainly determined by LAND since in the full analysis a neutron trigger was required and no acceptance cut is seen in the fragment distributions. Furthermore, the CB which is normally the other main contribution to the response is not needed in the presented analysis.

To determine the LAND response matrix, real neutron data from a calibration experiment serve as input. This data is stored in a database, from which hit patterns are taken and those are shifted to the location of the neutron interaction which has been simulated by the LEG. For the digitizer, the thresholds have to be given for each individual channel and the data reconstruction is done using the earlier described shower algorithm, this entire procedure is combined in the so called LEG. The LEG simulations presented here were done by D. Rossi. The particle decay was simulated using the `GENBOD` (`CERN` library N-Body Monte-Carlo Event Generator) [Jam]. Since ^{24}O does not have bound excited states (see e.g. figure 7.4), no γ's have to be included in the simulation.

The efficiency of LAND is directly influenced by broken detector channels. During the s393-experimental champaign, the LAND paddles listed in table 5.1 could not be used for the data analysis.

plane	paddle
1	1
1	20
2	19
6	6
6	13
7	17
9	1
9	12
9	20
10	completely

Table 5.1: Shown are LAND channels which could not be used for the data analysis. Plane 10 was read out using the new TacQuila electronics, and is excluded from this analysis.

These paddles are switched off in the simulation. In a second step, the individual threshold of each channel has to be given to be able to match the experimental and the simulated data. The thresholds are determined from the experimental data using the procedure described in [Ros09]. As further input parameter also the experimentally determined light attenuation length of each paddle is used in the simulation. This quantity is determined via the standard LAND calibration using the routine called `cosmic1`. The validity of the simulation is good, if the simulated hit multiplicity distribution repro-

duces the experimental one. A perfect agreement is found within error bars, as can be seen in figure 5.1.
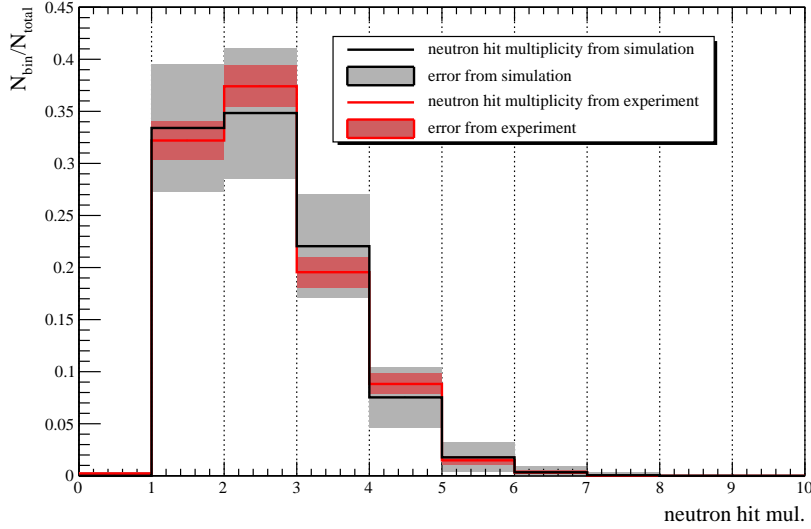
Figure 5.1: Shown are the neutron hit multiplicities for a 1n channel, once obtained from simulation and once using experimental data. Both histograms are normalized to one.

The results of the simulations for four important channels (1n→1n, 1n→2n, 2n→1n, 2n→2n, where the notation means: generated→tracked) are shown in figure 5.2 and figure 5.3, respectively. Projecting these two-dimensional spectra over the full range onto the y-axis results in the one-dimensional efficiency × acceptance curve such as e.g. shown in figure 6.1. In the upper panel of figure 5.3 (2n→1n), two correlation regions can be seen. For small energies, the two neutrons interact in LAND so close to each other, that they are sorted in the shower algorithm into one shower volume. At large energies, one of the neutrons has such a large angle that it does not hit LAND, this is the so called acceptance cut. In the one-dimensional projection (figure 6.1), the decrease of efficiency at approximately $E_{rel} \sim 3.5$ MeV can be seen, reflecting the acceptance cut, which depends on the neutron kinetic energy only. The acceptance is 100% up to $E_{rel} \sim 3.5$ MeV, for higher energies a fraction of neutrons does not hit LAND, since a higher neutron kinetic energy means that the neutron has a larger angle relative to the fragment (beam axis). In the lower panel of figure 5.3 (2n→2n) it can be seen that the correlation bends for low energies away from the diagonal. This reflects again the fact that neutrons which come too close to each other cannot be resolved.

The overall efficiency of LAND shown in figure 6.1 seems to be at a first glance too low. The nominal LAND efficiency for the detection of one neutron at ~ 500 MeV is 95% [BGI+03]. However, when using a rather small shower volume, see table 4.1, a part of the true 1n events are seen as 2n. This issue is overcome in the analysis in the

following way. The ^{25}O-channel is analyzed using as condition: LAND-track-multiplicity (Ntmul)>1. This can be done since for incoming ^{26}F and outgoing ^{24}O there can be a maximum of one neutron[*]. In the ^{26}O-channel very little real 1n events are expected. Furthermore, their position in energy is known from ^{25}O which allows us to look for this signature. No large contamination from this channel is found as discussed later, see figure 6.3 lower pad. In summary, one can say that as stated before, shifting to higher neutron multiplicity is acceptable for the present analysis.

The slow increase in efficiency seen below $E_{rel} \sim 3.5$ MeV can be explained as follows: the larger the relative energy the larger the angle and therefore the larger the irradiated area in LAND. This effect reduces the impact of dead zones (high thresholds or broken channels) as a function of the relative energy.
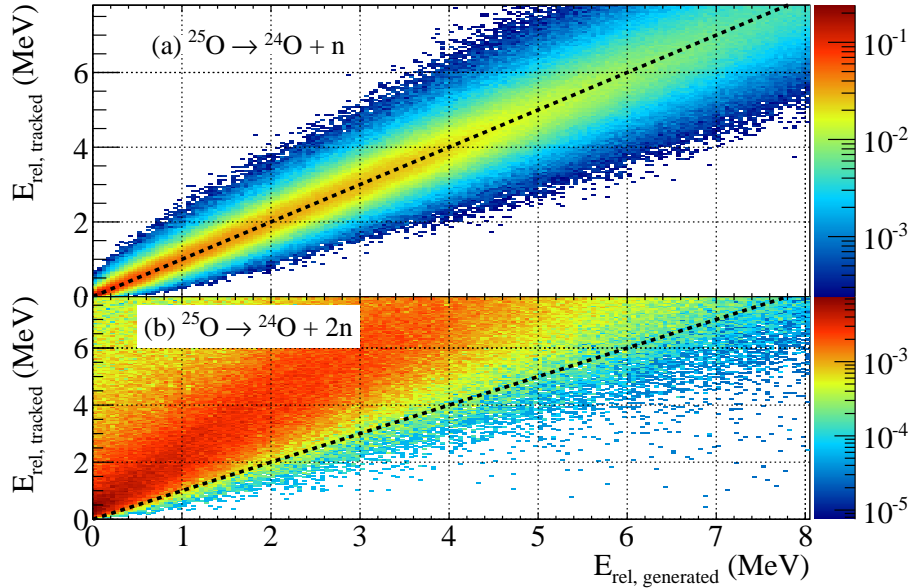
Figure 5.2: Shown are the response matrices of LAND for the 1n→1n (a) and 1n→2n (b) channels. Meaning for both spectra one neutron has been generated. The upper panel represents the response matrix for which this one neutron has been reconstructed correctly. In the lower panel the response matrix is shown for which a second (fake) neutron has been reconstructed by the analysis procedure. The dotted black line represents the diagonal.

---

[*]Assuming that the charge (Z) and mass (A) identification is to 100% correct.
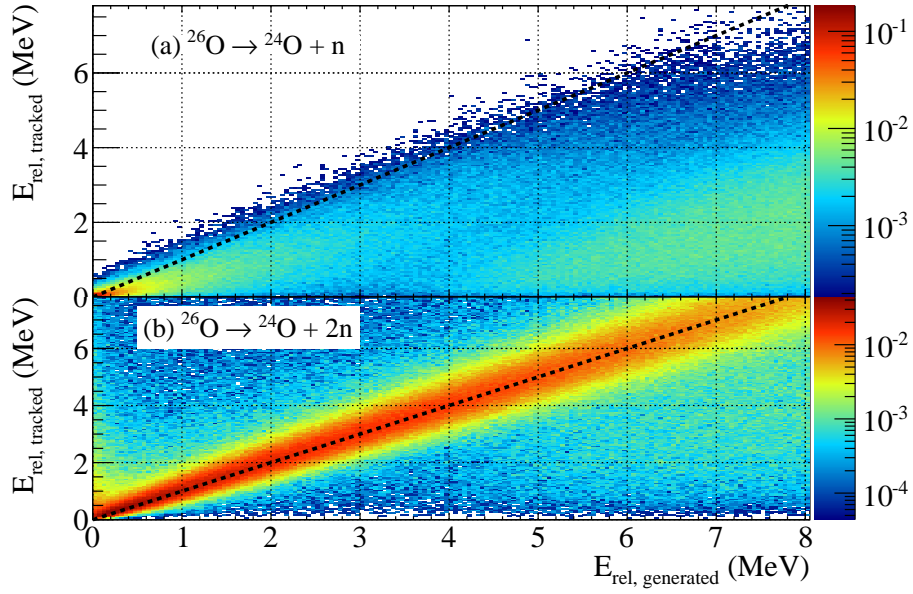
Figure 5.3: Shown are the response matrices of LAND for the 2n→1n (a) and 2n→2n (b) channels. The dotted black line represents the diagonal.
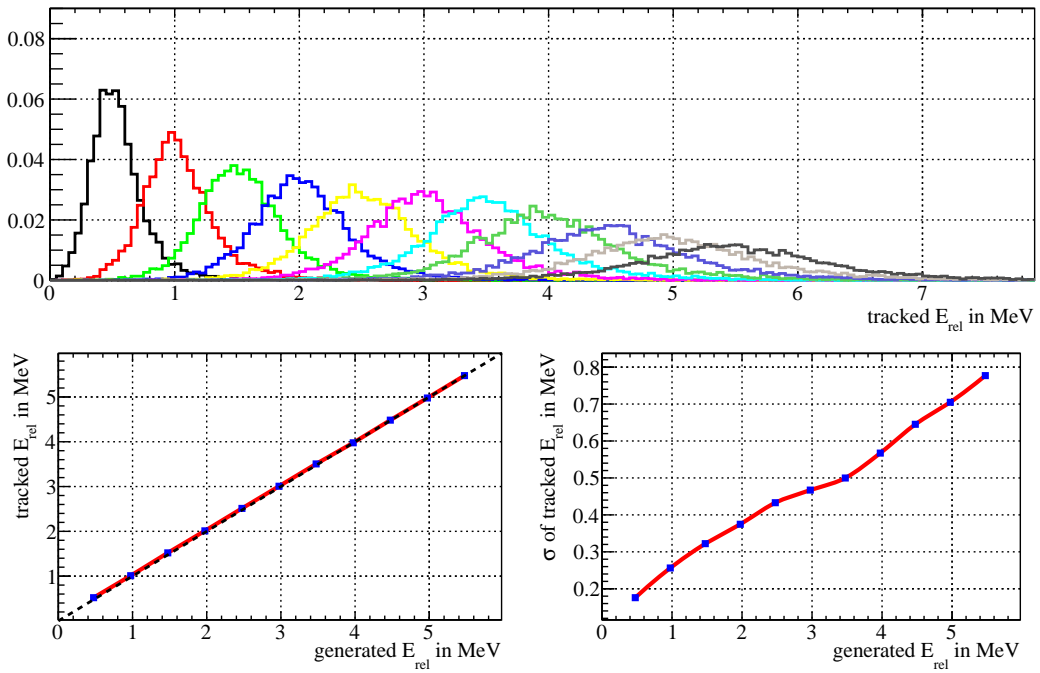
Figure 5.4: Upper pad: Eleven projections of the response matrix shown in the upper panel of figure 5.2 are depicted in different colors. The corresponding generated energy to the eleven shown spectra is $i \times 500$ keV where 'i' is 1 to 11. The individual distributions are fitted using a gaussian. The peak position as well as the sigma is determined. Lower left pad: The generated vs. tracked energy is shown. The correlation follows almost perfect the diagonal (black dotted line), only for small energies it bends slightly. Lower right pad: generated energy vs. resolution of the tracked energy is shown.

61

5.2 Breit-Wigner Line Shape

After discussing in the last section (5.1) how the detector response matrix is obtained, the next step is to convolute it with an input function. In the final step this 'test model' is then compared to the experimental data using χ^2 methods, described in section 5.3.

The standard function to describe a resonance is the so called 'Breit-Wigner resonance'. This line shape as given in the one-level approximation is a function which depends on the relative energy (E) and two ('fit') parameters:

- resonance energy E_r,
- reduced width γ.

For the amplitude an additional factor is later on used which scales the integral of the function to match the experimentally found integral. The Breit-Wigner line shape has the following form [LT58]:

$$f(E; E_r, \gamma) = \frac{\Gamma}{(E_r + \Delta - E)^2 + 1/4 \cdot \Gamma^2} \ , \tag{5.1}$$

with:

- $\Gamma = 2P_l(E) \cdot \gamma^2$,
- $\Delta = (S_l(E_r) - S_l(E)) \cdot \gamma^2$.

The energy (E) and angular momentum (l) dependent functions $P_l(E)$ and $S_l(E)$ can be taken from [BM69]*. For the angular momentum $l = 2$ is used due to the following argument. The Breit-Wigner line shape is used to describe the ^{25}O resonance. The additional neutron of ^{25}O compared to ^{24}O is in the $0d_{3/2}$ - shell, while for ^{24}O the highest occupied neutron energy level is $1s_{1/2}$, see figure 1.2. Therefore, one finds for the ^{25}O decay, from a $3/2^+$ state to the 0^+ ground state of ^{24}O, $\Delta l = 2$, which leads to:

$$P_2(E) = \frac{\rho^5}{9 + 3\rho^2 + \rho^4} \ , \tag{5.2}$$

$$S_2(E) = -\frac{18 + 3\rho^2}{9 + 3\rho^2 + \rho^4} \ , \tag{5.3}$$

with:

$$\rho = k \cdot R = \frac{\sqrt{2\mu E}}{\hbar c} \cdot R \ . \tag{5.4}$$

Where k is the relative momentum and μ is the reduced mass. R is commonly called channel radius, in [BM69] e.g. the 'better' description *range of the potential* is used. This parameter divides the configuration space in the R-matrix formalism into an internal and an external region, and has to be chosen such that R is larger than the radius of the

---

* [BM69] contains a 'typo' in formula (3F-38) for Δ_l, here a factor '$k \cdot R$' is missing [Chu12].

potential. This condition ensures that in the external region ($r > R$) only the asymptotic part of the wave function has to be accounted for. Since every choice which fulfills that R is larger than the size of the nuclear potential is suited, the channel radius has no direct physical meaning. It is only needed for computational purposes. As a consequence one can use the independence of the obtained physics results (resonance position and width) on the channel radius as a validity test [DB10].

The Breit-Wigner line shape as given in the one-level approximation can also be used to determine the single-particle width of the state using:

$$\Gamma_{sp} = \frac{2(\hbar c)^2}{\mu R^2} \cdot P_l(E) \cdot \frac{2l-1}{2l+1} \, , \tag{5.5}$$

which is for $l = 2$:

$$\Gamma_{sp} = \frac{2(\hbar c)^2}{\mu R^2} \cdot \frac{\rho^5}{9 + 3\rho^2 + \rho^4} \cdot \frac{3}{5} \, . \tag{5.6}$$

Using the resonance position ($E = E_r$) yields the single particle width. The value obtained from formula (5.6) depends strongly on the choice of the channel radius in contrast to the fit to the data, which is, as pointed out before, insensitive to this parameter [Vog08]. In the literature the following values can be found: Hoffman *et al.* [HBB$^+$08] state: '*The distribution was found to be insensitive to the size of the channel radius between 5.44 and 5.83 fm*', the origin of these particular values is not explained. In the same paper, a '*single-particle decay width of 79 keV, calculated for the $l = 2$ ground state neutron decay of ^{25}O at 770 keV*' is given. To reproduce the width for the given resonance position using formula (5.6), a channel radius of R=4.15 fm has to be used. The matter radius of ^{24}O is 3.19±0.13 fm [OST01]. Using the empirical relation to calculate the charge radius from the mass number (A): $R \approx (1.2 \cdot A^{1/3})$ fm for ^{25}O ($A = 25$) one obtains 3.5 fm[*]. To test the sensitivity of the Breit-Wigner function on the channel radius, the following parameters have been used:

- Peak position: $E_r = 0.737$ MeV.
- Width: $\Gamma = 0.072$ MeV.
- Fragment mass: $M_F = 24.0205$ u.
- Neutron mass: $M_n = 1.0087$ u.

for the ^{24}O+n system. The radius has been varied between 3.5 and 6 fm. As expected, it is found that the line shape is not very sensitive to this value, see figure 5.5. Considering this and all the different values found in literature and given above, a channel radius of R=4 fm has been used during the analysis.

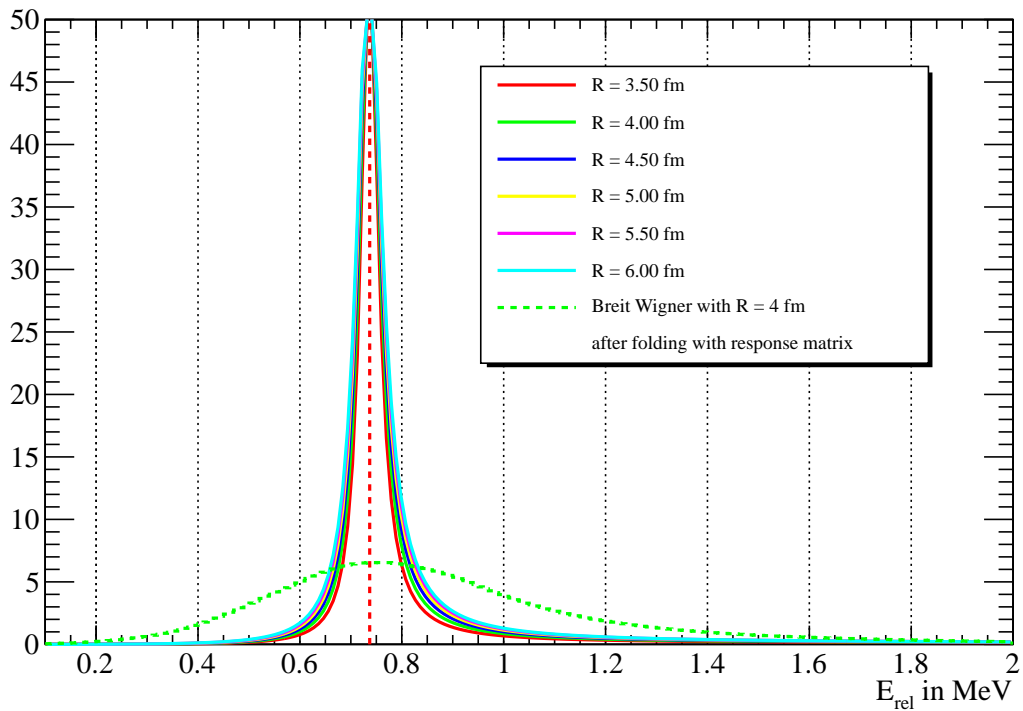[*]This relation is here only used to get a 'figure of merit'.

Figure 5.5: Breit-Wigner line shape as given in the one-level approximation for fixed E_r and Γ. The radius R has been changed between 3.5 and 6.0 fm. It can be seen that the line shape is not (very) sensitive to the channel radius. The dotted line represents the Breit-Wigner line shape for $R = 4$ fm folded with the response matrix shown in the upper panel of figure 5.2. It is shown that a substantial part of the experimentally observed width is due to the experimental response and not due to the original width of the state. The folded function is normalized to the area of the original function.

5.3 Chi-Square (χ^2) and Likelihood Methods

Having a test function on one side and the experimental data on the other side, it has to be determined how good this test function describes the experimental data. In an analysis framework like, e.g., `ROOT`, this is commonly done using standard χ^2 methods. In general several different approaches are applicable. Those deliver very similar results in case of a high-statistics data samples. But are not all usable in the case of a low statistics experiment. Different methods will be described here following the ideas described in [BR69] and [BC84]. The used notation is:

$$
\begin{aligned}
n_i &= \text{number of events in the } i^{th} \text{ bin (experimental measurement)} , \\
N &= \text{total number of events; } N = \sum_{i=1}^{N} n_i , \\
y_i &= \text{number of events predicted by the model to be in the } i^{th} \text{ bin} , \\
N_0 &= \text{total number of events predicted by the model; } N_0 = \sum_{i=1}^{N} y_i .
\end{aligned}
$$

For the commonly used χ^2 tests two choices are possible:

1. errors based on the sample data == Neyman's chisquare (χ^2_N), see figure 5.6 and formula (5.7),

2. errors based on the parent distribution == Pearson's chisquare (χ^2_P), see figure 5.7 and formula (5.8),

where the names are taken from [BC84]. This leads to the following two formulae for χ^2:

$$
\chi^2_N = \sum_{i=1}^{N} \frac{(n_i - y_i)^2}{n_i} , \tag{5.7}
$$

$$
\chi^2_P = \sum_{i=1}^{N} \frac{(n_i - y_i)^2}{y_i} . \tag{5.8}
$$
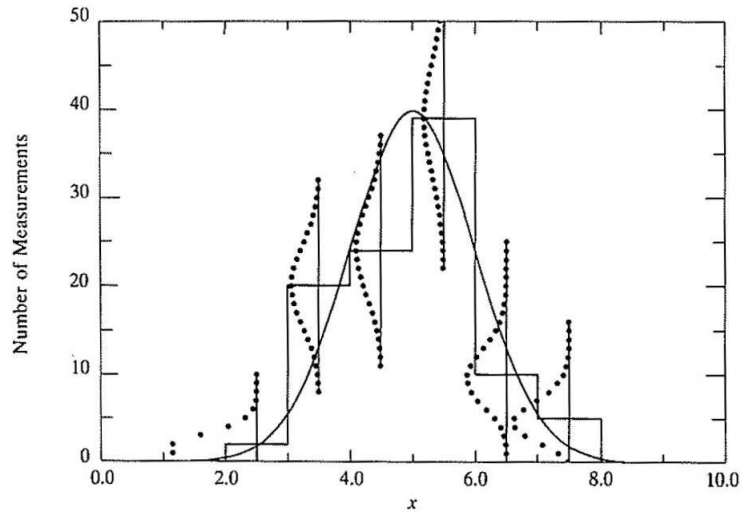
Figure 5.6: Histogram, drawn from a Gaussian parent distribution with mean $\mu=5.0$ and standard deviation $\sigma=1$, corresponding to 100 total measurements. The parent distribution $y(x_j)=NP(x_j)$ is illustrated by the large Gaussian curve. The smaller dotted curves represent the Poisson distribution of events in each bin, based on the sample data. Figure is taken from [BR69].
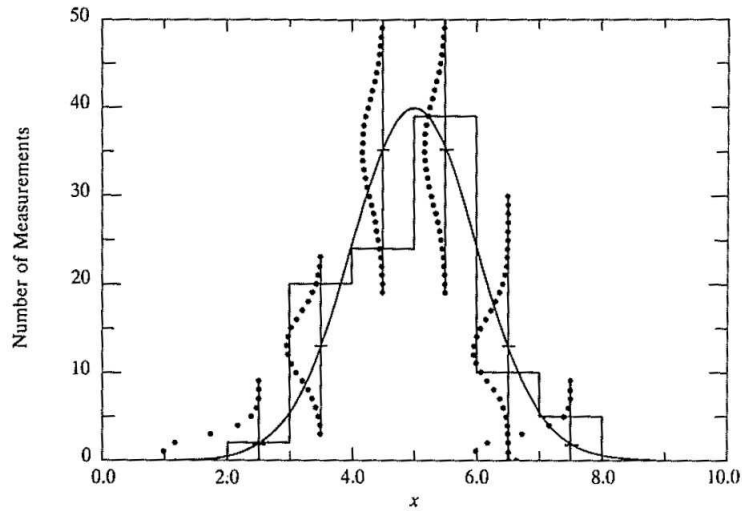
Figure 5.7: The same histogram as shown in figure 5.6 with dotted curves representing the Poisson distribution of events in each bin, based on the parent distribution. Figure is taken from [BR69].

Besides χ^2-tests likelihood methods are commonly used to test how good a certain distribution describes a test sample. Starting from the Poisson probability (formula (5.9)) and applying the method of maximum likelihood which is equivalent to maximize its natural logarithm one can convert this again to a χ^2, see formula (5.12). Were the general relation between a probability distribution and χ^2 (formula (5.11)) is used.

$$P_P(y,n) = \prod_{i=1}^{N} \left(\frac{(y_i)^{n_i}}{(n_i)!} \cdot e^{-y_i} \right) \ , \tag{5.9}$$

$$\ln(P) = \sum_{i=1}^{N} \left(n_i \cdot \ln(y_i) - y_i \right) + const \ , \tag{5.10}$$

$$\chi^2 \simeq -2 \cdot \ln(P) \ . \tag{5.11}$$

The derived χ^2 will here be called BEPL* and can be expressed in the following way:

$$\chi^2_{BEPL} \simeq 2 \cdot \sum_{i=1}^{N} \left(y_i - n_i \cdot \ln(y_i) \right) \ . \tag{5.12}$$

In [BC84] a likelihood-ratio λ is formed and then a χ^2 is calculated using again formula (5.11) were λ is used instead of the probability function (P). The likelihood-ratio λ is built using the probability distribution (e.g. Poisson, see equation (5.9)) divided by the distribution which one would get using the true values (m) if there were no errors

$$\lambda = \frac{P(y,n)}{P(m,n)} \ . \tag{5.13}$$

Replacing m by n and taking the natural logarithm (ln) one gets for χ^2 (which will here get the index BAPL[†]):

$$\chi^2_{BAPL} \simeq 2 \cdot \sum_{i=1}^{N} \left(y_i - n_i + n_i \cdot \ln(n_i/y_i) \right) \ . \tag{5.14}$$

Furthermore in [BC84] also a multinominal likelihood is given, which is derived replacing the Poisson by the multinominal distribution:

$$P_m(y,n) = N! N^N \prod_{i=1}^{N} \left(\frac{(y_i)^{n_i}}{(n_i)!} \right) \ , \tag{5.15}$$

---

[*]<u>BE</u>vington's <u>P</u>oisson <u>L</u>ikelihood
[†]<u>BA</u>ker's <u>P</u>oisson <u>L</u>ikelihood

this leads to a χ^2 which will here get the index BANL*:

$$\chi^2_{BANL} \simeq 2 \cdot \sum_{i=1}^{N} \left(n_i \cdot \ln \left(n_i / y_i \right) \right) \ . \tag{5.16}$$

χ^2_{BAPL} (formula (5.14)) and χ^2_{BEPL} (formula (5.12)) are the same despite a constant term and give therefore the same minimum. This can well be seen in figure 6.2 comparing the two spectra in the middle row (pad C and D). Both spectra look exactly the same and deliver the same minimum, but the scale of both histograms is different, which reflects the constant which is neglected for χ^2_{BEPL}. Equation (5.16) and (5.14) have the problem that they can not deal with empty bins. For $n_i = 0$ the logarithm is not defined, this problem is solved by replacing the corresponding summand by zero.

The five methods (χ^2_P, χ^2_N, χ^2_{BEPL}, χ^2_{BAPL} and χ^2_{BANL}) described so far are all used in the following procedure (see next chapter):

1. Fold test input function to response matrix (figure 5.2 or figure 5.3).
2. Do a y-projection of the obtained two dimensional matrix.
3. Use this function (e.g. shown in figure 5.5) and the experimental data to calculate a χ^2 with the corresponding formula.

As an alternative (6th) method the following procedure can be used to construct a χ^2: The measured relative energy is used event-by-event. A x-projection of the response matrix, see e.g. figure 5.3, for a small y-region, serves as probability distribution. The y-region is chosen such that it reflects the measured relative energy. The obtained probability distribution gives the probability to which the measured relative energy corresponds to a certain real energy. Such a probability function is selected for each event. The individual probabilities are then multiplied to an overall probability. This overall probability can again be converted to a χ^2 using formula (5.11). And is called χ^2_{prob} in the context of this thesis. The methods χ^2_P, χ^2_N, χ^2_{BEPL}, χ^2_{BAPL} and χ^2_{BANL} and χ^2_{prob} will be referred to as method 'A' to 'F' in the following chapter.

The various χ^2 methods have been investigated to gain confidence that the results do not depend on the analysis procedure. This can be underlined by the following citation: *'For finite sample size (small N) general results are lacking; one must carefully study the problem at hand in order to choose and interpret a test statistic.'* [BC84]. Method A can not handle empty bins correctly, since the assigned error is zero. Method B assumes that the real distribution is known already in advance which is in most cases not true. While methods A and B both assume that the error is described by $\sqrt{N}$ methods C and D use a Poisson distribution to describe the error. This is for low statistics the better choice. As conclusion one has to say that even for the very low statistics of the present experiment

---

*<u>BA</u>ker's <u>N</u>ominal <u>L</u>ikelihood

all methods give the same result within error bars, see next chapter. However, the different analysis procedures are kept, to proof the robustness of the analysis.

It has to be noted, that for method C and F the absolute value of χ^2 has now meaning. These methods deliver the correct shape and can therefore be used to determine the minimum χ^2, but the reduced χ^2 gives no information on the goodness of the fit.

Chapter 6

Results

In the last two sections it has been discussed how a test function is generated including e.g. detector response as well as how to compare this function to the experimental data. The described procedures will now be applied to the obtained relative-energy spectra.

6.1   Analysis of the ^{25}O Channel

Analyzing the ^{26}F $\rightarrow ^{25}$O $\rightarrow ^{24}$O + n reaction, the relative energy spectrum of ^{25}O and therefore its mass is reconstructed, see figure 6.1. The relative energy of the ^{24}O + n system depicts the data in the 0 to 8 MeV range, one sharp resonance can directly be seen at approximately 700 keV. The acceptance cut is at roughly 3.5 MeV and does therefore not influence the observed shape at all. This is one disadvantage of the previously performed measurement at NSCL. The setup used there has the following property: '*In particular, the width of the measured data is almost entirely due to experimental resolution, and the shape of the data above $\sim$ 0.8 MeV is dominated by the limited acceptance at higher relative energies*' [CFA$^+$12a].

The data has been analyzed using a Breit-Wigner line shape described by formula (5.1) with a channel radius fixed at R=4 fm and Δ=0; Γ as well as E_r have been used as free fit parameters. The amplitude is chosen such that the integral of the fit function and the experimental data match. Methods A to E have been applied, the 2-dimensional χ^2 distributions are shown in figure 6.2. For empty bins an error of ± 1 was used. The width (Γ) has been changed between 0 and 500 keV, the peak position (E_r) was varied between 500 and 1000 keV for both quantities 5 keV steps have been used. The results obtained from the different 'fits' are shown in figure 6.2 and given in table 6.1.

An overall agreement on the peak position (E_r) and the width (Γ) can bee seen within error bars, for the results obtained by the different methods. The uncertainty in determining the width is mainly due to the fact that the observed width is dominated

by the experimental resolution, see e.g. figure 5.5. Since it reduces the obtained errors dramatically $\Delta=0$ has been used. The results obtained including Δ and R=6 fm, which is comparable to the Breit-Wigner line shape used by Hoffman *et al.* [HBB$^+$08], is shown in appendix A.

It can be seen that χ^2_N (method A) gives a very low value for the χ^2 at the minimum, this is the case since for empty bins an error of ± 1 was assigned, and this method is the only one using these (large) errors. The final result is determined using method D, for that reason the reduced χ^2 is only given for this method. Method D is chosen over the other methods since it uses a Poisson distribution for the errors taken from the test function which is the correct parent distribution. Furthermore, this method is least sensitive to the chosen binning of the experimental data, as has been observed during the analysis. The result obtained for the ^{25}O ground state is $E_r = 737^{+48}_{-43}$ keV and $\Gamma = 72^{+126}_{-65}$ keV.

method	χ^2 at min.	E_r at min. in keV	Γ at min. in keV
A	22.71	$707\ ^{+81}_{-71}$	$228\ ^{+273}_{-167}$
B	54.93	$727\ ^{+31}_{-34}$	$127\ ^{+113}_{-58}$
C	93.62	$737\ ^{+48}_{-43}$	$72\ ^{+126}_{-65}$
D	52.85 / (55-2) = 0.997	$737\ ^{+48}_{-43}$	$72\ ^{+126}_{-65}$
E	57.22	$768\ ^{+24}_{-42}$	$1\ ^{+19}_{-0}$

Table 6.1: Given are the results analyzing the ^{25}O-data using a Breit-Wigner line shape and methods A to E. For method D the NDF is given in brackets, which is the number of bins in the fit range minus the number of free parameters in the input function.

In figure 6.1 two different theoretical predictions for the ^{25}O ground state are indicated. Those theoretical calculations have been performed by Holt *et al.* [Hol12] and Simonis *et al.* [Sim12]. Chiral EFT including three-body (3N) forces have been used, theory and experiment will be compared in chapter 7.
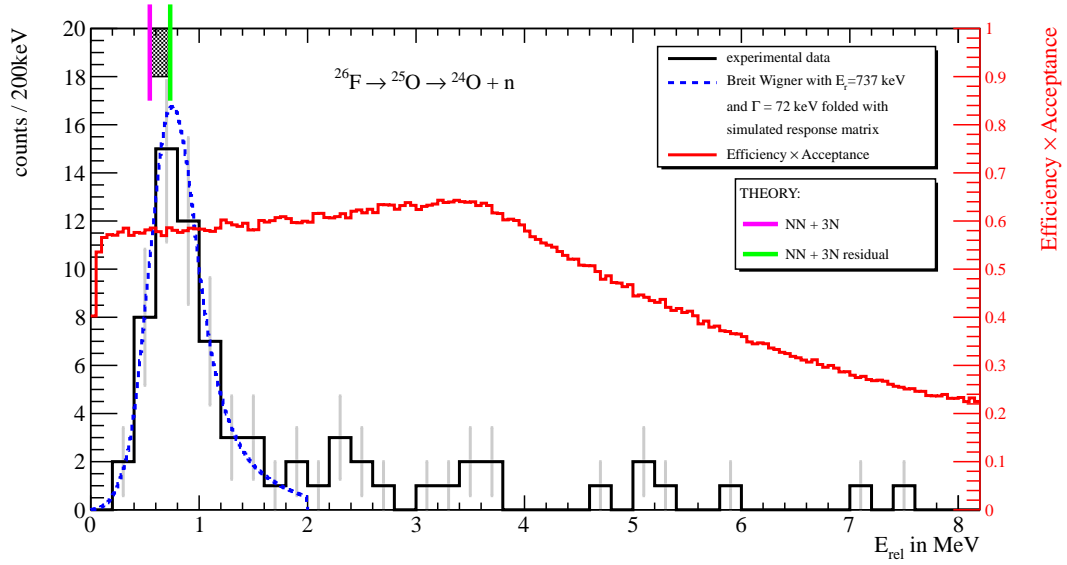
Figure 6.1: Shown is the experimental data of the relative energy for ^{25}O as black solid line. On top as blue dotted line the best fit (Breit-Wigner line shape with R=4 fm, E_r=737 keV, Γ=72 keV and Δ=0) is shown. In addition the LAND 'efficiency × acceptance' curve is shown to highlight that the observed peak is not produced by an acceptance cut. At the top of the panel two different theoretical predictions obtained using chiral EFT including three-body forces are shown.
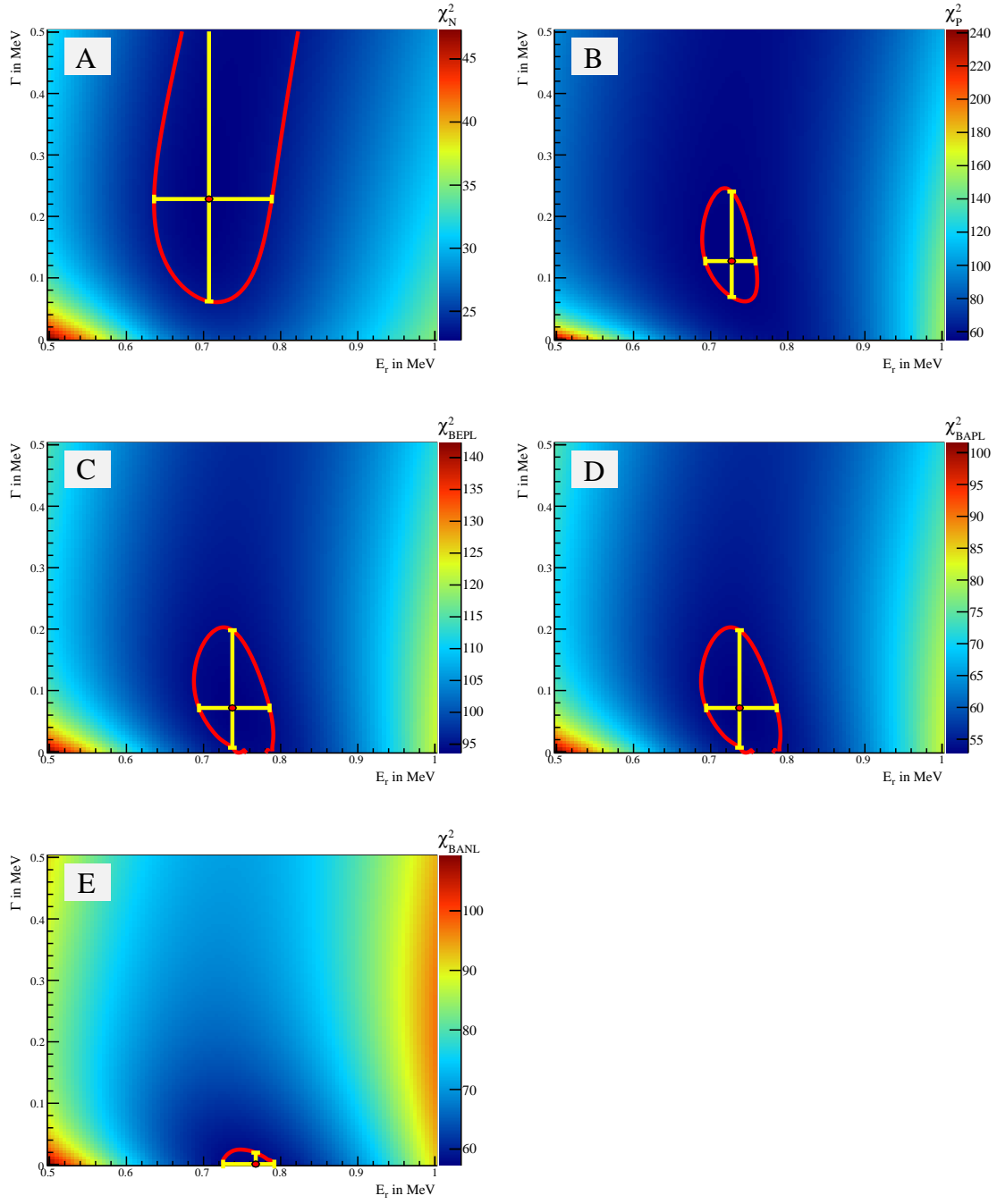
Figure 6.2: 2-dimensional χ^2 spectra are shown for methods A to E, applied to the ^{25}O-data using a Breit-Wigner line shape as described by formula (5.1). As red solid line the $\chi^2_{min} + 1$ contour is indicated in each spectrum, the yellow horizontal and vertical lines represent the errors determined using this contour. The exact values are given in table 6.1.

74

6.2 Analysis of the ^{26}O Channel

The relative energy spectrum of ^{26}O is shown in figure 6.3. Predicting the shape of this spectrum with 'hand-waving arguments' one would naively assume that it should be similar to the $E_{rel}(^{25}$O$)$, ^{26}O is a bit more exotic (larger A/Z) but on the other hand the system should gain binding energy due to pairing effects.
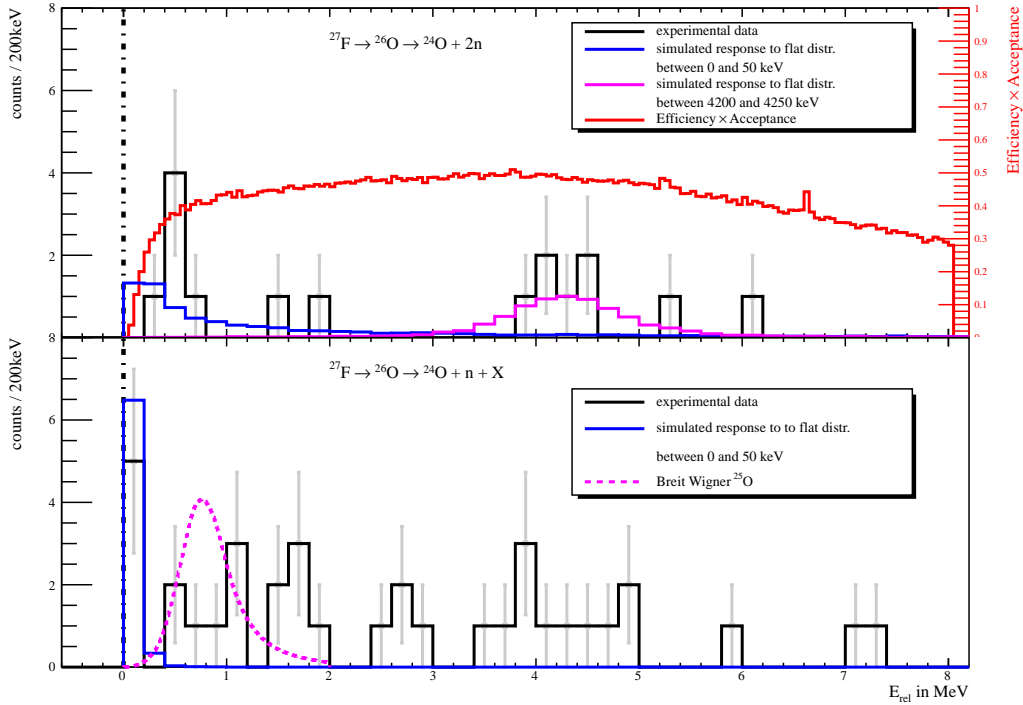
Figure 6.3: The 1n and 2n channel of the ^{26}O data are shown (upper and lower pad). The experimental data is shown as a solid black line. In blue the best fit to the low energy part of the 1n and 2n channel is shown. In purple other contributions to the 1n as well as 2n are indicated. In the upper pad the solid purple line reflects a excited state of ^{26}O, while in the lower pad the dashed purple line depicts the contribution to this channel originating from real 1n events. In the upper pad the LAND efficiency × acceptance is shown in red visualizing the cut at low energies into the 2n channel.

Analyzing the data of this reaction channel differs from the analysis procedure applied to the ^{25}O in the following sense. As discussed in section 5.1, the low-energy part of the 2n channel of this kind of reaction is shifted to the 1n channel making it necessary to analyze both channels simultaneously. Looking at the (real) 1n channel of the ^{25}O analysis (figure 6.1), one sees that no events are observed within the first 200 keV of the spectrum. Comparing this to the (fake) 1n channel found in the ^{26}O analysis, see figure 6.3 lower panel, one sees a substantial amount of events in the first 100 keV of the spectrum, which can be therefore assigned to originate from the 2n channel. Due

to the low statistic which makes it impossible to extract the width of the state, a flat distribution with a width of 50 keV was used as a test function. To fit the 1n and 2n channels simultaneously the following procedure has been applied:

1. Select test function (E_r), width is fixed to 50 keV.

2. Scale 2n test function such that the integral is the same then experimentally observed.

3. Scale 1n test function by the same factor.

4. χ^2-methods are applied to 1n and 2n simultaneously.

In total the 2n channel of the ^{26}O-data is described with a low- and a high-energy part (ground and excited state), see blue and purple contributions in figure 6.3 upper panel. The low energy part of the 1n and the 2n channel are as described above treated together. The results of these fits using method A to F are shown in figure 6.4. No real minimum can be determined in these spectra, using finer steps for the chosen test functions introduced statistical fluctuations. The result was interpreted such that the lowest value gives the best description of the experimental data. The error was determined via a linear interpolation between the two lowest points and using the value at χ^2+1. For the high energy part of the 2n channel, the group of events found between 2 and 7 MeV in this channel were analyzed separately. Again a flat, 50 keV wide distribution was used as test function. The results are shown in figure 6.5. All methods show the expected behavior, meaning that the χ^2 distribution around the minimum follows the shape of a parabola. A fit using a polynomial of second order was done to describe the range close to the minimum, indicated as red dashed lines in figure 6.5. Using the parameters of this fit the position of the minimum is used as peak position and the value at χ^2+1 is used as error.

The low energy part of the 1n channel is described together with the low energy part of the 2n as explained before. A second contribution here comes from real 1n events, namely ^{25}O. These two contributions are shown in the lower pad of figure 6.3 as a solid blue line (2n) and a dashed purple line (1n).

To determine the final results of the analysis of the ^{26}O data the probability functions derived while applying method F (see section 5.3) are directly used. The most likely value is used as peak position (E_r). The error is determined using the maximum probability found in the distribution and lowering it such that 68% of the area is underneath the function. The probability distributions for the two found ^{26}O states are shown in figure 6.6. For each state the individual distribution is normalized to one. For the ground state 80% probability is reached within the first bin. For the excited state the 68% range is indicated as a blue dashed area. The found value of E_r=4.225$^{+0.227}_{-0.176}$ MeV is in agreement with the values observed from the parabola fits to the χ^2 distributions.

method	χ^2 at min.	E_r at min. in keV
A	8.0	25 ± 58
B	78.1	25 ± 9
C	46.6	25 ± 24
D	32.8 / (48-1) = 0.7	25 ± 24
E	34.4	25 ± 13
F	0.5	25 ± 16

Table 6.2: Given are the values obtained describing the low-energy part of the ^{26}O 1n and 2n channel using a flat test distribution having a width of 50 keV. NDF is the number of bins in the fit range minus the number of free parameters in the input function. The error is obtained using a linear interpolation between the two lowest points and using the energy at χ^2+1.

method	χ^2 at min.	E_r at min. in MeV
A	5.3	4.21 ± 0.65
B	38.7	4.40 ± 0.08
C	36.8	4.27 ± 0.24
D	22.8 / (60-1) = 0.39	4.27 ± 0.24
E	24.6	4.26 ± 0.23
F	4.0	4.26 ± 0.23

Table 6.3: Given are the values obtained describing the high-energy part of the ^{26}O 2n channel using a flat test distribution having a width of 50 keV. NDF is the number of bins in the fit range minus the number of free parameters in the input function. The χ^2 distributions have been fitted in the range of the minimum using a polynomial of 2nd order. The minimum and error have been determined using the fit.

For ^{26}O the same type of theoretical calculations as for the ^{25}O have been performed, those are indicated in figure 6.6. Here the ground state as well as the first excited state are predicted.
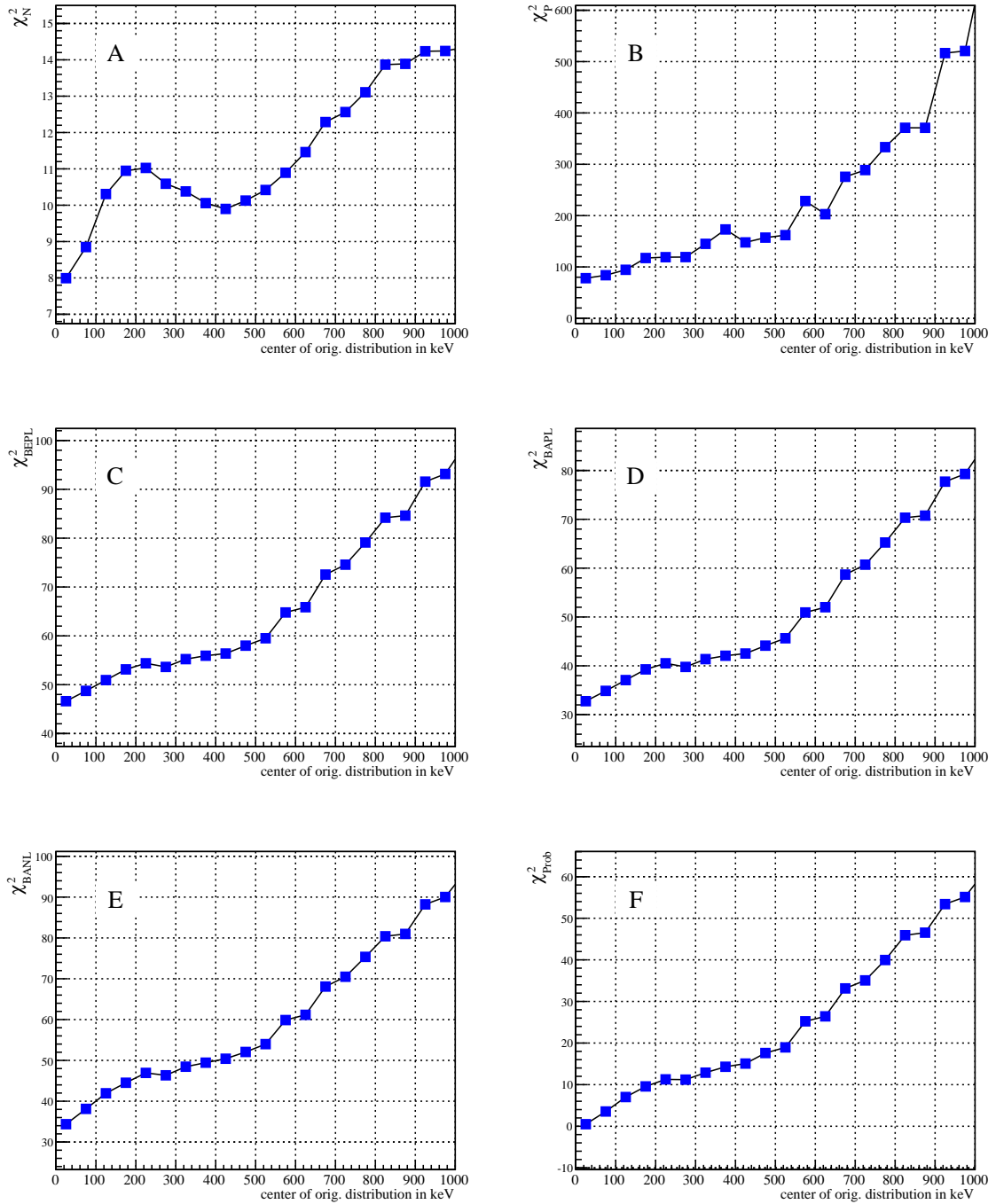
Figure 6.4: Shown is χ^2 for the different methods as a function of the central energy of the test input distribution. Flat distributions with a width of 50 keV are chosen as test functions to describe the low energy part of the ^{26}O 1n and 2n channel. The minimum is for all methods found at the lowest value (25 keV), the extracted results are given in table 6.2.
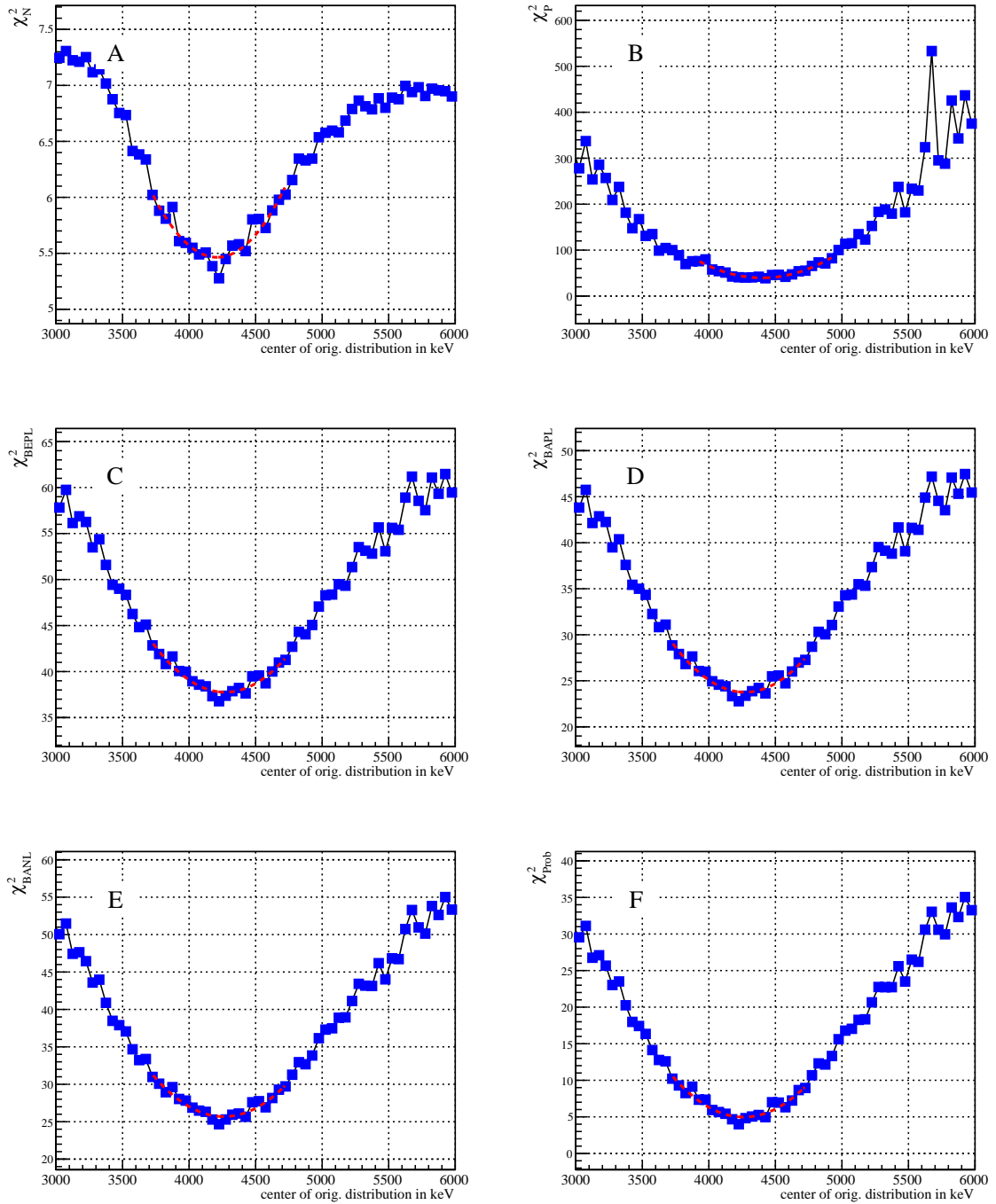
Figure 6.5: Shown is χ^2 for the different methods as a function of the central energy of the test input distribution. Flat distributions with a width of 50 keV are chosen as test functions to describe the ^{26}O 2n channel in a range between 2 and 7 MeV. The extracted results are given in table 6.3 and discussed in the text.
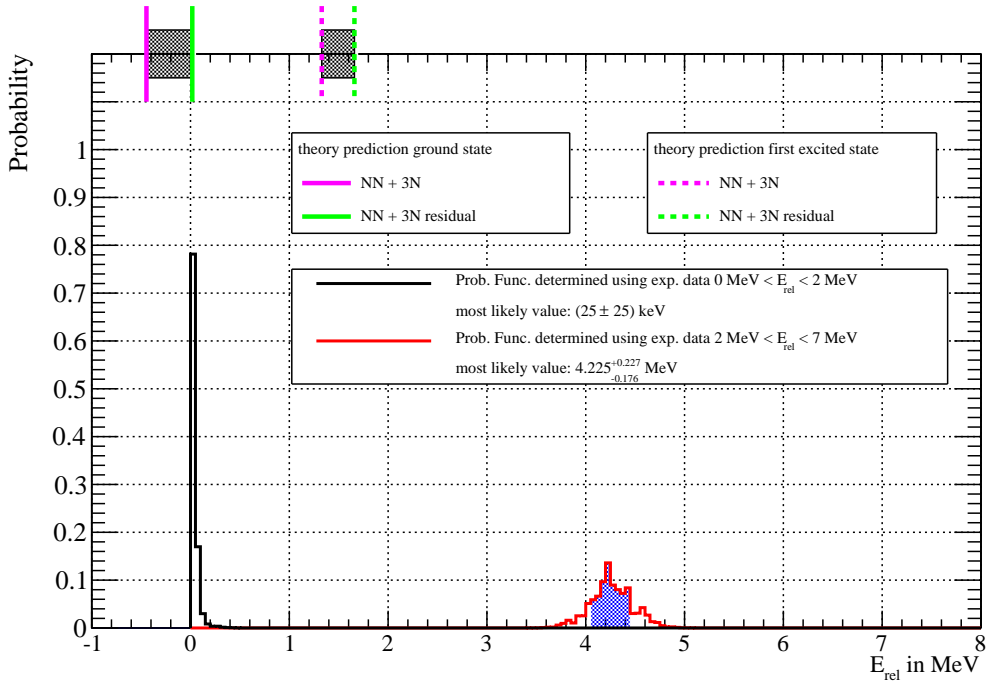
Figure 6.6: Shown is the relative energy of the ^{24}O + 2n system on the x-axis and the probability that the given energy is the real energy of the state on the y-axis. For the ground state almost 80% probability are reached within the first bin (first 50 keV). For a excited state of ^{26}O the probability peaks at 4200 - 4250 keV. The error is determined such that 68% (one σ) of the area have to be under the curve. The theoretical predictions are indicated at the top border of the panel for the ground state as well as the first excited state.

6.3 Lifetime Estimates

For a given angular momentum the decay width can be calculated as a function of the resonance position, if a single particle structure is assumed, e.g. done using formula (5.6). The connection between the lifetime of a decaying nucleus and the width of the state (or resonance) is given by:

$$\Gamma \cdot \tau = \hbar \,, \tag{6.1}$$

where the lifetime (τ) is the time constant in the exponential decay law:

$$N(t) = N_0 \cdot e^{-t/\tau} \,. \tag{6.2}$$

For the ^{25}O ground state a width of $\Gamma = 72^{+126}_{-65}$ keV has been observed. Transforming this into the liftime using formula (6.1) leads to:
$\tau(^{25}\text{O}; \text{GS}) = 9^{+85}_{-6} \cdot 10^{-12}$ ns

For ^{26}O the width of the ground-state resonance could unfortunately not be determined. But using the ToF of the fragment from the target to the center of ALADIN an upper limit on the lifetime can be estimated. Including the relativistic Lorentz factor γ one gets from formula (6.2):

$$\tau = \frac{t/\gamma}{\ln(N_0/N(t))} \,, \tag{6.3}$$

which means that we can obtain the lifetime τ, if the number of surviving nuclei $N(t)$ at time t can be determined. The distance from the target to the middle of ALADIN is given in table 3.1 and amounts to 256 cm. The beam velocity is given on page 47 and is β=0.722. Using these values results in a ToF of 11.8 ns, for the ^{26}O ions from center target to center ALADIN. To estimate the lifetime using formula (6.3) $N(t)$ and N_0 have to be known, in addition to the ToF. N_0 can be obtained from the observed number of events belonging to the ^{26}O ground state and the known efficiency×acceptance. Six events can be attributed to the ^{26}O ground state looking at the 2n channel, see figure 6.3, using the simulation to obtain the efficiency×acceptance a initial number of N_0=20.5 is found. $N(t = \text{ToF})$=1 is used due to the following argument. If the ^{26}O did not decay at the time were it reaches the center of ALADIN two characteristics have to be present for such an event:

(1) It has to be at $A > 24$ in the mass identification plot.
(2) Furthermore no neutron should be observed in LAND, since the decay happens after the ion has been bend off the zero degree line far enough to be outside the acceptance of the neutron detector.

The center of ALADIN has been chosen as 'threshold' exactly for that reason. At this point the beam has been bend by 7.5°, which is the minimum deflection angle to be

outside the acceptance of LAND. The spectrum, shown in figure 4.8, was produced using a CB trigger only, to not reduce the statistic further. If one requires the two above mentioned characteristics, to have no neutron in coincidence and $A > 24$, one possible candidate remains, leading to an upper limit of $N(t)=1$. This one count can either be background or a real ^{26}O event. Here it is assumed to be real to define the upper limit. To determine the error of this one count a Poisson distribution is used. Figure 6.7 shows the probability to measure one count as a function of the given mean for a initial Poisson distribution. The one and two sigma regions are determined such that integral reflects 68.3% and 95.4% probability, respectively. This yields $N(t)=4.87$ for a 95% confidence level.
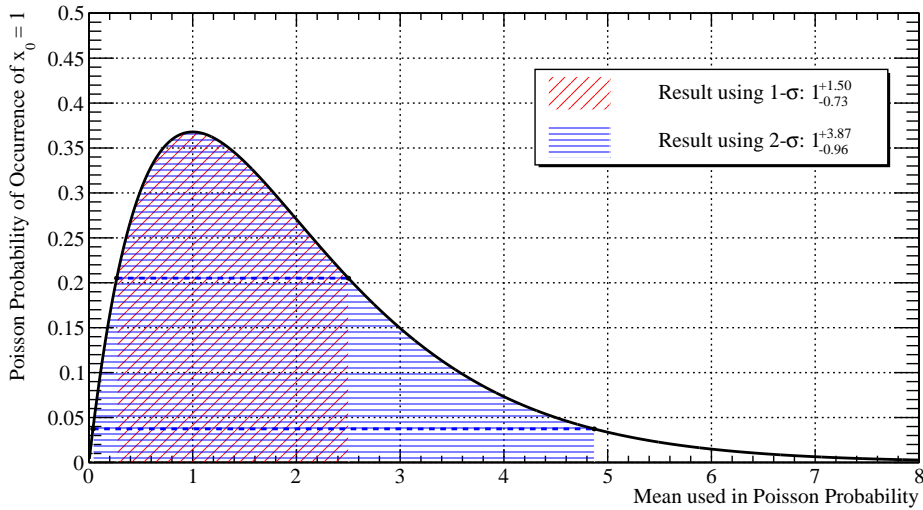
Figure 6.7: Shown is the Poisson probability for the occurrence of $x_0 = 1$ as function of a given mean for a initial Poisson distribution.

Using the values discussed above:

- $t = ToF = 11.8$ ns,
- $\gamma = 1.445$,
- $N(t) = 4.78$,
- $N_0 = 20.5$,

and formula (6.3) results in an upper limit for the lifetime of the ^{26}O ground state, which amounts to:

$\tau(^{26}$O GS$; N(t) = 4.78) \leq 5.7$ ns.

We conclude that the lifetime of the ^{26}O ground state must be smaller than 5.7 ns (95% confidence level).

Chapter 7

Discussion

The results obtained in this work are summarized together with results from the literature in table 7.1 and figure 7.1.

The ground states of ^{26}O and ^{25}O have also been recently observed at NSCL, see table 7.1 , making the new measurement a necessary test of the previous experiments. The obtained results for the ^{25}O ground state is in very good agreement with the previous measurement [HBB$^+$08]. The width (Γ) of the ^{25}O ground state is by approximately a factor of two smaller than observed before, however, is still in agreement within error bars. The single particle width for a $l = 2$ state at $E = 737$ keV is 65 keV, this value is determined using a radius of 4 fm and formula (5.6). The calculated single particle width is in very good agreement with the experimentally measured one. This can be understood as an experimental confirmation for the $l = 2$ single-particle nature of the state.

The found ^{26}O ground state energy and the previous measurement [LDK$^+$12] are also consistent, however, the upper limit is by the new measurement reduced from 200 keV to 50 keV. No excited state of ^{26}O has been observed before, making the observed value the first such measurement.

The theoretical calculations to which the results of this thesis have been compared to have been performed by Holt *et al.* (NN+3N) [Hol12] and Simonis *et al.* (NN+3Nres) [Sim12]. Microscopic 2N and 3N forces from chiral EFT have been used to derive a potential which is then used for shell model calculations. Including three-body forces, due to Δ excitations, one can explain the oxygen anomaly as detailed in chapter 1. Including the 'normal-ordered' 2-body part of 3N forces leads to repulsive interactions between valence neutrons, as shown in figure 7.2. Where 'effective 2-body part' of the interaction means that one neutron from the core interacts with two valence neutrons. Calculations done using this type of interaction are here labeled 'NN+3N'. Contributions from three valence-nucleon interactions are in general suppressed by $\sim N_{valence}/N_{core}$ [FS11], those contributions will therefore only be important in the most neutron-rich nuclei. Making

this effect significant for the oxygen isotopes discussed here. This is why also contributions from interactions amongst three valence neutrons have been recently included in the theoretical predictions, this interaction is called 'NN+3Nres' within this work. The results of the two different theoretical calculations, performed by Holt *et al.* (NN+3N) and by Simonis *et al.* (NN+3Nres), are given in table 7.1. While the calculation using the NN+3N interaction predicts the ^{26}O ground state to be bound a perfect agreement is found using the calculation which includes the residual interactions (NN+3Nres). This interaction predicts correctly that the ^{26}O ground state is unbound. The ground states of both oxygen isotopes are perfectly reproduced by theory using the NN+3Nres interaction. It should be pointed out, that going from the NN+3N to the NN+3Nres interaction both ground state predictions get closer to the experimental observed ones. The theoretical predictions for the first excited state of ^{26}O and the experimentally observed excited state do not match. This discrepancy, however, is most likely found between theory and experiment because the states which are compared here are not of the same nature.

The lifetimes obtained here are discussed in context with values given in [GMSZ11]. Graphs showing the relation between the width and the resonance position for different angular momenta (l) have been adapted from this publication and are shown in figure 7.3. Unfortunately the text of this publication uses the term lifetime (τ) while the axis label indicates that the half-life ($T_{1/2}$). However, the values given within this thesis are all lifetimes (τ).

For the ^{25}O ground state the measurement presented here is indicated in figure 7.3 (a). The blue box represents the measured values including their error. It can clearly be seen that the state has angular momentum $l = 2$ as expected, and also supported by the estimated width using formula (5.6).

state	this work				others					
	experiment		theory		experiment			theory		
	E_r	Γ	Holt *et al.* E_r (NN+3N)	Simonis *et al.* E_r (NN+3Nres)	E_r	Γ	reference	E_r	Γ	reference
^{25}O ground state	737^{+48}_{-43}	72^{+126}_{-65}	545	733	770^{+20}_{-10}	172^{+30}_{-30}	[HBB+08]	1002	-	[VZ06]
								21	2	[VZ06]
^{26}O ground state	25^{+25}_{-25}	-	-446	18	150^{+50}_{-150}	-	[LDK+12]	80	-	[UOMH99]
								500	-	[BR06]
^{26}O exc. state	4225^{+227}_{-176}	-	1328	1659	-	-	-	~ 2100	-	[BR06]
								1870	-	[VZ06]

Table 7.1: Compendium of all results obtained in this work as well as other values found in the literature. All values are given in keV. The theoretical predictions concerning the ^{26}O excited state are all done for the first excited (2^+) state. The state observed in the measurement presented here, is, however, most likely not of the same nature.
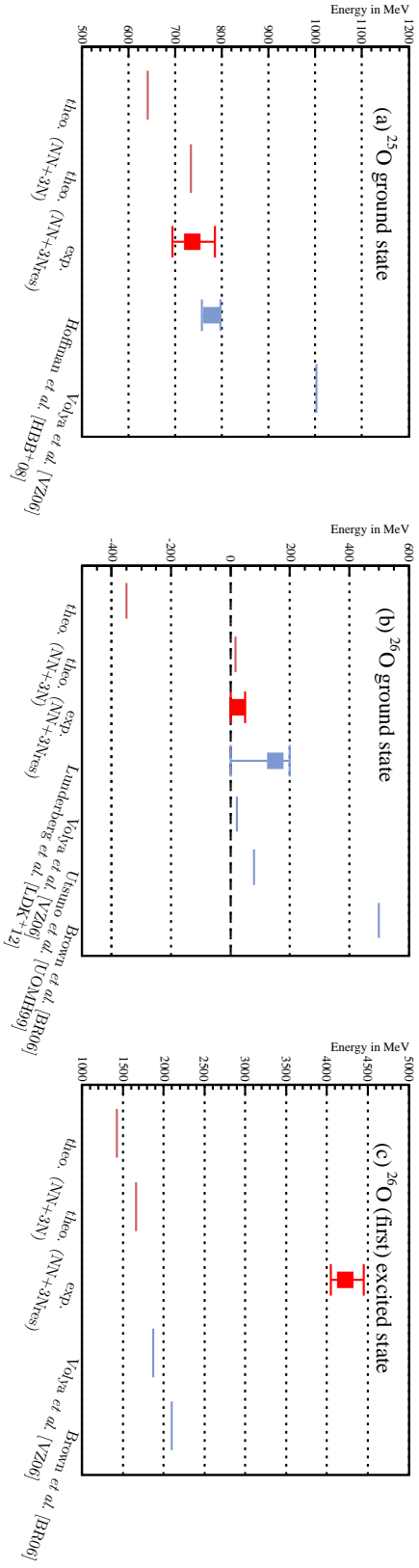
Figure 7.1: Shown are the experimental results obtained in this work and the theoretical values from Simonis *et al.* [Sim12] and Holt *et al.* [Hol12] in red, together with results from the literature in light blue. Theoretical values are shown as lines, while experimentally determined values are depicted as squares with error bars. The error bars represent the experimental error and not the width of the state. All theoretical values depicted in panel (c) represent calculations for the first excited (2^+) state. The nature of the experimentally observed state is most likely different.
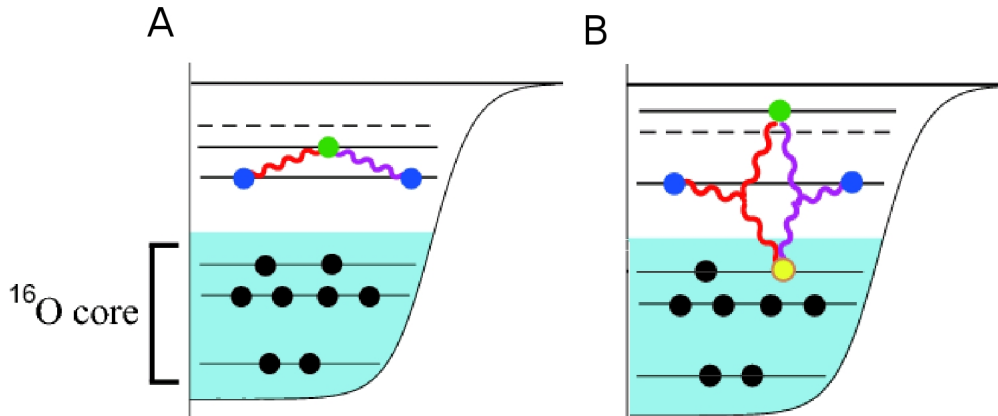
Figure 7.2: Visualization of three-body (3N) forces. The left figure (A) shows 3N inter-actions between valence neutrons. The right figure (B) depicts 3N interactions between two valence neutrons and one neutron from the core. Figure is taken from [Sch12a].

The obtained lifetime of the ^{26}O ground state is indicated in figure 7.3 (b). The values obtained from the measurement are indicated by grey. Those values limit the available range to the area indicated as blue-striped area.

A schematic level scheme depicting the determined energy levels of ^{26}O and ^{25}O relative to the known states of ^{24}O is shown in figure 7.4. Populating the ^{26}O ground state only a direct decay to the ^{24}O ground state is possible, by-passing ^{25}O. Furthermore, the lifetime obtained for the ^{26}O ground state is rather long. This value is twelve orders of magnitude larger than the lifetime found for the ^{25}O ground state. Those two facts make ^{26}O a candidate for a so called true two-neutron decaying nucleus, a property which has been discussed in recent publications [GMSZ11,PKGR12] and which is found for very few nuclei only.
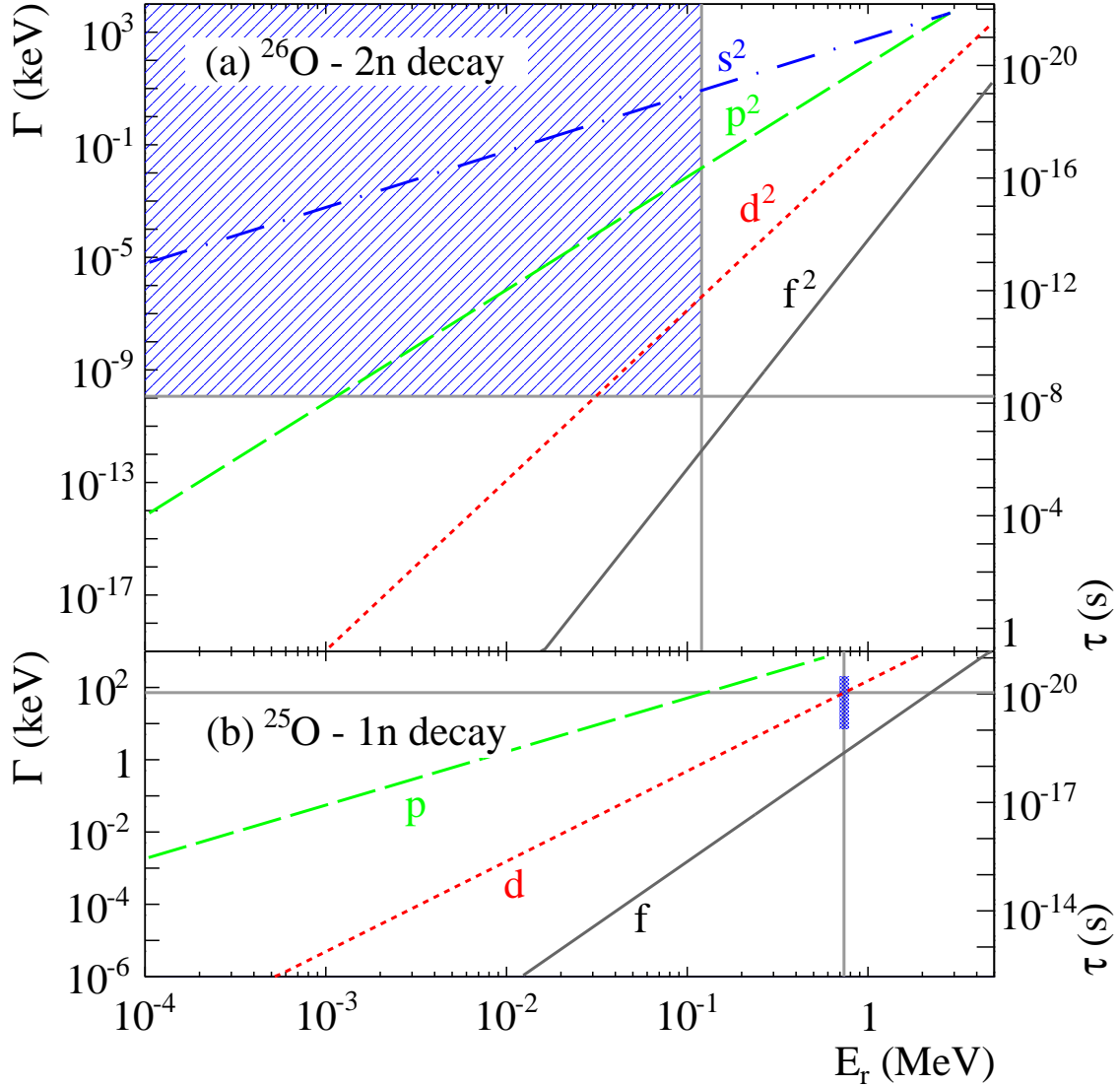
Figure 7.3: Graphs are adapted from [GMSZ11]. The x-axis depicts the position of the resonance, the y-axis on the left gives the width (Γ) while the y-axis on the right shows the corresponding lifetime (τ). The colored lines show the theoretical correlation between width (lifetime) and resonance position assuming different single particle states. The experimental results are shown on top of those theoretical predictions. In the ^{26}O case (pad a) the determined limits (grey lines) define a allowed region, which is shown as a blue hatched area. In the lower pad (b) the result for the width (Γ) and resonance position (E_r) of the ^{25}O ground-state are indicated as grey lines and their errors are represented by the blue area. For further details and discussion see text.
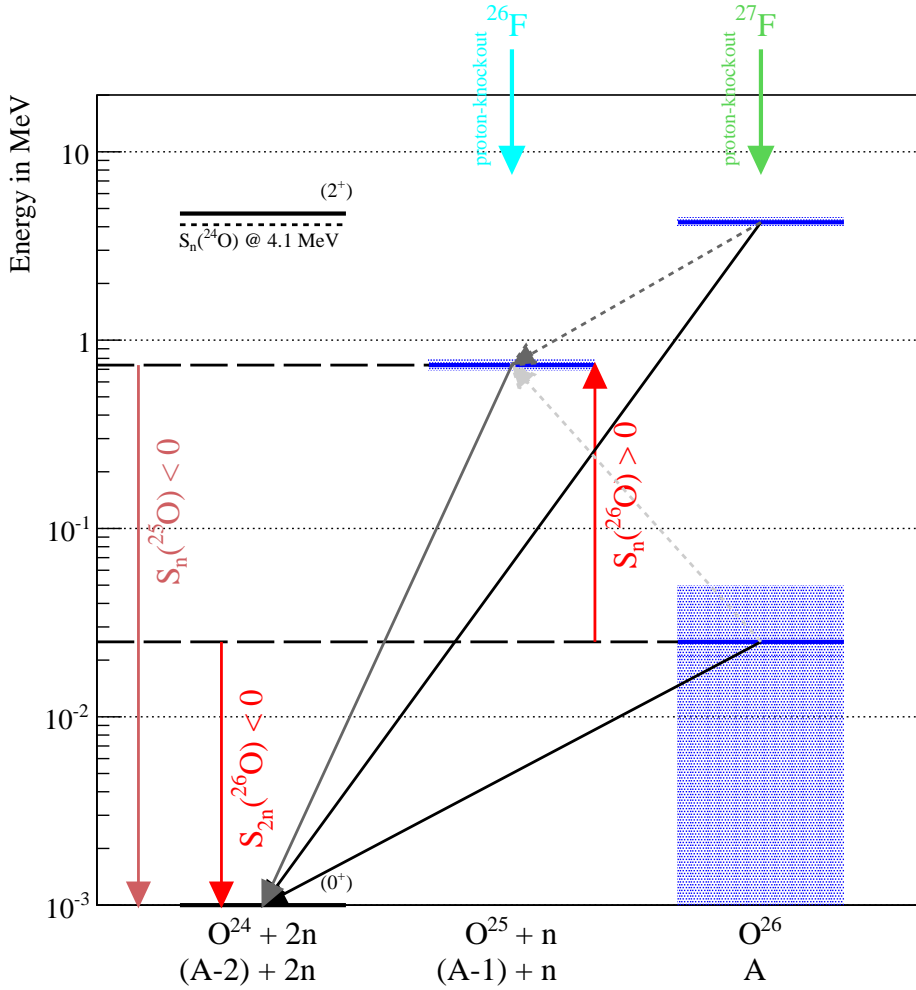
Figure 7.4: Shown is a level scheme of the known states in ^{24}O as solid black lines on the left as well as the new results on ^{26}O and ^{25}O shown as blue solid lines on the right. The experimental errors are represented by the light blue 'bands'. ^{24}O has no bound excited state, the neutron separation energy (S_n) at 4.1 MeV is indicated as horizontal black dotted line as well as the first excited (2^+) state above it at 4.7 MeV, values are taken from [HBB$^+$11]. ^{26}O and ^{25}O have in the experiment presented here been populated via proton-knockout reactions from ^{26}F and ^{27}F, respectively. For ^{25}O exclusively the ground state has been populated which decays directly to the ^{24}O ground state (solid gray arrow). In the ^{26}O case the excited as well as the ground state can be populated. From the ground state only a direct decay to the ^{24}O ground state is possible (black solid arrow). The connection between the ^{26}O ground state and the ^{25}O ground state is indicated by the light-grey arrow showing that this decay is energetically not possible ($S_n > 0$). For the first excited state a direct decay (black solid arrow) as well as a sequential decay (gray dotted and gray solid arrow) via the ^{25}O ground state is possible.

Appendix A

Fit to ^{25}O Data using R=6 fm and $\triangle$

method	χ^2 at min.	E_r at min. in keV	Γ at min. in keV
A	29.42	722^{+107}_{-89}	$344\ ^{+(>156)}_{-336}$
B	108.74	707^{+26}_{-24}	$203\ ^{+205}_{-94}$
C	155.67	742^{+44}_{-45}	$92\ ^{+281}_{-91}$
D	91.67 / (110-2) = 0.85	742^{+44}_{-45}	$92\ ^{+281}_{-91}$
E	95.78	742^{+38}_{-11}	$1\ ^{+25}_{-1}$

Table A.1: Given are the results analyzing the ^{25}O-data using a Breit Wigner line shape and methods A to E. It can be seen that χ^2_N (method A) gives a very low value for the χ^2 at the minimum, this is the case since for empty bins an error of ± 1 was assigned, and this method is the only one using this (large) errors. The reduced χ^2 is only given for method D, this method uses a Poisson distribution for the errors taken from the test function which is the most reasonable assumption. NDF is the number of bins in the fit range minus the number of free parameters in the input function.
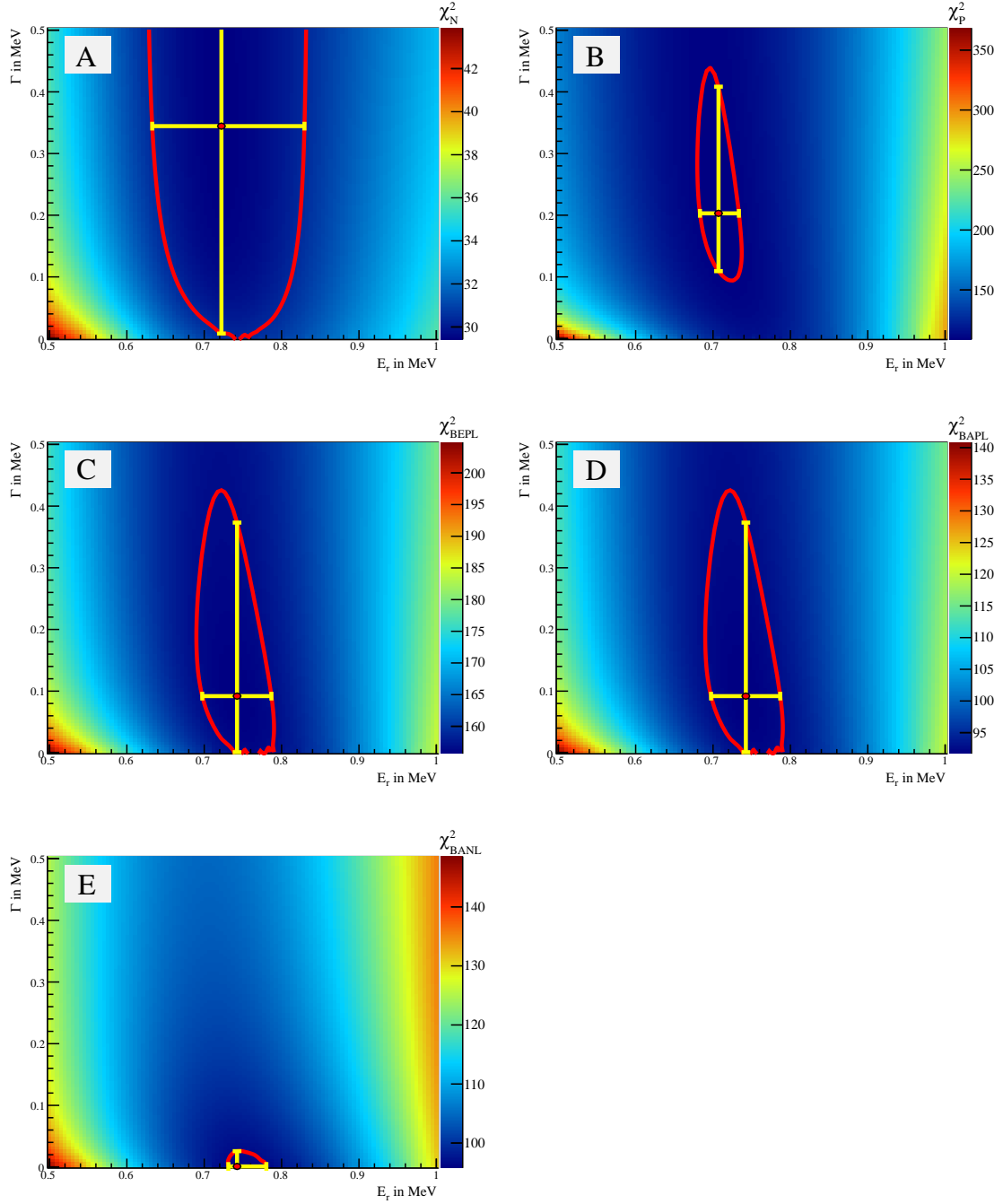
Figure A.1: 2-dimensional χ^2 spectra are shown for methods A to E, applied to the ^{25}O-data using a Breit Wigner line shape as described by formula (5.1). As red solid line the $\chi^2_{min}+1$ contour is indicated in each spectrum, the yellow horizontal and vertical lines represent the errors determined using this contour. The exact values are given in Tab. A.1.

Appendix B

New LAND Electronics - TacQuila

The goal of this document is to introduce the user of NeuLAND to its new readout electronics, namely the TacQuila-readout. The document is a mixture of a description of the individual components and a manual for the usage of the new readout electronics. It is indented that the write-up is also understandable for beginners, that's why a lot of details are given. The here described situation is the one of the TacQuila setup in May 2011. If you have corrections, suggestions, updates or comments to this document please write an email to: `c.caesar@gsi.de`.

B.1 Software / TacQuila-MBS

The DAQ of the TacQuilas is based on MBS, this TacQuila-MBS-DAQ will be introduced in this section. The slow control is currently done using LabView and will be explained in Sec. B.3. The implementation into EPICS is still ongoing.
Two TacQuila DAQ versions are available. One version was modified by H. Johansson to integrate the TacQuilas into the main LAND DAQ. The original sources from the EE[*] are written by N.Kurz. The different sources can be found in:
`/lynx/Lynx/land/usr/land/TacQuila_DAQ`. And the modified version can also be found in the experiment specific folders of the newest experiments, e.g.:
`/u/land/lynx.landexp/aug2010/tacquila/multi_land`.
While starting MBS one should gets messages (among others) which will be similar to the ones shown here:

```
-R3-30  :read_meb   :start TACQUILA initialization
add to sam 6 gtb 0 number 0 tac 1
.
```

---

[*]Experiment Electronic Department

```
add to sam 6 gtb 1 number 29 tac 30
-R3-30  :read_meb   :../util/paraload ./tacset.txt done!
-R3-30  :read_meb   :../util/hstart 6 done!
File ../util/tacquila_big_2010.hex loaded, 98032 bytes, total 98032 bytes
File ../util/tacquila_middle_2010.hex loaded, 59215 bytes, total 157247 bytes
-R3-30  :read_meb   :../util/tacload 6 ../util/tacquila_big_2010.hex
                     ../util/tacquila_middle_2010.hex done!
File ../util/tacsam5.m0 loaded, 2950 words
-R3-30  :read_meb   :../util/hpistart2  6 ../util/tacsam5.m0 done!
-R3-30  :read_meb   :
-R3-30  :read_meb   :wait for GTB TACQUILA address initialization
-R3-30  :read_meb   :this needs a few seconds..
-R3-30  :read_meb   :on SAM5 with id 6, GTB 0: 6 TACQUILAs found
-R3-30  :read_meb   :
-R3-30  :read_meb   :finished TACQUILA initialization
-R3-30  :collector  :acquisition running
```

This means, the following three files have been loaded:

- tacset.txt (contains some of the TacQuila settings),
- tacquila_big_2010.hex (code for first TacQuila FPGA),
- tacquila_middle_2010.hex (code for second FPGA on the TacQuila).

And 6 TacQuilas have been initialized by MBS. This number should of course match the current setup.

Some settings of the TacQuilas can be done in the above mentioned `tacset.txt`, which can be found in the MBS directory. This file is only loaded during the startup of the DAQ, so one has to do a 'stop acquisition' and 'start acquisition' to activate changes. The following can be changed using this file:

1)SAM_id	→ parameter which will be written to the data to identify the SAM.
2)GTB_id	→ is 0 or 1 and identifies the 2 GTB cables of the above mentioned SAM.
3)TacQuila_id	→ on each GTB one can have up to 10 TacQuilas here one can define the numbering of those.
4)reset on=1/off=0	→ enable or disable the reset-time.
5)threshold	→ NOT used anymore, was threshold setting of comparator on FEE (value 0-3F) in the 'pre-TRIPLEX-phase'.
6)reset time	→ (value 0-3F) specifies how long an event is kept. If the event is not read out within the reset time it is discarded.

Remark:
The 'tacset-HEX-value' (0-3F) is converted into a 6 bit binary value. This value is then extended by two bits. The two added least significant bits are fixed to '11'. Hence, the real value in decimal goes from 3 to 255 in steps of four. Therefore one can use the following formula to get the reset-time in ns:
reset-time (ns) = (tacset-HEX-value · 4 + 3) · clock-cycle
As a consequence the reset time can be set within the following window (using a 40 MHz clock):
75 ns ≤ reset-time ≤ 6375 ns; in 100 ns steps.

7)generator on=0/off=1 → On the FOPI FEE there is a pulser which can be turned on with this parameter. For the LAND FEE this is of no use at all.

8)TacQuila in=0/out=1 → TacQuila board will not be read out also it is connected to the GTB if the setting is 1.

The parameter of most importance here is the reset time. During tests this was mainly set to the maximum, however, during a real experiment it should of course be set to the shortest value reasonable to minimize the dead-time of the system.

In the LAND DAQ the TacQuila events are 'marked' with the following numbers: type=94, subtype=9400[*]. So one can do a type event in the DAQ screen (e.g.: `X86G-10:: ty ev -v`) and look for the '94 /9400' events to see if the TacQuilas deliver data.

For an event measured with TacQuila readout electronics the result of three individual measurements is written to the data file:

1. TAC-value,
2. clock-cycle-counter,
3. QDC-value.

On the MBS side the data format of the TacQuilas looks like shown in table B.1. Unpacking lmd files with `land02` one gets the parameters shown in table B.2 and B.3. The structure shown here is from an example of the DTF[†] x paddles, the unpacking was done using the option, `--paw-ntuple=RTS,RAW,SYNC,DTF`, so one has DTF data in `RAW` and `SYNC` level.

To have times in ns from the data delivered by a TacQuila-system one should use `land02` `SYNC` level data. For `RAW` level data the time information is split into the fine and coarse measure. R. Plag integrated the calibration routine explained in Sec. B.4 into the `tcal` program[‡]. The `tcal` routine is one of the standard programs of the `land02` package. For more information on the `land02` package see: `www-linux.gsi.de/~rplag/land02`.

---

[*]These values are not TacQuila-hard-coded, they are e.g. defined in:
`/u/land/lynx.landexp/aug2010/tacquila/multi_land/setup.usf.in`
For the s394 (AsyEOS) experiment e.g. 1/10 was chosen.

[†]D̲icke (engl. thick) T̲ime of F̲light wall

[‡]Since the time calibrations of the TacQuilas is done in a different way than for all other systems in the LAND setup the program looses it's generic features here. If problems occur please contact R. Plag.

For each GTB on each SAM a 32 bit header word (were the bits mean the following):
`31-28`: SAM id
`27-24`: GTB id
`23-20`: local event counter
`19-16`: trigger type as seen by SAM (1 physics, 2 calibration)
`15-12`: trigger type as seen by TacQuila (0 physics, 1 calibration)
`8-0  ` : data length on this SAM/GTB in 32 bit words, excluding this header word

For each fired TacQuila channel two('time' and 'charge') 32 bit words:
first word (time):
`31-27`: TacQuila (GTB) address
`26-22`: channel number on TacQuila card (0-16)
`21   ` : 0 indicating first TacQuila channel data word
`20   ` : 0 physics, 1 calibration trigger
`19-12`: clock-cycle-counter
`11-0 ` : hit time (TAC)

second word (charge):
`31-27`: TacQuila (GTB) address
`26-22`: channel number on TacQuila card (0-16)
`21   ` : 1 indicating second TacQuila channel data word
`20   ` : 0 physics, 1 calibration trigger
`11-0 ` : QDC data

Table B.1: TacQuila data structure in MBS.

`Rdtxmul`	→ how many paddles fired
`Rdtxmuli[6]`	→ which paddle fired
`Rdtxt01[6]`	→ TAC-measurement PMT1
`Rdtxt02[6]`	→ TAC-measurement PMT2
`Rdtxt03[6]`	→ counter-measurement PMT1
`Rdtxt04[6]`	→ counter-measurement PMT2
`Rdtxt05[6]`	→ 17th channel TAC-measurement
`Rdtxt06[6]`	→ 17th channel TAC-measurement
`Rdtxe01[6]`	→ QDC-value PMT1
`Rdtxe02[6]`	→ QDC-value PMT2

Table B.2: Shown is the structure of TacQuila-data in `land02` `RAW` level.

Using `tcal` it is possible to create `SYNC` level data within the `land02` analysis framework. Besides `land02` also a UCESB* version for the TacQuilas is available, see e.g. `/u/land/unpackexps/tacquila17` or `/u/land/unpackexps/s393`. This is e.g. usefull to setup an unpacker or watcher for a small test-setup.

---

*Unpack and Check Every Single Bit

```
Sdtxmul     → same as in RAW level
Sdtxi[6]    → same as in RAW level
Sdtxt01[6]  → reconstructed time of PMT1 in ns
Sdtxt02[6]  → reconstructed time of PMT2 in ns
Sdtxt03[6]  → counter of PMT1 in ns
Sdtxt04[6]  → counter of PMT2 in ns
Sdtxt05[6]  → 17ᵗʰ - TAC in ns
Sdtxt06[6]  → 17ᵗʰ - TAC in ns
Sdtxe01[6]  → QDC-PMT1; randomized over bin-width
Sdtxe02[6]  → QDC-PMT2; randomized over bin-width
Sdtxe03[6]  → empty
Sdtxe04[6]  → empty
Sdtxe05[6]  → empty
Sdtxe06[6]  → empty
```

Table B.3: Shown is the structure of TacQuila-data in land02 `SYNC` level.

B.2 LAND FEE

The LAND FEE, is an adaption of the FOPI FEE [CSC⁺07]. Due to its shape it is also called 'Hammer Hai' (engl. hammerhead shark), see figure B.1.

In figure B.3 it is schematically shown how a signal is processed on the LAND FEE. Here a 'ideal' case is shown in which the protective diode does not cut (this happens at ≈ 700 mV) the signal and the amplifier is not in saturation (happens at ≈ 200 mV). In the following the signal flow will be discussed in detail for one channel. The first component on the board is a protective diode (HBAT 5402) which in the original design was forseen to protect the amplifier from sparks. In the next device (Monolithic Amplifier GALI-S66+) the signal is inverted and amplified. The output of the amplifier is then split to do a time and an energy measurement.

On the time branch the signal is routed to a comparator (MAX9601). The voltage of this comparator is kept stable using a linear regulator (LP3965EMP-ADJ). The comparator compares the input signal to a threshold. If the input is larger than the threshold a PECL output signal is generated which is routed to the TacQuila[17] and the TRIPLEX board.

On the energy branch the signal is given to a buffer-amplifier (MAX2471) which is here used to convert the input to two single-ended outputs. Normally this device expects a differential input, however, in this application the second input is connected to ground. From these two outputs the negative is send to the TRIPLEX, while the positive is routed to the piggyback-QDC.

The gain of the amplifier is nominal $\sqrt[3]{160} \approx 5.4$ (The FOPI FEE had three stages using this amplifier and a total gain of 160). Measuring the signal using a probe infront and
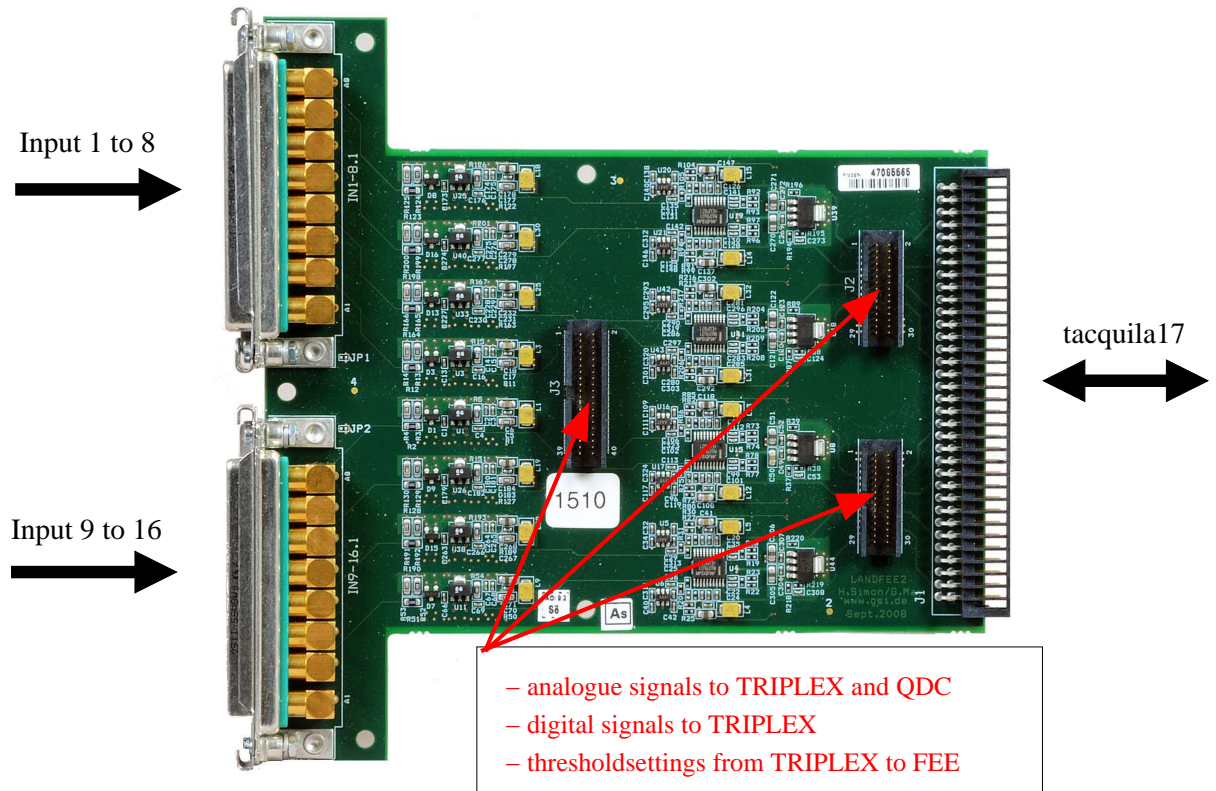
Figure B.1: The LAND FEE is shown. On the left side the input signals, coming e.g. from a detector have to be connected. The TRIPLEX board goes on top on the three connectors while the TacQuila board is connected using the connector on the right side. On these connectors the FEE is also supplied with lv.

input amplitude / mV	output amplitude / mV
7	20
15	40
37	90
75	140
100	160
200	180
>200	180 / 190

Table B.4: Correlation between amplitude of input and output signals of the amplifier.

behind the amplifier gave different results, see table B.4. The amplifier is designed such that it delivers a very fast rise time to achieve the optimal time resolution but this results on the other hand in a small linear range, see table B.4 and figure B.4, this means the amplifier goes very fast into saturation. How the currently used amplifier for example affects the shape of a too large input signal is visualized in figure B.4.
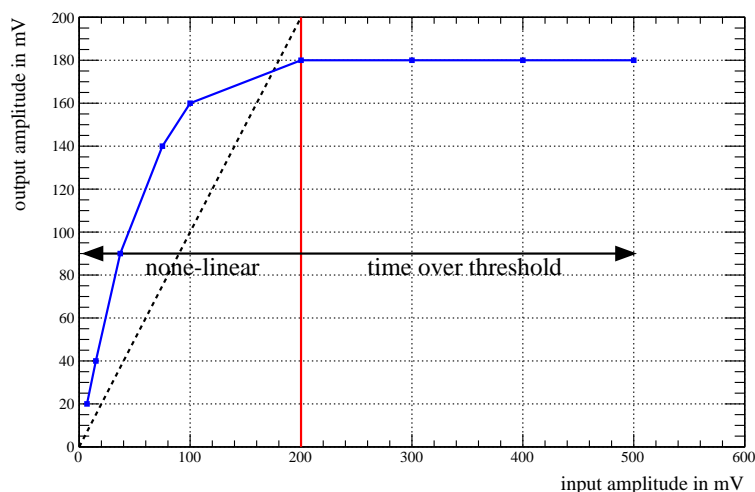
Figure B.2: A graphical representation of the values given in table B.4 is shown. The values are represented by the blue markers and line. The black, dashed line represents the diagonal. The red vertical line represents the limit between the two working regimes of the amplifier.

The following versions of the LAND FEE do exist at the moment:

- FEE1 (LEMO-version),
- FEE1A (SAMTEC -version),
- FEE2 (HammerHai).

which do only differ by the used connector types. Since the TacQuila readout was designed to be used with RPC detectors, but is now used in combination with a plastic scintillator which is coupled to a PMT, the FEE needs some modifications to work optimal for these (larger) signals. While in conjunction with the RPC the TacQuila has to work with very small input signals, deliver a very fast timing and the energy measurement is of minor interest, for the use together with a scintillator based detector the input signals are much larger, the time measurement is not as critical and the energy measurement is also important. To cope with these requirements the following modifications are planned for the FEE3. The protective diode will be removed and the amplifier will be replaced by an component which does only an inversion, such like e.g. the general purpose pulse transformer murata 78601. This development is currently ongoing.

If one connects detector signals to the LAND FEE one has to be careful since the numbering of the used eight-fold connectors and the channel numbering on the board is not mapped in a 'one to one way', see figure B.5.

99
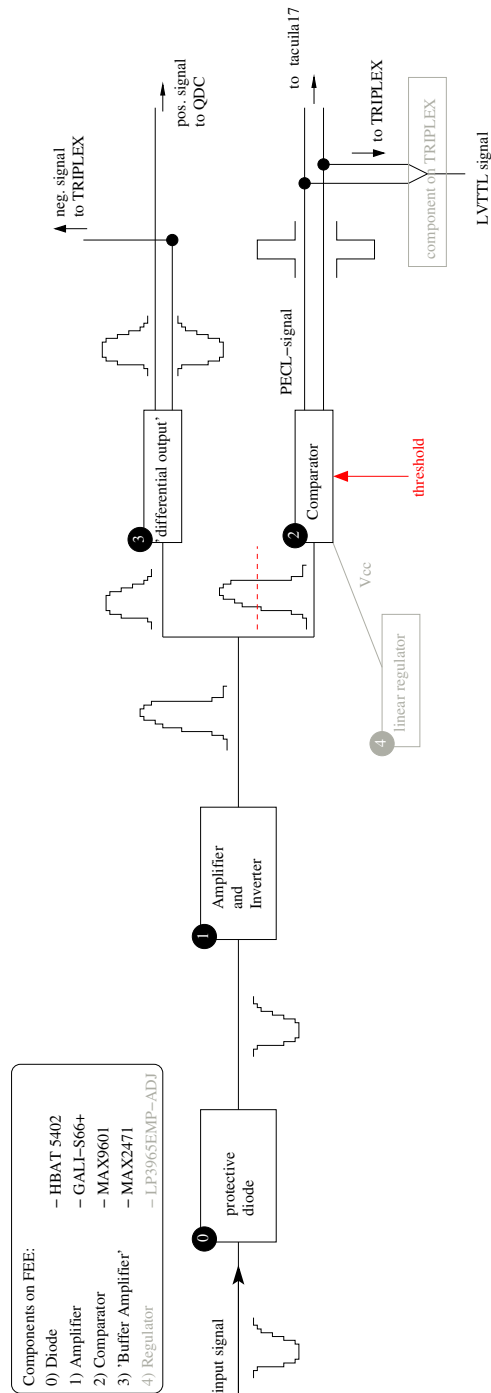
Figure B.3: It is schematically shown how a signal is processed on the LAND FEE, for details see text.
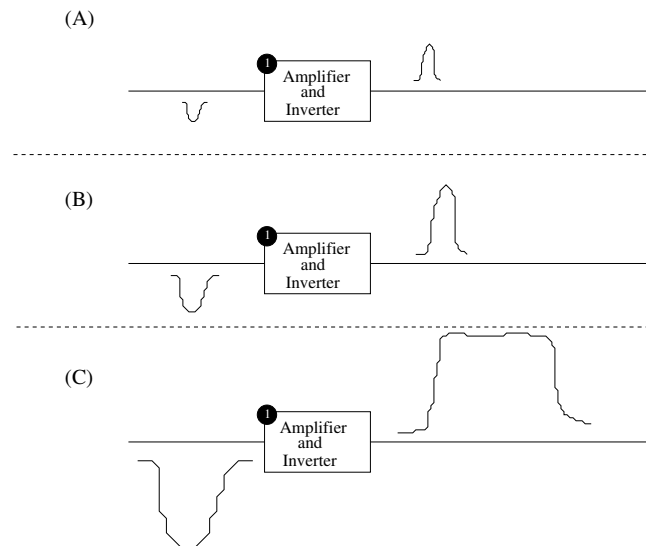
Figure B.4: Three different input pulses and the response of the amplifier to these are schematically shown. This schematic visualizes that the amplifier goes into saturation if the input is too large and how it affects the shape of the pulse.
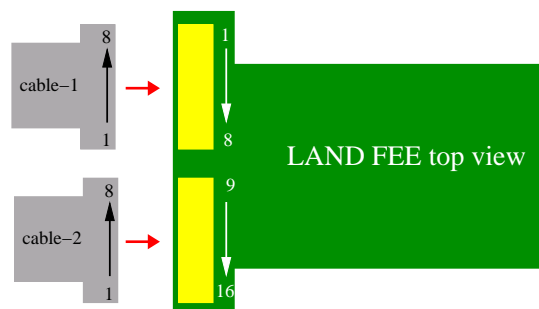
Figure B.5: Shown is a schematic view of the LANDFEE. The connectors are indicated. It is illustrated how the mapping of the detector signals to the electronic channels has to be done. If one uses for example the eight-fold cables of LAND pin 1 on cable 1 would be TacQuila channel 8.

B.3 TRIPLEX

The initial name of the TRIPLEX board during the development stage was 'FEE piggyback' board, the board is shown in figure B.6. The nowadays used name could be interpreted as TRIgger and multiPLEXer board. The TRIPLEX offers the following features:

- individual threshold for each of the 16 channels on the FEE.
- Mul signal of the full TRIPLEX tree.
- analogue sum of the full TRIPLEX tree.
- Or signal of the full TRIPLEX tree.
- A pulser to fire the timing branch of an individual, several or all channels in the TRIPLEX tree.
- A multiplexer to look at an individual signal, as well as e.g. at Mul signals of parts of the TRIPLEX tree.

The TRIPLEX cards are connected in a tree like structure via I^{2}C*, see e.g. figure B.7. The most top module in the tree is connected to the so called TRIPLEX-interface, which is a modified TRIPLEX board in a housing which holds several additional in- and outputs, see figure B.8. The cable used to connect the first TRIPLEX card to the TRIPLEX-interface should be as short as possible. Using e.g. a 2 m long cable caused severe problems in the test phase[†]. The in- and outputs of the TRIPLEX-interface-prototype shown in figure B.8 are:

- Pulser input, the here connected pulser can be distributed either to all TacQuila channels in the tree or to individual ones. The mode is selected via the LabView settings. There is no QDC measurement for these events, only the comparator will be fired by changing the threshold from its nominal voltage to +5V or -5V. Doing this the threshold crosses the baseline and the comparator gets triggered. The pulser input has to be a LVTTL[‡] signal. Furthermore, it has to be terminated using a lemo[§]-T and an additional 50 Ω resistor. Otherwise one can get problems with a floating baseline.
- Mul output, signal which represents how many channels fired in the whole tree. The width can be individually changed for each channel changing the setting of the corresponding stretcher. The height can be changed for each card via a potentiometer. In figure B.9 an example, how a Mul signal looks like, is shown, in

---

*Inter-Integrated Circuit; is a multi-master serial single-ended computer bus

[†]I^{2}C communication did not work reliable.

[‡]Low Voltage Transistor-Transistor Logic

[§]Lemo is the name of a company producing mainly push-pull connectors, in the context of this document the name lemo is used as a synonym for the in nuclear physics experiment commonly used 1-pin connectors of type #FFA 00.250.CTAC29

this example five TRIPLEX cards have been connected in one tree. Each of them had a different width for its Mul signal. The height of the Mul signal was adjusted such that it was 40 mV / fired-channel, so the picture, shown here, represents one channel firing on each of the five cards.

- AMux and DMux are the multiplexer outputs. The AMux is used to look at an individual signal after the amplifier. While the DMux delivers analogue sum, OR and Mul signals of the tree, but only up to a certain card, which can be selected via slow control settings.

- The analogue sum signal of the full tree.

- The OR signal of the full tree.

- The two lemo connectors without any label are used to program which of the connectors (J5 or J7) is used as the start for the TRIPLEX tree. This is done by sending a logical signal to these inputs. These inputs should be terminated. The default setting is that J5 is used.

- The I^2C bus is used to communicate in both ways (get data, write settings) to the TRIPLEX.
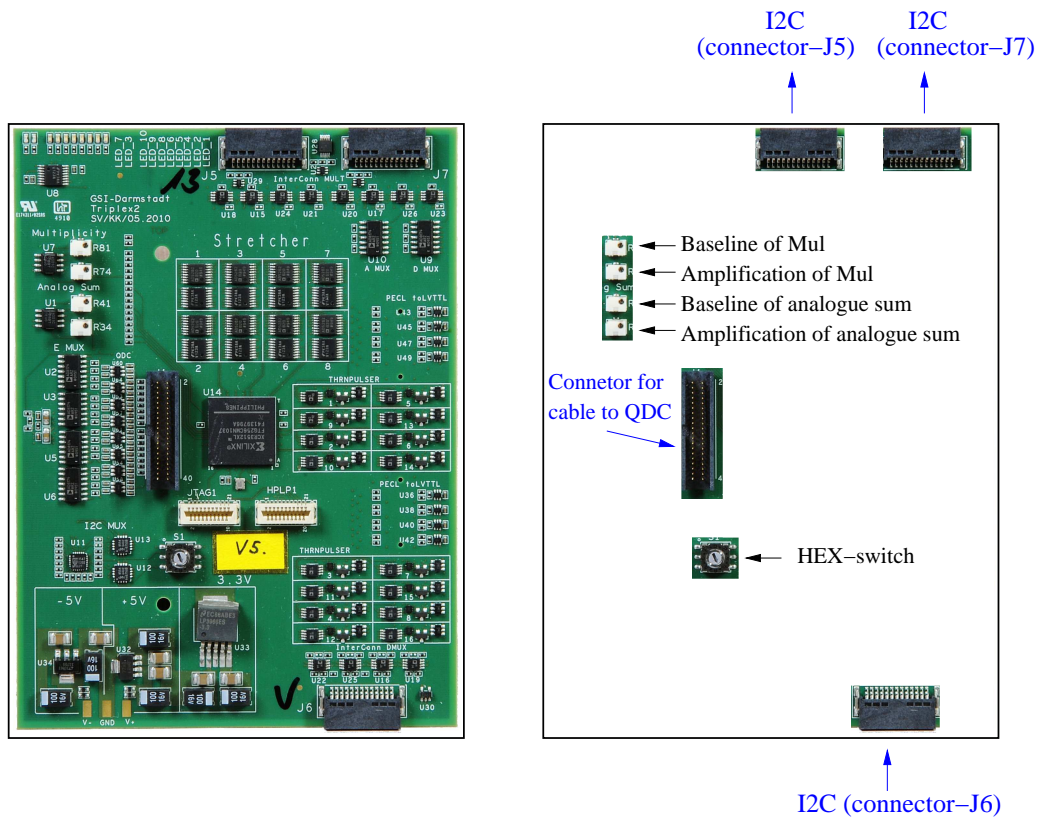
Figure B.6: On the left side the full TRIPLEX board is shown. On the right side some components are highlighted to show the possible connections and where on the TRIPLEX card one can set the following:

- Baseline of Mul signal.
- Amplification for Mul signal.
- Baseline of analogue sum.
- Amplification for analogue sum.
- I^{2}C address.
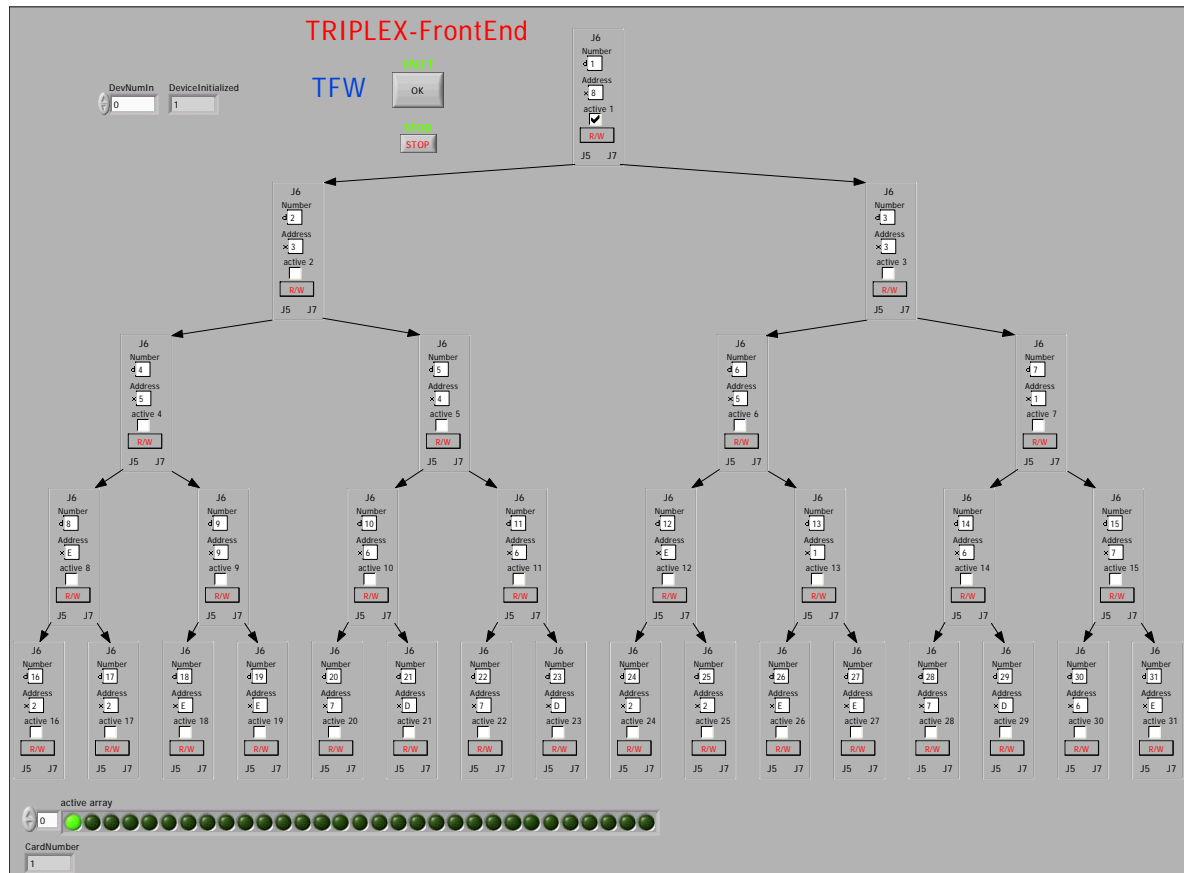
Figure B.7: Screen-shot of the LabView Main-panel to control the TRIPLEX. Visualizes also the tree like order of the TRIPLEX cards.
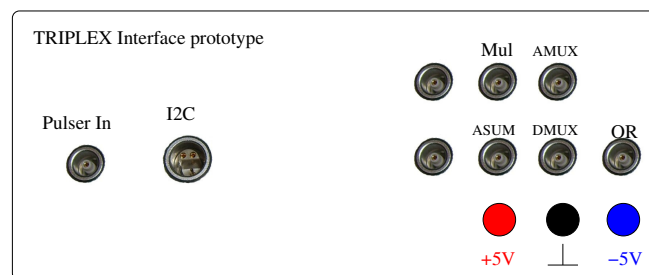
Figure B.8: Shown is the front Panel of the TRIPLEX interface prototype, the different connectors are indicated. In addition to the here shown connectors on the front a connector for the I^2C to the first TRIPLEX in the tree can be found on one side, normally the connector J5 is used for this purpose. For more details see text.
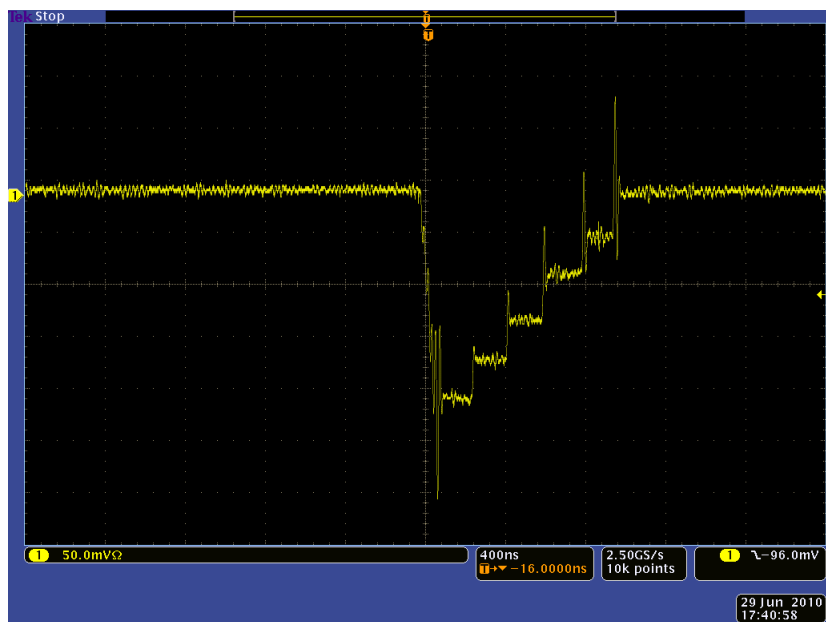
Figure B.9: A screen-shot from the scope of the TRIPLEX-Mul signal is shown. The sparks visible here have been removed for the currently used TRIPLEX boards by adding capacitors. For details on other aspects of the signal shape see text.
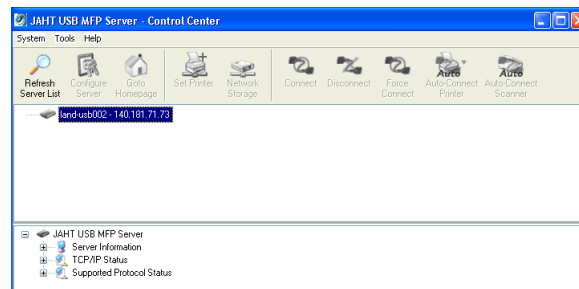
Figure B.10: Shown is the menu of the MFP server. At the moment there are 3 USB-over-IP-server used for TacQuilas at GSI. The one called EE should not be touched. The ones called land-usb001 and land-usb002 are used to control the two TRIPLEX chains which are currently in use (LAND and Veto, see Sec. B.3).
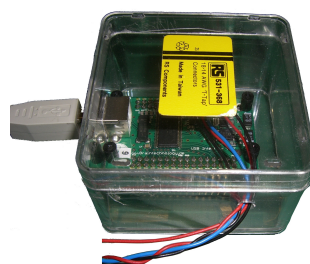
Figure B.11: Shown is a prototype of the I^{2}C-to-USB-converter.

Figure B.12: Shown is the used USB-over-IP-server.
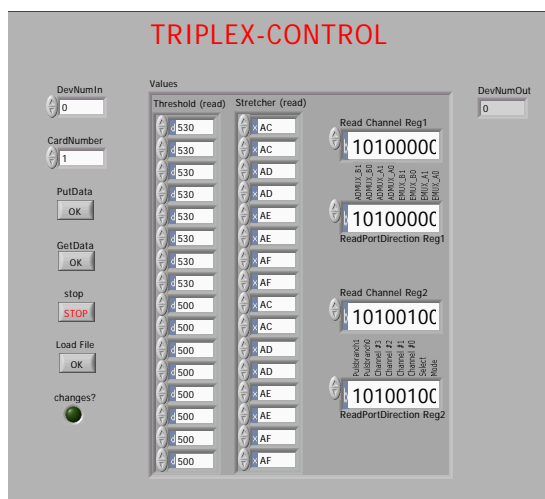
Figure B.13: Shown is the TRIPLEX control window of one card. For explanations see text.

Besides the TRIPLEX interface two more modules are needed to control the TRIPLEX over the network, the I^{2}C-to-USB-converter and a USB-over-IP-server, see figure B.11 and figure B.12. The USB-over-IP-server can be remotely reset using a network controllable power plug. This can be accessed via a web-interface, `www.landpwr002.de`, usr-name and password are the standard land ones.

The TRIPLEX cards are at the moment controlled via LabView. In the next paragraph some details on the LabView settings as well as detailed instructions on how to read and write those will be given. LabView is e.g. installed on KRAPC003, a windows machine currently located in Cave C. The user can either use this machine locally or connects to it using a Remote-Desktop-Connection. To be able to communicate with the TRIPLEX one has first to connect the USB-over-IP-server to that computer, this is done using a program called MFP-server. The GUI of this program is shown in figure B.10. One has to select a certain USB-over-IP-server and connect it by using the corresponding button. Now one can control the settings of the TRIPLEX cards via LabView. Opening LabView one gets two windows (shown in figure B.7 and B.13). The TRIPLEX control window should be closed. The second one (figure B.7) is the main TRIPLEX control window. Here one sees a scheme of the TRIPLEX chain. To start the TRIPLEX-control one has to push the arrow in the left upper corner which makes the program 'run'. The next step is to initialize the control using the INIT button in the middle of the LabView window. For each card a window will open and close again showing that this card is being initialized. If the settings, e.g. threshold values, look strange (meaning e.g. 123456) this means most likely that the communication between the TRIPLEX tree and LabView does not work. One problem could be the 'device number', see figure B.7 field labeled DevNumIn at the left upper corner. Having two TRIPLEX trees (LAND and VETO) the correct address has to be chosen here. This address is assigned each time the devices are started, therefore it is unfortunately not fixed and has to be checked each time.

To change the settings of a certain card one has to click the R/W (Read/Write) button of that card. As a result a window like shown in figure B.13 will be opened. Here one sees:

- 'CardNumber' - this number identifies the card. The Address which is shown in the main TRIPLEX control window can be used by several cards as long as they are on different branches of the tree. The Addressing of the cards will be discussed in detail later, see Sec. B.3.1.
- 'PutData' - pushing this button will write the shown values to the TRIPLEX card.
- 'GetData' - pushing this button will read the current settings from the TRIPLEX card.
- 'stop' - will close the window (if one uses the 'X' to close the window, like most users might intuitively do, the LabView GUI will freeze).

- 'LoadFile' - one can load (old) settings from a file.

In the 'values box' on the right side of the TRIPLEX control window one can set the following:

- threshold and stretcher values for each of the 16 channels of this TacQuila. The stretcher value sets the width of the logical signal used for the Mul (see also figure B.9). While the threshold is used for the comparator. The threshold is applied after inversion and amplification of the signal at the comparator, see figure B.3. To be able to estimate a reasonable threshold setting see table B.5.

- 'Read Channel Reg-i' (i=1,2) expects a eight digits binary value[*]. 'Read Channel Reg1' is used for the Multiplexer. Here one can put one of the $x \cdot 16$ used channels to the Mux output of the TRIPLEX interface. With x being the number of TRIPLEX cards in the tree. This was never used by me. For details ask K. Koch or A. Ignatov. The 'Read Channel Reg2' is used to control the pulser. The meaning of each of the 8 bits will be described now. The bits are numbered from the left to the right (1|2|3|4|5|6|7|8).

  1,2   = Pulse Branch, here it is chosen to which branch the pulser is send:
       - both (J5 and J7); bits: 00
       - none; bits: 11
       - only left (J5); bits: 01
       - only right (J7); bits: 10

  3,4,5,6 = Channel (here one can select a specific channel if bit 7 is set to 1)
  7   = Select (0 = fire all channels; 1 = fire single channel)
  8   = Mode (0: thr. $\rightarrow$ +5V; 1: thr. $\rightarrow$ -5V)

  Examples for pulser settings are:
  00000001 (looks in LabView like 1) = pulser fires each channel in the tree.
  00000011 (looks in LabView like 11) = pulser fires only channel-1 on each card in the tree.

- 'ReadPortDirection Reg_i' (i=1,2) expects a 1 digit binary value. Defines if the values should be written (==0) to or read from (==1) the CPLD[†] of the TRIPLEX. In principle the setting should here always be 0.

  Remark to LabView:

  Each box in LabView indicates what type of value it expects; d=decimal, x=hex, b=binary.

---

[*]Here one has to be careful. LabView cuts the leading zeros and does also not align to the right. So a shown 1 means for example in reality 00000001.
[†]<u>C</u>omplex <u>P</u>rogrammable <u>L</u>ogic <u>D</u>evice
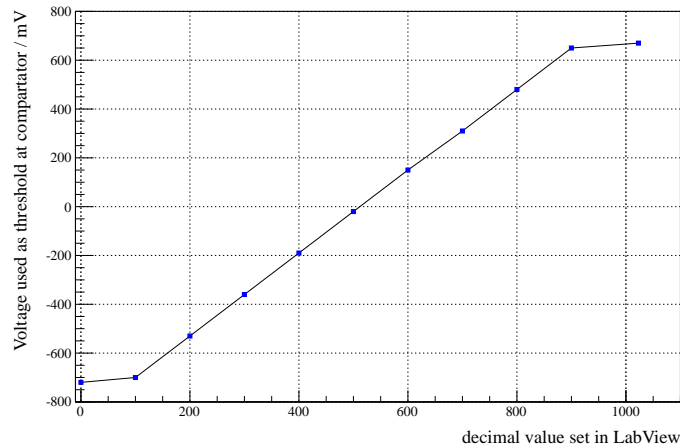
Figure B.14: Shown is a graphical representation of table B.5.
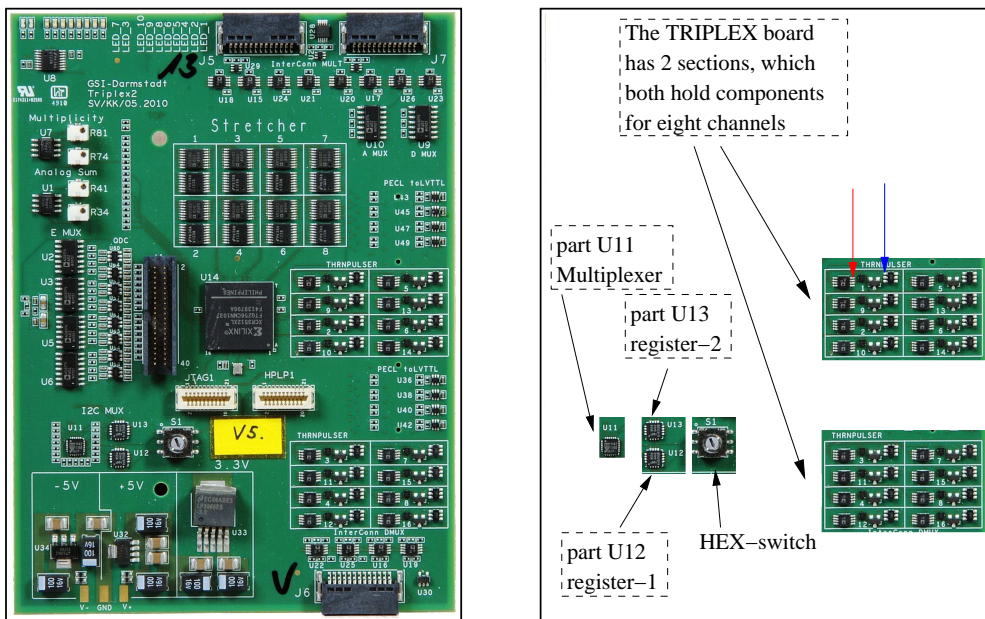
Figure B.15: On the left side the full TRIPLEX board is shown. On the right side it is indicated where on the board one can measure the thresholds. For each of the 16 channels there is one field with 4 components. On the right upper leg of the left component (red arrow), one can measure the threshold before the DAC. While on the left upper leg of the right part (blue arrow) the voltage how it is given to the FEE can be measured. Furthermore, the HEX-switch, the Multiplexer (Part-U11) and the two registers (Part-U12 and Part-U13) are shown. For details see text.

Digital Value	Comparator Value in V	TRIPLEX Value in V
0	-0.72	-4.12
100	-0.7	-4
200	-0.53	-3.04
300	-0.36	-2.07
400	-0.19	-1.1
500	-0.02	-0.13
600	0.15	0.83
700	0.31	1.8
800	0.48	2.75
900	0.65	3.72
1023	0.67	3.83

Table B.5: The left column shows the threshold settings entered via the LabView-TRIPLEX-Control, see figure B.13. This is the value which is then used by the DAC on the TRIPLEX board to generate the threshold as seen by the comparator on the LAND FEE. The middle column shows the voltage which defines the threshold for the comparator. While the right column shows the voltage how they are measured on the TRIPLEX card. These values are helpful because they can be measured on the board while everything is mounted and running. See figure B.14 for a graphical representation of the table.
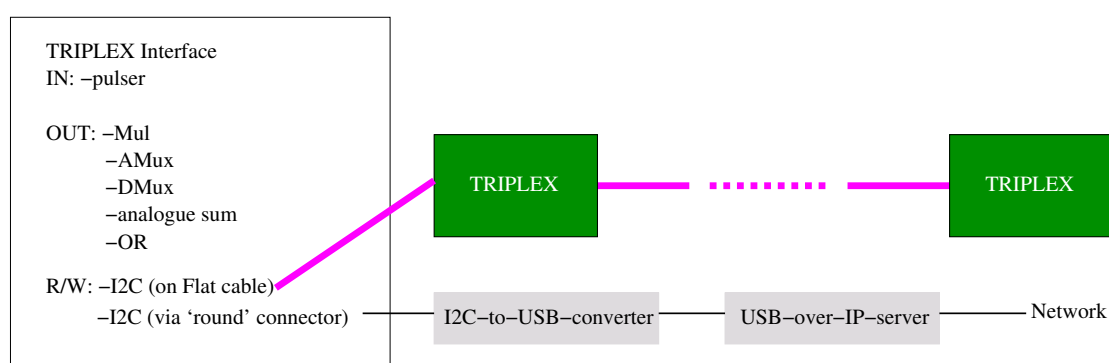
Figure B.16: A schematic of the TRIPLEX setup is shown. One can see how the TRIPLEX tree is connected to the network via the I^{2}C-to-USB-converter and the USB-over-IP-server.

To get an idea about the timing of the TRIPLEX-chain a measurement with 1 card was done. The delay between a pulser input connected to the FEE and the lemo-Mul-output of the TRIPLEX interface amounts to ∼42 ns. This measurement was done using a TacQuila system whose TRIPLEX card was at the topmost position in the TRIPLEX tree. Using a card which is in lowest (6th) level of the tree adds ∼40 ns of delay.

Possible Settings and connections on the TRIPLEX board itself are shown in figure B.6 and B.15.

The TRIPLEX board has several LEDs. At the moment only the first two are used. The first LED indicates that one of the corresponding FEE channels fired, while the second one shows when the TRIPLEX pulser is used.

The I^2C-to-USB-converter and USB-over-IP-server might in the future be replaced by a modified version of the HADSHOPOMO* which will be used as a I^2C to Ethernet converter. Furthermore, to simplify the Slow Control of the TacQuilas the Triplex settings will be integrated into EPICS.

B.3.1 TRIPLEX-I^{2}C-Address-Tree of LAND

To understand the cabling scheme of the TRIPLEX tree which is used for LAND first the addressing within this tree has to be explained. Each TRIPLEX board holds two registers (Part-U12 and Part-U13), see figure B.15. The settings of a TRIPLEX board (e.g. thresholds) are written into these registers. To do this one has to be able to address them. This is done via the I^2C bus which is directed using multiplexers on each TRIPLEX card. The information flow on one Y-cross in the I^2C bus is exemplary shown in figure B.17, the full TRIPLEX tree is build out of many such crosses. The way how this is realized at the moment creates some limitations for the available address-space. A nicer solution is shown in figure B.18. Using this scheme for the information routing not each register is on the main path, and therefore the addresses could be used several times within one branch of the tree.

The addresses of the multiplexer and both registers are defined via the HEX-switch on the TRIPLEX board. How the device addressing has to be done for the multiplexer and the register is shown in figure B.19 and figure B.20, respectively. Here one sees that only three bits (in the figures labeled as 'HARDWARE SELECTABLE') can be changed for the address of each part. These three bits and therefore the addresses of the registers are directly defined by the HEX switch of the corresponding TRIPLEX card. The HEX address of a TRIPLEX board is four bits long (e.g. HEX-address=A → binary=1010). Out of these four bits the first three are used to generate the address of the multiplexer and one register, while for the second register the three last bits are used.

All combination of addresses for the multiplexer and both registers which one can gener-

---

*<u>HAD</u>es <u>SHO</u>wer <u>PO</u>wer <u>MO</u>nitor
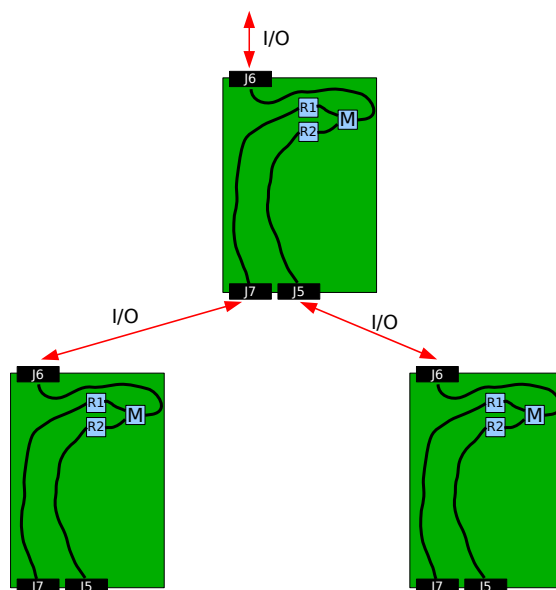
Figure B.17: Information-Flow for one of the Y crosses which appear within the TRIPLEX tree. This is a schematic of the situation how it is realized at the moment.
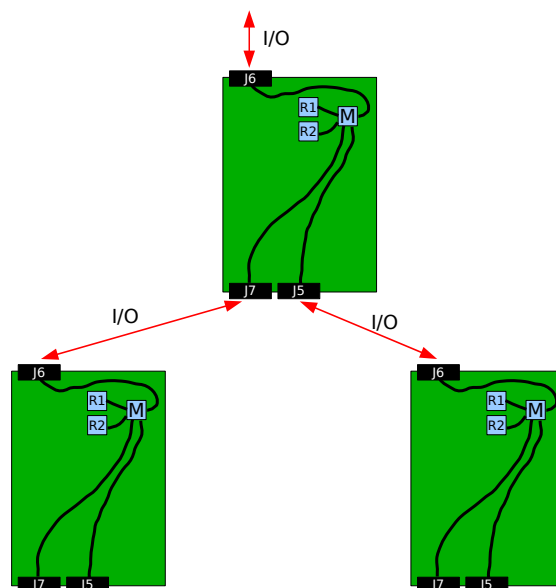
Figure B.18: Optimized information-Flow for one of the Y crosses which appear within the TRIPLEX tree. If this scheme would be used the addresses of the registers would not constrain the TRIPLEX tree. This should be applied for future developments.

ate by changing the HEX switch on the TRIPLEX board are shown in table B.6. Using the 14 sets of available addresses (see table B.6) one has to build a I^2C Tree. While doing

113
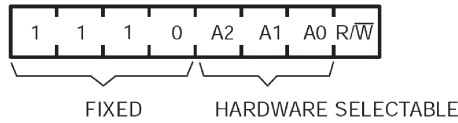
Figure B.19: The device addressing for the 8-channel I^{2}C-bus multiplexer PCA9547 is shown. This part can be found on each TRIPLEX board labeled as PART-U11, see e.g. figure B.15.
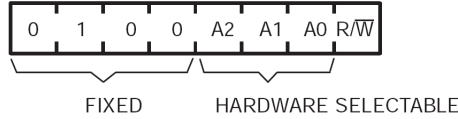
Figure B.20: The device addressing for the 8-bit I^{2}C I/O port PCA9554 is shown. Two of these devices are mounted on each TRIPLEX board, labeled as PART-U12 and PART-U13, see e.g. figure B.15.

HEX-switch	multiplexer-addr.	register-1 addr.	register-2 addr.
0	70	20	20
1	71	21	20
2	72	22	21
3	73	23	21
4	74	24	22
5	75	25	22
6	76	26	23
7	77	27	23
8	70	20	24
9	71	21	24
A	72	22	25
B	73	23	25
C	74	24	26
D	75	25	26
E	76	26	27
F	77	27	27

Table B.6: In this table the addresses of the multiplexer and both registers on the I^{2}C bus are shown. All numbers are in HEX. The combinations of addresses are a direct consequence of the chosen address on the HEX-switch. Since for the HEX-switch-addresses 0 and F both registers on one card have the same address these HEX addresses can never be used.

so one has to consider that on each path each address can only be used once. Currently we use a tree which allows to combine 40 TRIPLEX cards to one TRIPLEX-interface, this tree is shown in figure B.21.

At the current LAND setup three TacQuila crates are in operation, each crate holds ten

TacQuilas, twentyfive of those are used for LAND itself. The remaining five systems are used for Veto, see Sec. B.3.2 and as backup. The corresponding TRIPLEX cards have to be interconnected to deliver, e.g., one LAND multiplicity. To do so the TRIPLEX tree has been arranged in the way shown in figure B.22. If one wants e.g. change a TRIPLEX board due to maintenance, one has to make sure that the new card has the right HEX address to not destroy the TRIPLEX tree. For that reason the Hex-Address is also written to each TacQuila system in the crate. Furthermore, the HEX Addresses are given several times in this document, see figure B.21, B.22, B.23 and table B.9.
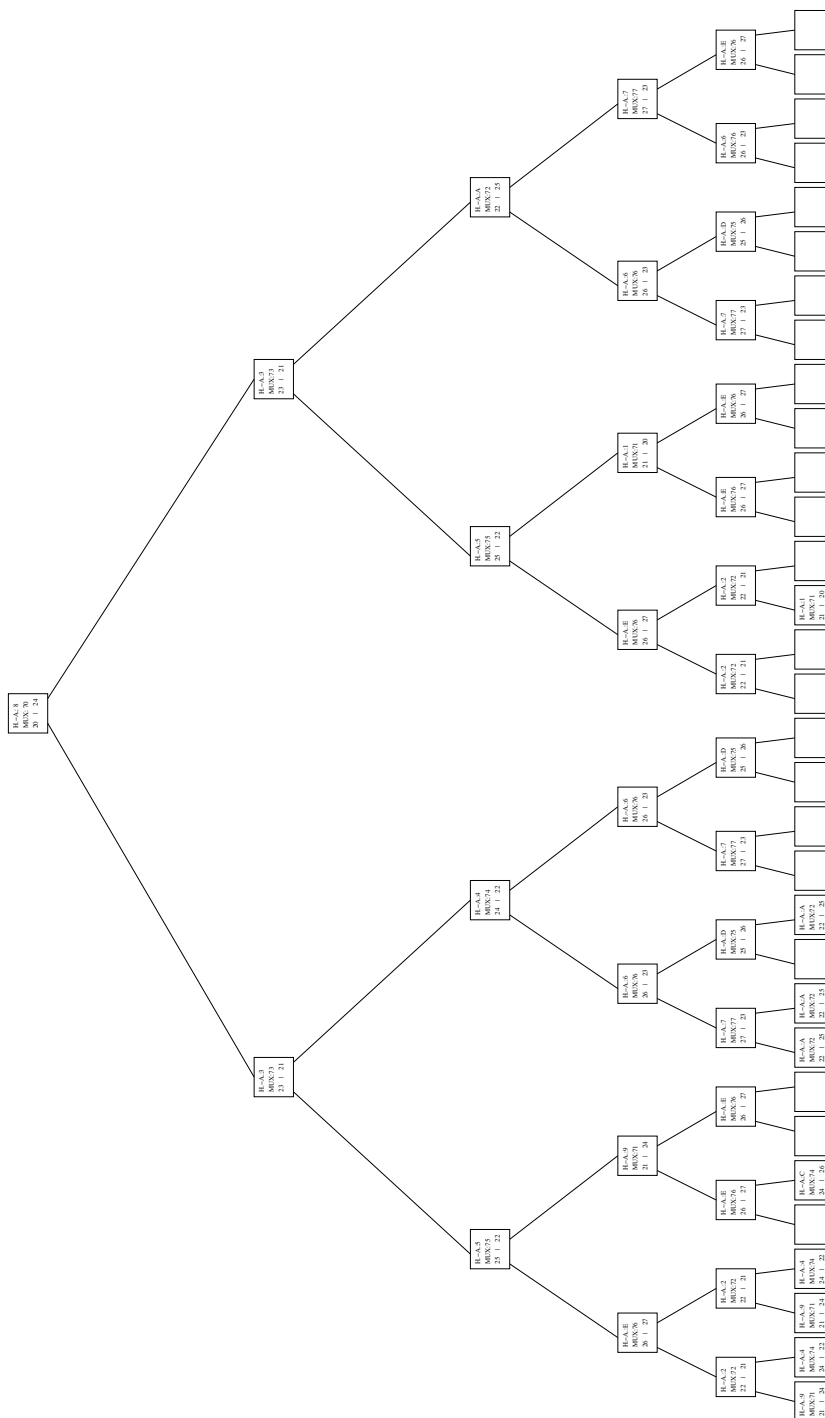
Figure B.21: Ordering of all 40 TRIPLEX cards in the I²C-bus. This is in principle the same scheme then shown in figure B.7. Each box represents one TRIPLEX card. H.-A. is the HEX address of the TRIPLEX card while MUX is the address of the multiplexer. The two numbers given in the bottom line of each box are the addresses of the two registers.
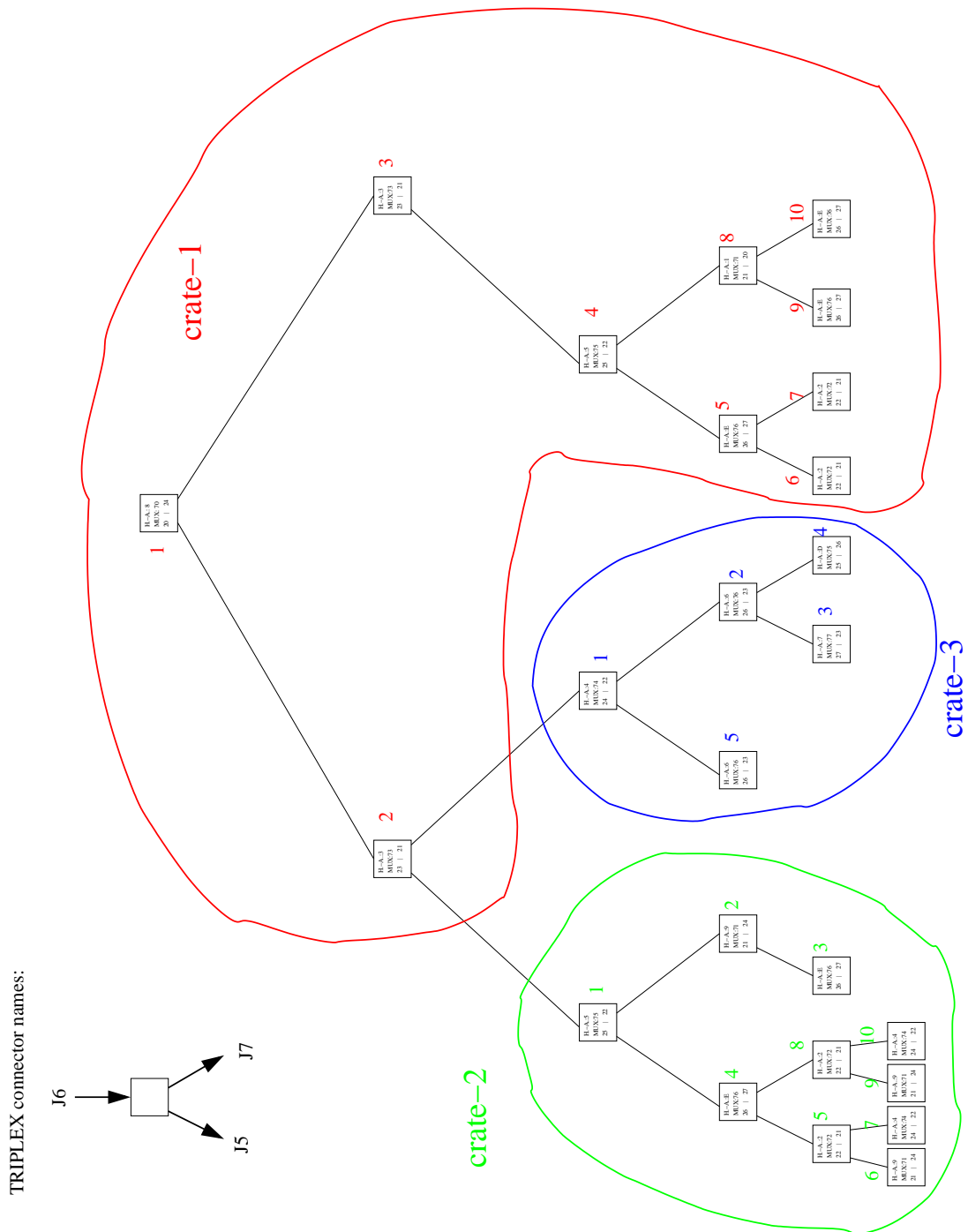
Figure B.22: Shown is which parts of the address-space for the TRIPLEX-tree is used for the LAND electronics. The tree is split such that one has only one interconnection between the three crates. How this is arranged into the crates can be seen in figure B.23.
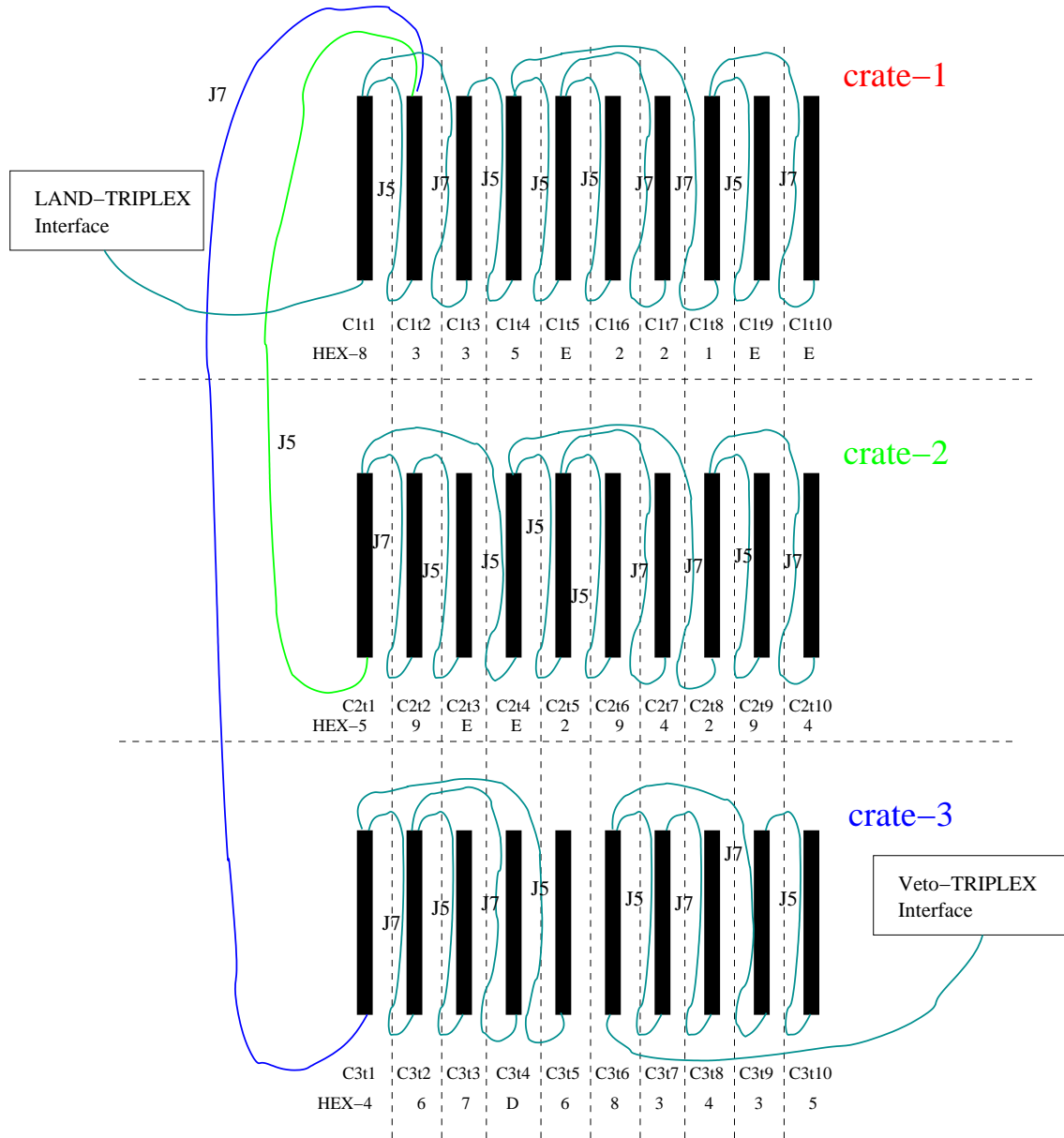
Figure B.23: Shown is the cabling of the TRIPLEX cards which build the LAND-TRIPLEX-tree and the Veto-TRIPLEX-tree. The following things are indicated:
1) place in the crate e.g. C1t1 means Crate 1 TacQuila 1.
2) needed HEX-Address at this position.
3) which connector one has to use for the cabling (J5 or J7).

B.3.2   TRIPLEX-I^{2}C-Address-Tree of VETO

As mentioned already thirty TacQuila systems are mounted currently at the LAND setup. Twentyfive of those are used for LAND itself and are connected to one TRIPLEX-tree, see Sec. B.3.1. The remaining five systems are connected to a second TRIPLEX-tree. This is here called Veto-Tree, where Veto refers to the additional scintillator plane mounted infront of the actually LAND detector which is used as a veto for charged particles. Out of the five TacQuila systems three are used for this Veto detector, while the other two cards are used for test systems and as backup.
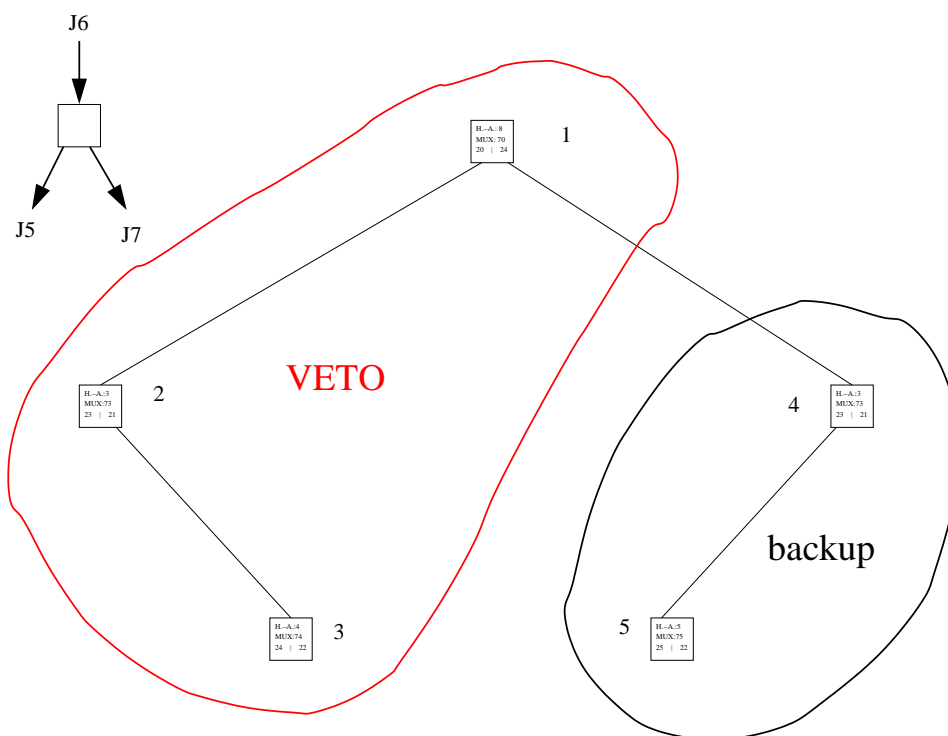
Figure B.24: Shown is which parts of the address-space for the TRIPLEX-tree is used for Veto and as backup. Where the cards can be found in the crate can be seen in figure B.23.

B.4 TacQuila[17]

The original TacQuila board, developed for FOPI, has 16 channels. Each of them measures a time relative to a external clock (at the moment a 40 MHz clock is used). As a result the time measurement is limited to a time smaller than 25 ns. The R^3B-TacQuila boards have an additional 17th channel. This is why the board is also called TacQuila[17]. Using this additional channel the time measurement is divided in a fine measurement (relative to the clock) and a coarse measure. The coarse measure counts the amount of clock cycles between the event in the channel and the one in the 17th. As a consequence the time measurement is now not limited. But it can be restricted. The restricting parameter called reset-time can be set software wise, see also Sec. B.1. If the reset-time is enabled in `tacset.txt` it is the maximum up to which the clock counter can go. If the 17th channel did not fire in the time-window set by the reset time, the event is discarded. The 17th channel is not connected on the FEE but directly on the TacQuila board, a signal in PECL* standard has to be used here. At the moment the 17th channels of all TacQuila boards are feed using the level converter† shown in figure B.41.
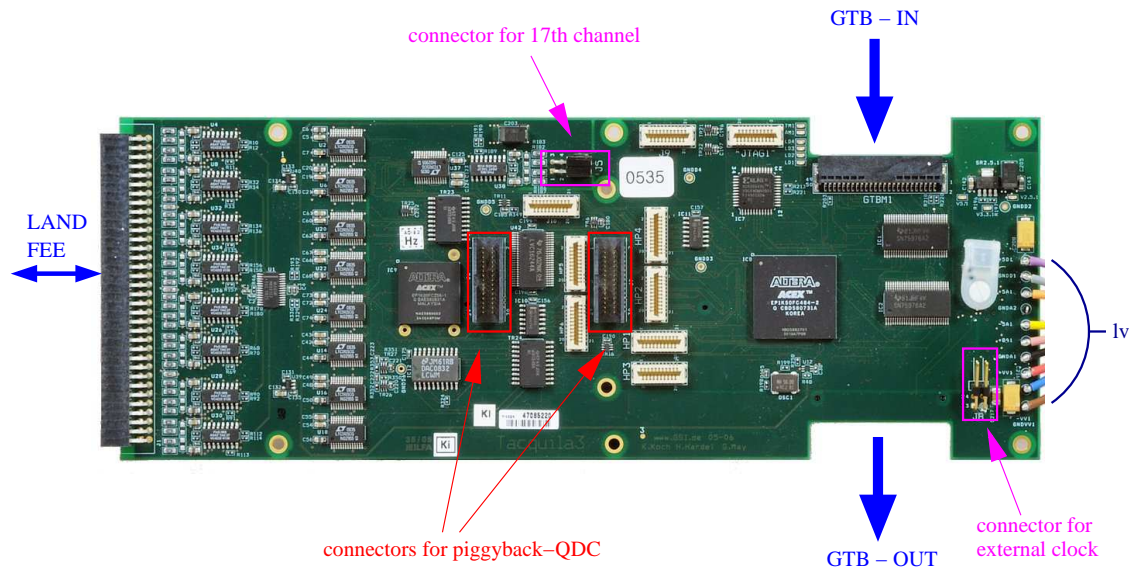
Figure B.25: Shown is the TacQuila[17] board. It is indicated where to connect: the piggyback QDC, the LAND FEE, the GTB bus (GTB In means the side which is closer to the SAM, while Out corresponds to the side which is closer to the terminator of the chain), the clock, the 17th channel and the lv.

The TacQuila time measurement is realized in the following way, see also figure B.26. Each channel starts its own time measurement. The so called TAC value is measured till the next rising edge of the clock. At this point the clock counter of this particular

---

*Positive Emitter Coupled Logic
†the official GSI-name of this device is: SIS-CLOCK-DISTRIBUTION

channel starts counting. The clock counters of channel 1-16 are stopped by channel 17. Channel 17 starts his own clock counter like the other channels, but this is stopped by the trigger (coming on GTB). So clock$_{17}$ gives an idea about the delay between channel 17 and the readout trigger coming on the GTB bus. The 17th channel performs a normal TAC measurement like the other 16 channels. Having these individual measurements the timing of one channel can be calculated using:

$$t_i = t(tac_i) - t(tac_{17}) + \frac{counter_i}{clock frequency} \; , \tag{B.1}$$

where $t(tac_i)$ is tac_i converted from channels to times.
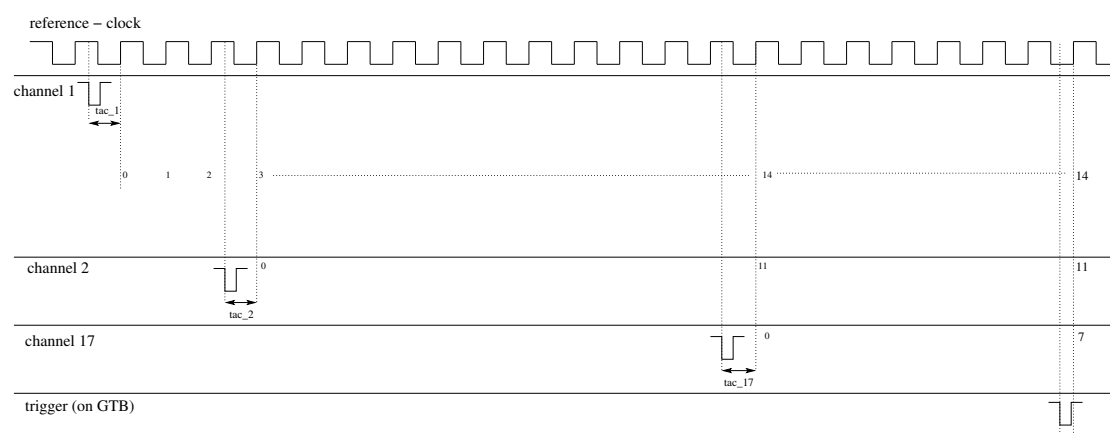
Figure B.26: Shown is how the TacQuila timing works, for the explanation see text.

The calibration (converting channels to ns) of the TAC measurement is at the moment done following a method suggested by N. Kurz. One records a white spectrum and gets a histogram like shown in the upper pad of figure B.27. To convert the channels to times one uses the information that the width of the spectrum is given by the clock frequency. This is described by,

$$t(channel) = (\frac{1}{clock frequency}) * (\frac{B}{A}) \; , \tag{B.2}$$

where:
A $\equiv$ whole integral
B $\equiv$ integral up to certain channel.

The disadvantage of this method is that high statistics are needed. But on the other side all data can be used for the calibration. No special events (e.g. tcal trigger) are needed. The calibration parameters should be monitored over time, since the TAC measurement shows a weak temperature dependence, see figure B.28.
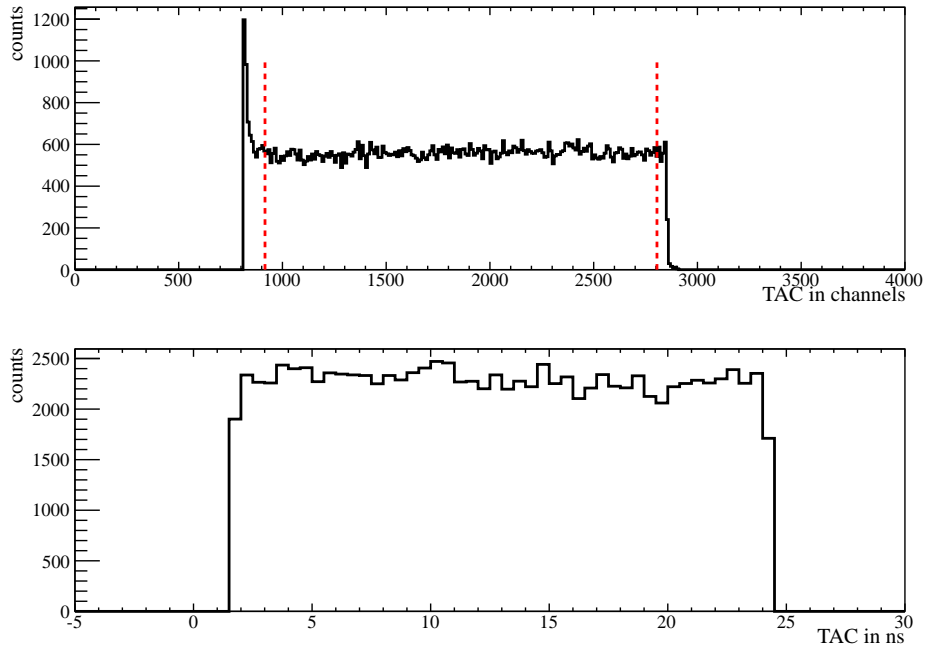
Figure B.27: In the upper pad a raw TAC spectrum is shown. The non-linearity at the edges can be seen. This particular shape is an intrinsic property of the TAC chip, see also section B.9. N. Kurz suggested to cut these events and during the test-phase this was done to have a cleaner sample of events. The cuts are indicated by the red, dotted lines. The lower panel shows the calibrated time spectrum in ns after applying the cuts.
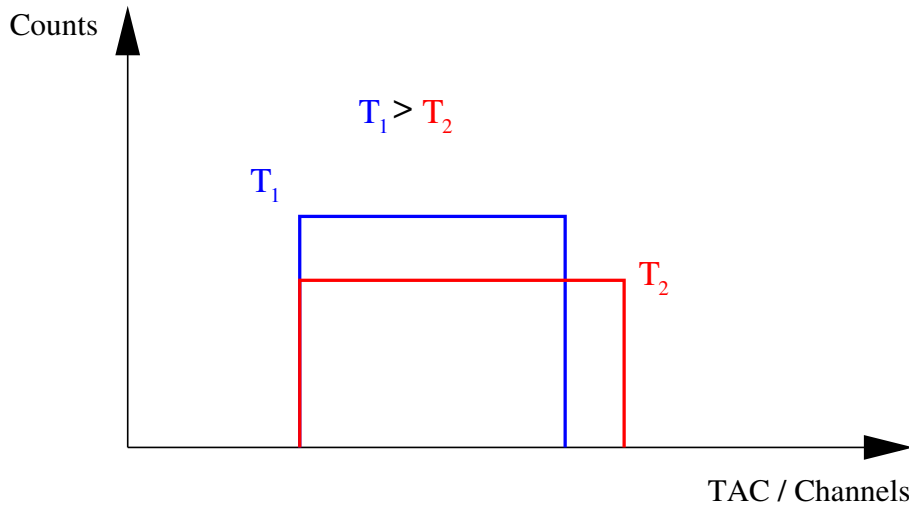
Figure B.28: Shown is schematically how the TAC-spectrum changes with temperature. Only the right edge moves. The change is in reality much smaller than shown in the picture.

To test the resolution of the TacQuila system the time difference between two channels is used. Here first a measurement is presented which highlights a specific feature of a time measurement which is done using a 'random' common stop like it is the case for the TacQuilas. The input at one of the channels is delayed relative to the other one (by $\sim$12 ns $\approx$ half a clock cycle). From such a measurement one gets two types of events like shown in figure B.29. In case A both TAC values are measured relative to the same clock-rising-edge. But in case B relative to two successive ones. The time difference (t_d) is calculated using:

$$t_1 > t_2 : t_d = t_1 - t_2 \ , \tag{B.3}$$

$$t_1 < t_2 : t_d = t_{clk} + t_1 - t_2 \ , \tag{B.4}$$

with t_{clk} = clock-cycle $\sim$ 25 ns.
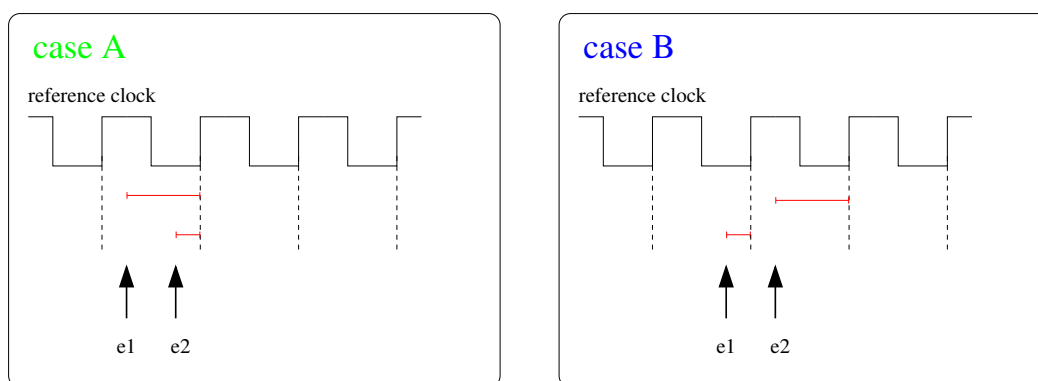
Figure B.29: Shown are the two types of events which one can get if two events (e1 and e2) with a fixed delay ($\sim$12 ns) are used as an input. Either they are measured relative to the same rising edge of the clock (case A) or they are measured versus the rising edges of two successive clock cycles (case B).

Looking at a time difference spectra, see figure B.30, one gets two contributions, which reflect the two types of events shown in figure B.29. For this example the resolution is $\sim$24 ps, it was chosen to illustrate the two types of events. The here presented way, in which the time difference between two events is limited to 25 ns, is exactly how the TacQuila readout is used by FOPI.

As mentioned already in the introduction a time resolution on one TacQuila card of $\sim$10 ps is achievable, see figure B.31. Measuring a time difference using channels from two different TacQuila systems worsens the resolution slightly.

For completeness of this section the calibration trigger will be discussed as the last topic. The TacQuilas accept two different trigger types (see also Sec. B.1), the physics trigger (trigger = 1) and the calibration trigger (trigger = 2). The calibration trigger comes always at $\sim$80% of the width of the TAC spectrum. So it could for example be
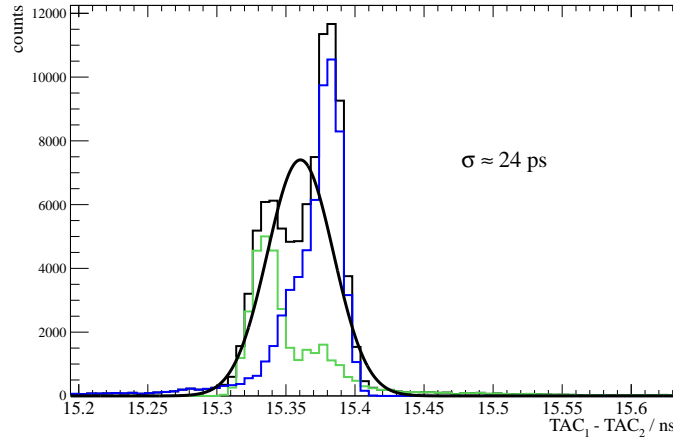
Figure B.30: Shown is the time difference between two calibrated channels in ns. For these two channels inputs with a fixed delay have been used. In black the whole data is shown. The green and blue peaks show the contributions of the two different event types, see figure B.29.
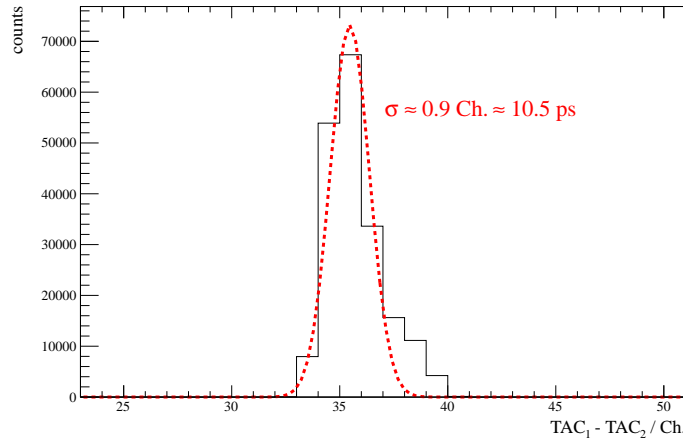
Figure B.31: Shown is the difference between two RAW TAC measurements. In this example the full TRIPLEX-LAND tree was triggered using the TRIPLEX pulser. The width of a TAC spectra is ~ 2150 channels, see e.g. figure B.27, this reflects the 25 ns of the Clock. Therefore the bin width is (assuming a linear conversion) ~ 12 ps. Hence, the here achieved resolution is $\sigma \sim 10.5$ ps. In general the relation 1 channel=12 ps can be used as a figure of merit for the TacQuilas.

used to monitor the movement of the right edge with temperature. But in the LAND DAQ only the physics trigger is used. This was suggested by N. Kurz for the following reason, the calibration trigger destroys the next physics event*.

---

*The statement in the EE is: In general the calibration trigger works, but the implementation in the

B.5 QDC

The working principle of the current QDC version will be explained in this section, the electronic board itself is shown in figure B.32, it has for each channel three stages:

- The first stage is a pulse integrator, it converts the voltage to a current. Only positive pulses are accepted. For the input on the FEE this means negative signals, since the amplifier does also invert the signal. The end of this stage is a RC component which (R=680 kΩ and C=100 pF in the first prototype version) has a time constant of ∼ 68 μs. The QDC has a virtual-gate. This means it is software wise set such that it reads the charge value 8 clock-cycles (200 ns) after the corresponding comparator fired. The discharging is only done via the RC component, there is no reset after a readout. The time constant defines directly the input frequency at which the measurement suffers from pileup, this is at ∼15 kHz (if one assumes that the time constant defines the limit for which pileup is not negligible).

- The second stage in the QDC channel is the baseline-restorer which cancels out slow (μs) variations of the baseline.

- The last stage is an ADC which converts the current to a 12 bit data word.
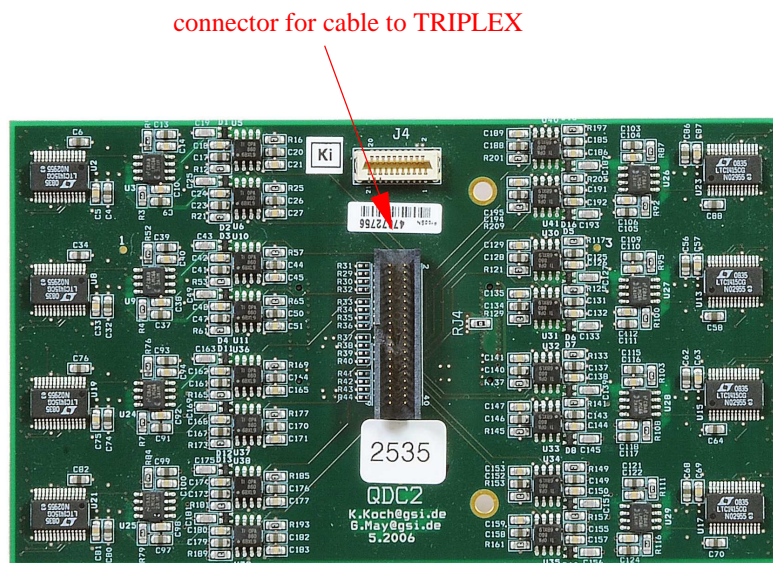
Figure B.32: Shown is the QDC2 piggyback board.

To get a QDC calibration several pulser measurements were done. Some of the results are shown here to see the basic characteristics of the QDC board, for more details see `https://elog.gsi.de/tacquila-test/273`. The shape of the 'QDC-channel vs.

SAM is not done perfect.

injected-charge' spectrum is like the one of a saturation curve, see figure B.33. This was a feature which FOPI wanted to have, since they want higher resolution for small charges. The charge measurement is in the FOPI case only needed to perform a walk correction. The decrease of the resolution with higher injected charge can be seen in figure B.34.

For the experiments s393, s306b and s389 the NTF* was read out with FaBu electronics and TacQuila electronics at the same time to see the correlations between the two read-out systems. One result is shown in figure B.35. Again the non-linearity of the TacQuila QDC measurement can be seen.

Prior to these experiments the following modifications have been done:

1. software: In the initial version only 10 of the 12 bits were read and the QDC was read at the time the trigger on GTB reached the TacQuilas. Nowadays all 12 bit are read 8 clock cycles after the comparator triggered.

2. hardware: The resistor of the RC component was replaced by a 150 kΩ component, giving a smaller time-constant. Figure B.36 shows K. Koch's measurements with the new resistor and software, the values are shown in table B.7

The modifications of the QDC board improve the charge measurement in two aspects, both, the dynamic range and the rate capability increase.

voltage / V	mean-QDC pulse1	mean-QDC pulse2
3.67	2617	490
1.93	2477	400
1.03	2329	355
0.475	2033	290
0.125	1279	188
0.055	809	114

Table B.7: The QDC characteristics have been investigated for two different pulses. Pulse-1 has: t_{fall} =15 ns and t_{rise} =100 ns. Pulse-2 has: t_{fall} =2 ns and t_{rise} =10 ns. The amplitude has been modified to scan the QDC range. See figure B.36 for a graphical representation.

---

*New Time of Flight wall
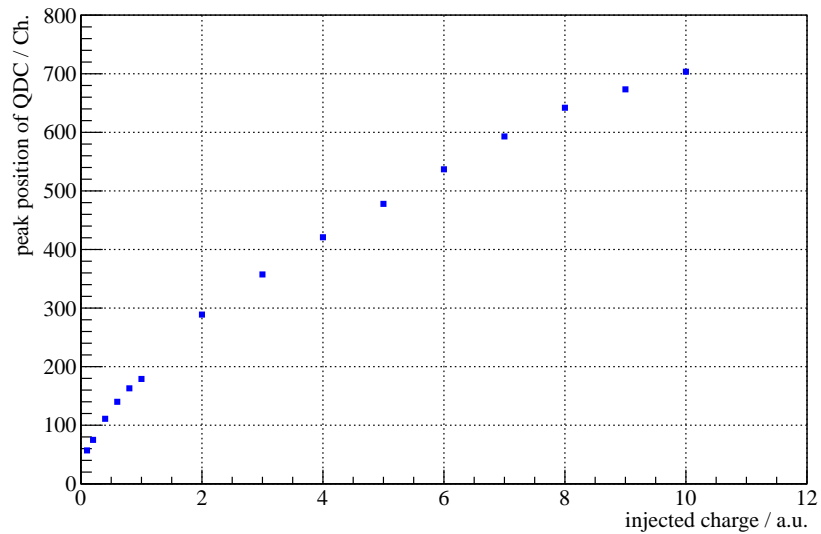
Figure B.33: The injected charge in a.u. vs. the mean of the QDC peak is shown. The measurements were done using a pulser, the pulse was scaled using amplifiers and attenuators. The original pulse (injected-charge=1) has a charge of ≈ 23 nC. Hence, the measurements are in a range from 2.3 nC to 230 nC. For smaller values the threshold could not be adjusted in a way that the signals were still accepted. One sees that only a quarter of the 12 bit QDC range is covered. For higher charges the measurements become more difficult due to saturation effects.
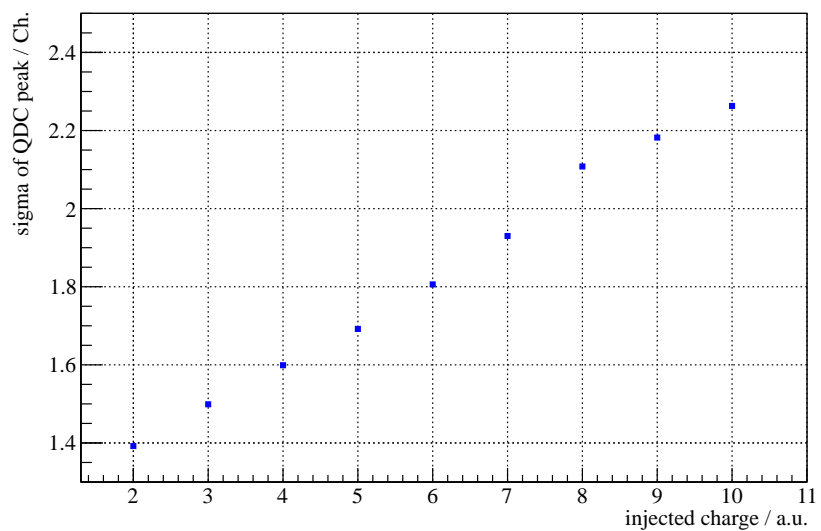
Figure B.34: Shown is the sigma of the QDC peak vs. the charge in a.u. A decrease of resolution with higher charges can be seen.

127
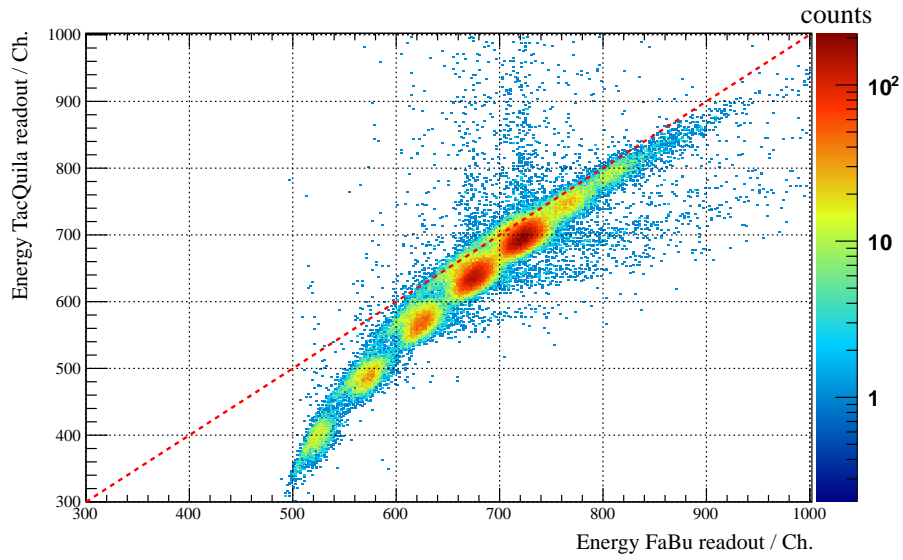
Figure B.35: The correlation between the TacQuila and FaBu readout is shown for data taken during the s393 experiment. Plotted is the $E_{mean} = \sqrt{E_1 \cdot E_2}$ for the y-paddle which was mainly hit by the beam measured with the TacQuilas and FaBu, respectively. The red dotted line represents the diagonal.
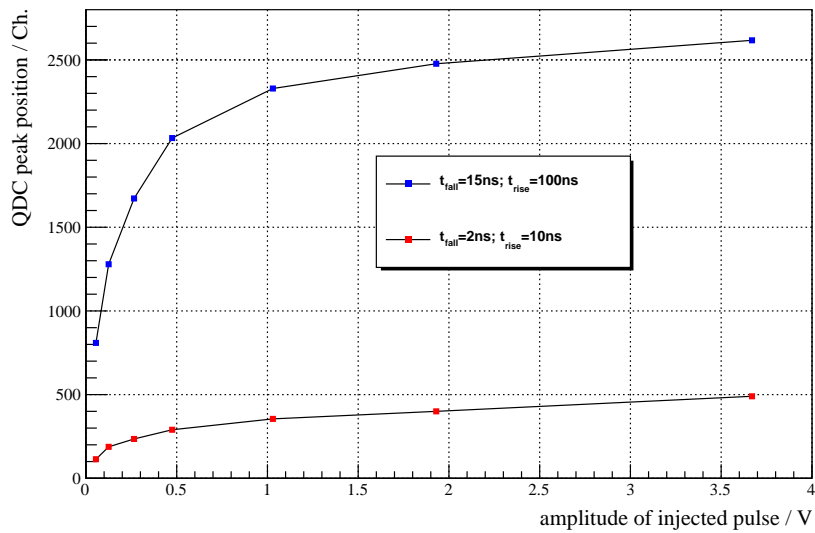
Figure B.36: Shown is the correlation between injected and measured charge. For details see text and table B.7.

B.6   Low Voltage

The lv distribution for the TacQuilas is done using five TDK LAMBDA power supplies (GEN-8-180 / LN). Each of them can provide 0-8 V and 0-180 A. The access and control of those power supplies is realized using EPICS. The first power module (master) has an ethernet connection. The other four modules are daisy-chained to the master via RS485 standard. The EPICS-GUI* can be found in:

`/u/land/LANDLV`

execute the following shell script to start it:

`./tacquila_startGUI.sh`

The TacQuila-lv-GUI can also be opened via the standard LANDHV GUI. There one will find a button for the TacQuilas at the right bottom. A window like shown in figure B.37 will be opened. This can be used to switch the supplies on and off and to monitor the voltage and current of each device, it is not possible to set voltages here. The idea is that one can only change the voltage values at the devices themselves. In principle the power supplies can also be controlled using a web interface (`landlv002.gsi.de`). The user is admin, no password is needed. The web-interface is not working reliable so it should normally not be used. However, as backup solution to check the voltages it could be useful in case that e.g. the EPICS server does not work. To restart the EPICS server in this case follow the HowTo on the `land02` webpage.

To be able to estimate typical values of the currents which one TacQuila system draws, the consumption, per system is given in table B.8.

No.	voltage / V	comment	current / A
1	+7	needed by FEE and external reference clock	0.04
2	+5	analogue and digital (needed by TacQuila and QDC)	1.2
3	-5	used by TRIPLEX	0.6
4	-5	used by QDC	0.3
5	+6	used by FEE (pre-amp.) and TRIPLEX	1.8

Table B.8: The first column shows the numbering of the lv modules. In the second one the nominal voltages for a TacQuila readout system are given. The voltages at the lv modules might differ, e.g. due to losses. The third column explains which parts use the different voltages. The last column gives the current one full TacQuila system draws for each power supply. On top small currents are needed by e.g.: LVTTL-to-PECL-converter.

The voltages which one TacQuila-system needs are given in figure B.38. Out of the nine voltages (six voltages plus three grounds) the board is only supplied with six (five voltages plus one ground). The voltages +5 analogue and digital are both feed using the

---

*Graphical Under Interface
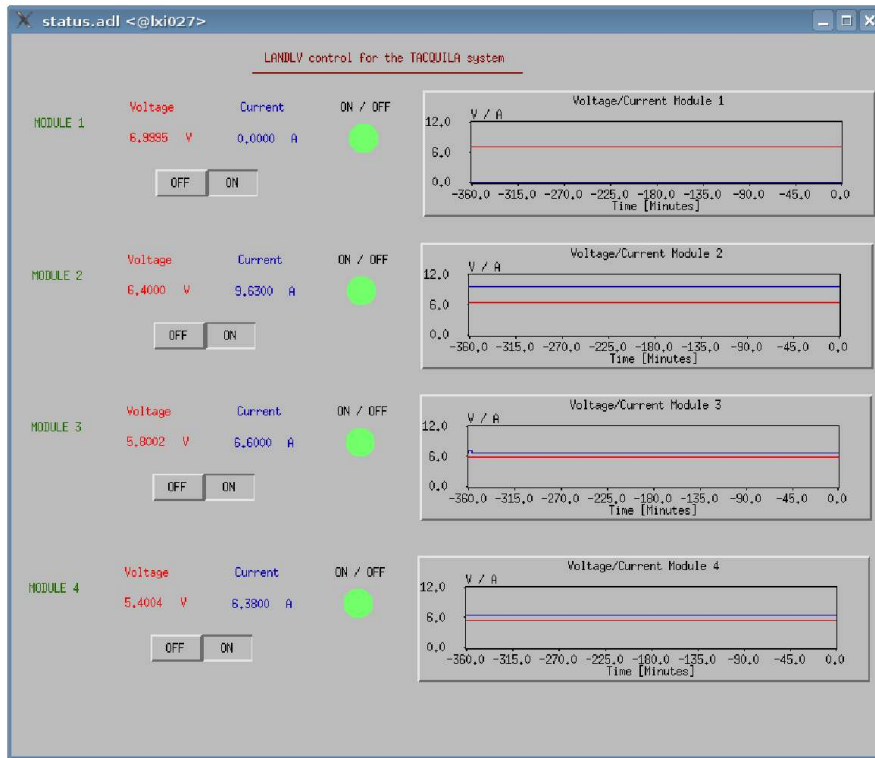
Figure B.37: Shown is a screen shot of the EPICS GUI for the TacQuila lv modules.

same power supply, see also table B.8. Furthermore, all grounds are connected together. For the distribution of the lv to the different devices two different schemes are available:

1. A FOPI lv distribution board, see figure B.39 is/was used for tests.
2. For the LAND-TacQuila-Crates a distribution system using WAGO* Rail-Mounted-Terminal-Blocks has been designed.

The 2nd scheme will now be discussed in more detail. From the power supplies a master-distribution is feed, also a sensing to this point is foreseen for the future. The cables from the power supplies to the master-distribution have a cross-section of 16 mm^2. Each TacQuila crate has a lv-distribution which is used for the ten TacQuilas in the crate as well as the clock and the 17th-channel-distribution. The connections from the master-distribution to those sub-distributions is done using cables with a cross-section of 10 mm^2. In the sub-distributions each voltage is connected to ground several times using 470 μF capacitors to make the voltages more smooth. Such a sub-distribution is shown in figure B.40. In the shown picture all Rail-Mounted-Terminal-Blocks for one crate are mounted but only the cables for one out of the ten TacQuila systems are connected.

---

*Name of the company which produces the parts.
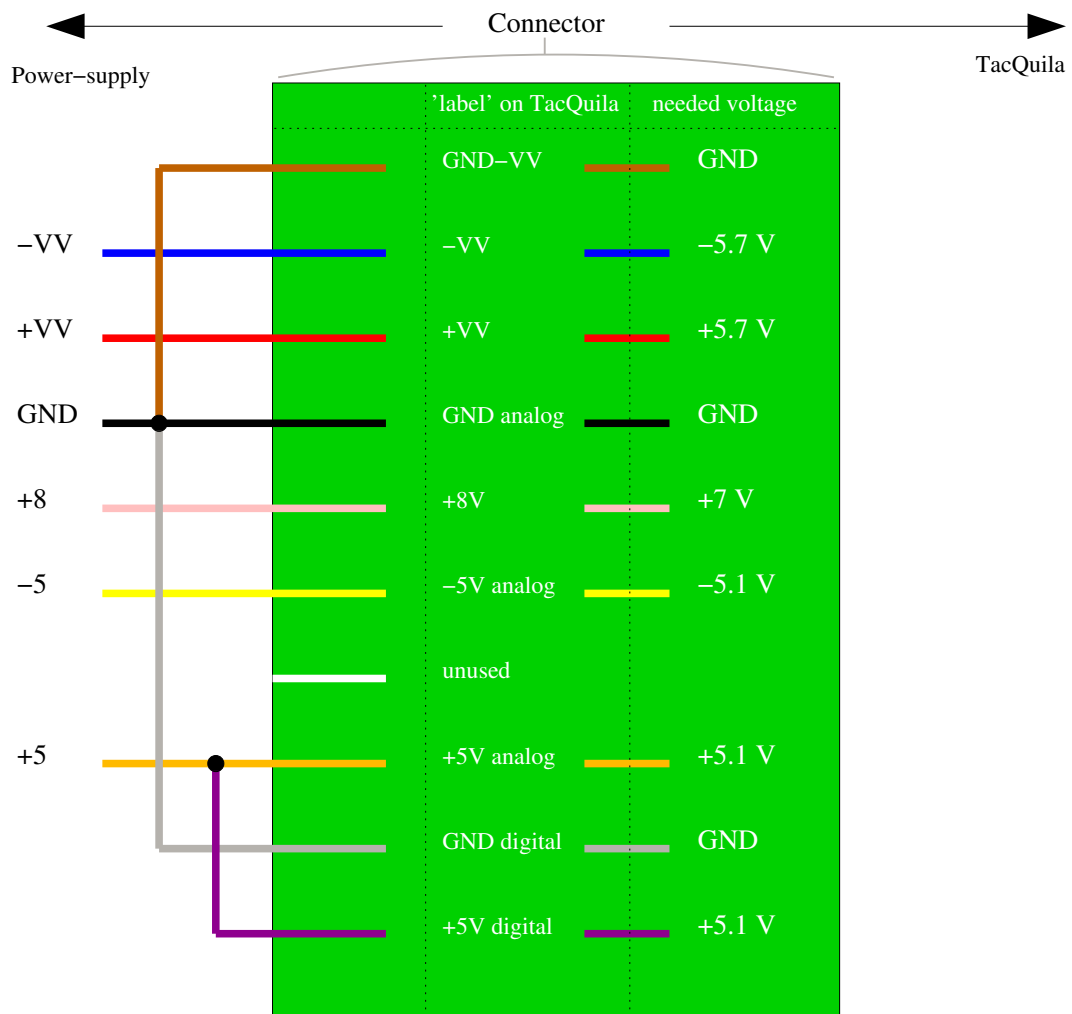
Figure B.38: It is schematically shown how the lv distribution for the TacQuilas is realized. The color-code is shown. Furthermore, the values of the voltages which are needed on a TacQuila board are given as well as how they are labeled.
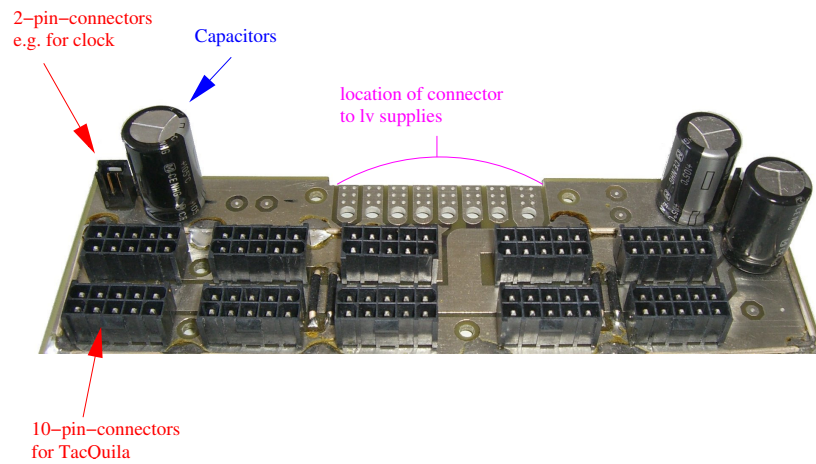
Figure B.39: Shown is the FOPI lv distribution board. There are two types of connectors on the board. Two 2-pin and ten 10-pin connectors. The 2-pin connectors are used to connect the clock and the LVTTL-to-PECL-converter. Here one has to be careful, since since it easy to reverse the polarity. The 10-pin connectors are used for the TacQuilas.
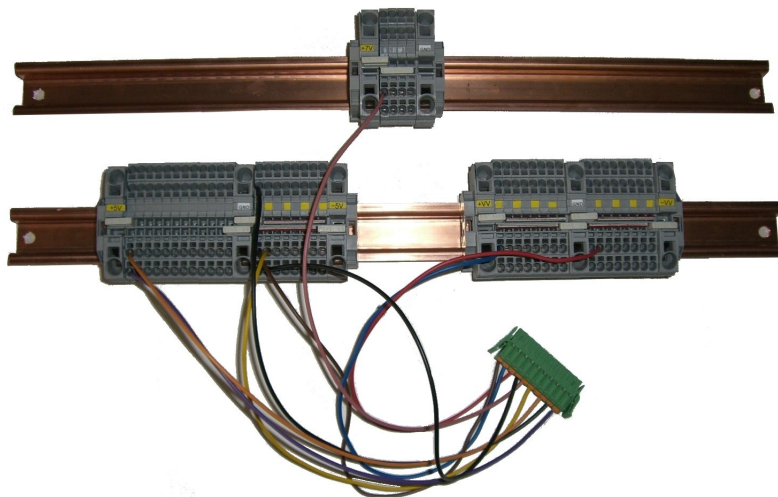
Figure B.40: Shown is one WAGO sub-distribution during the production. All Rail-Mounted-Terminal-Blocks are fixed to the rail. The cables for only one TacQuila system are connected.

B.7   Additional Electronics

In addition to the TacQuila-systems themselves some other electronic modules are needed to complete the readout electronics:

- A LVTTL-to-PECL-converter (SIS-Clk-Distribution), which distributes the 17th channel to the TacQuila boards, this module is shown in figure B.41. Three such devices are currently used to distribute the signal to all 30 TacQuilas. This three modules are connected from only one source using a LEVCON*.
  If one wants to monitor the output of the LVTTL-to-PECL-converter on a scope one has to be aware of how to measure a PECL signal. A nice FAQ concerning this topic can e.g. be found here:
  `http://www.pulseresearchlab.com/faqs/ecl_ques/ecl_q13-q16.htm`
  and a printout of this webpage can be found here:
  `/u/ccaesar/tacquila/FAQ_ECL_PECL.pdf`

- The clock-Distribution. At the moment an external 40 MHz clock is used as a reference for the time measurement of the TacQuilas. The module is shown in figure B.42. This will in the future be replaced by BuTiS†. The clock needs a voltage of +5 V. Up to ten TacQuila boards can be connected to one clock module. To have the same reference clock for all 30 TacQuila systems at LAND the clock shown in figure B.42 is used as a master-clock and three further modules are used as daughter-modules. Each of those is placed behind one TacQuila crate and used to distribute the clock signal to ten TacQuilas. The master-clock is also connected to the LEVCON, there the signal is converted to TTL and then connected to a scaler to monitor the clock frequency. See also:
  `www.gsi.de/informationen/wti/ee/elekt_entwicklung/clockdstr.html`
  to get further details on the clock modules.

- LEVCON, see:
  `http://www.gsi.de/informationen/wti/ee/elekt_entwicklung/levcon.html`
  for details on the module. In the LAND setup it is currently used to feed all three SIS-Clk-Distributions from the same source and to connect the clock to a scaler. See figure B.43. The used LEVCON has been specially programmed to be suited for the here shown task.

In addition to the above mentioned modules a NIM‡ crate is located close to LAND, it holds several modules which are e.g used to distribute a pulser or construct a trigger. In the NIM Crate the following modules can e.g. be found:

---

*programmable LEVel CONverter
†Bunch-phase Timing System
‡Nuclear Instrumentation Module standard

<dl>
<dd>LA8000 → Level Adapter. Converts from NIM to TTL. Is needed for the pulser inputs of the TRIPLEX interface.</dd>
<dd>CF8000 → Constant Fraction. Is used to discriminate the Mul signal delivered by the TRIPLEX interface.</dd>
</dl>

Furthermore, some VME modules are necessary to complete the readout electronics, see figure B.44:

RIO3 → computer in VME crate, MBS runs for example on this machine.

TRIVA5 → distributes DAQ-trigger, tells the DAQ at what time it has to read out the data.

TRIDI1 → distributes FEE-trigger here to TacQuila board.

SAM5 → Via GTB cables the readout of up to 60 TacQuila boards is done.

ENV1 → is a 16 Channel NIM-ECL-NIM level translator packaged in VME module. It converts in both directions between NIM and ECL logic families.

VULOM1 → VME Universal LOgic Module, is here used to do the dead time blocking.
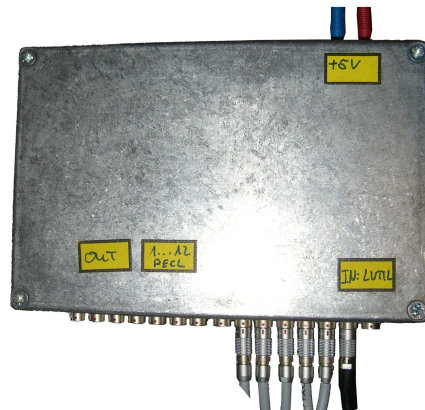
Figure B.41: Shown is the LVTTL to PECL converter. The device has to be supplied with +5 V. Having one LVTTL input twelve PECL outputs are available.

Figure B.42: Picture of the 40 MHz clock. The device needs +5 V. The clock can be distributed to up to 10 TacQuilas.
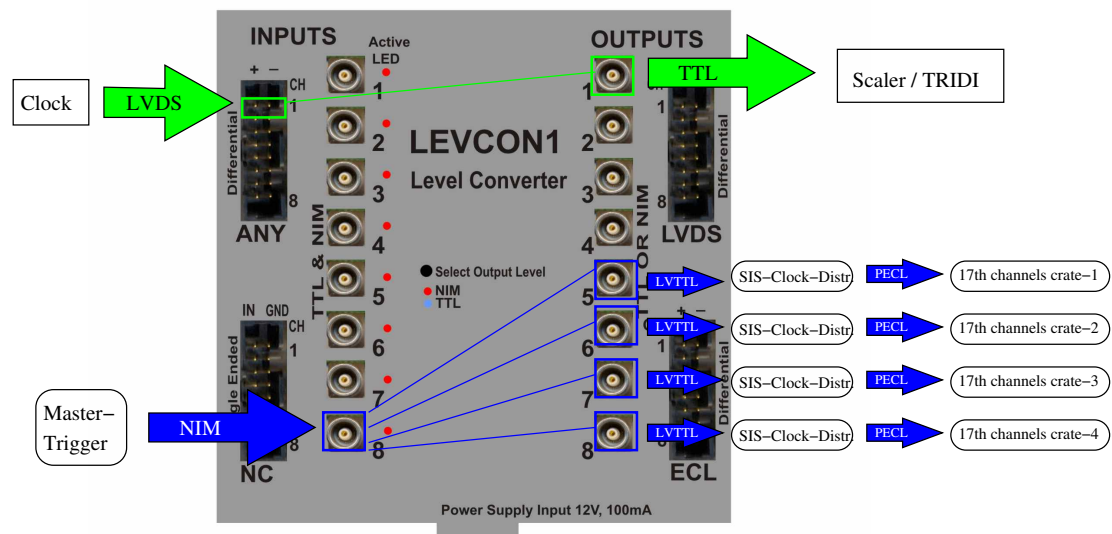
Figure B.43: Picture of the LEVCON. It is indicated how this module is used in the LAND setup at the moments.

135
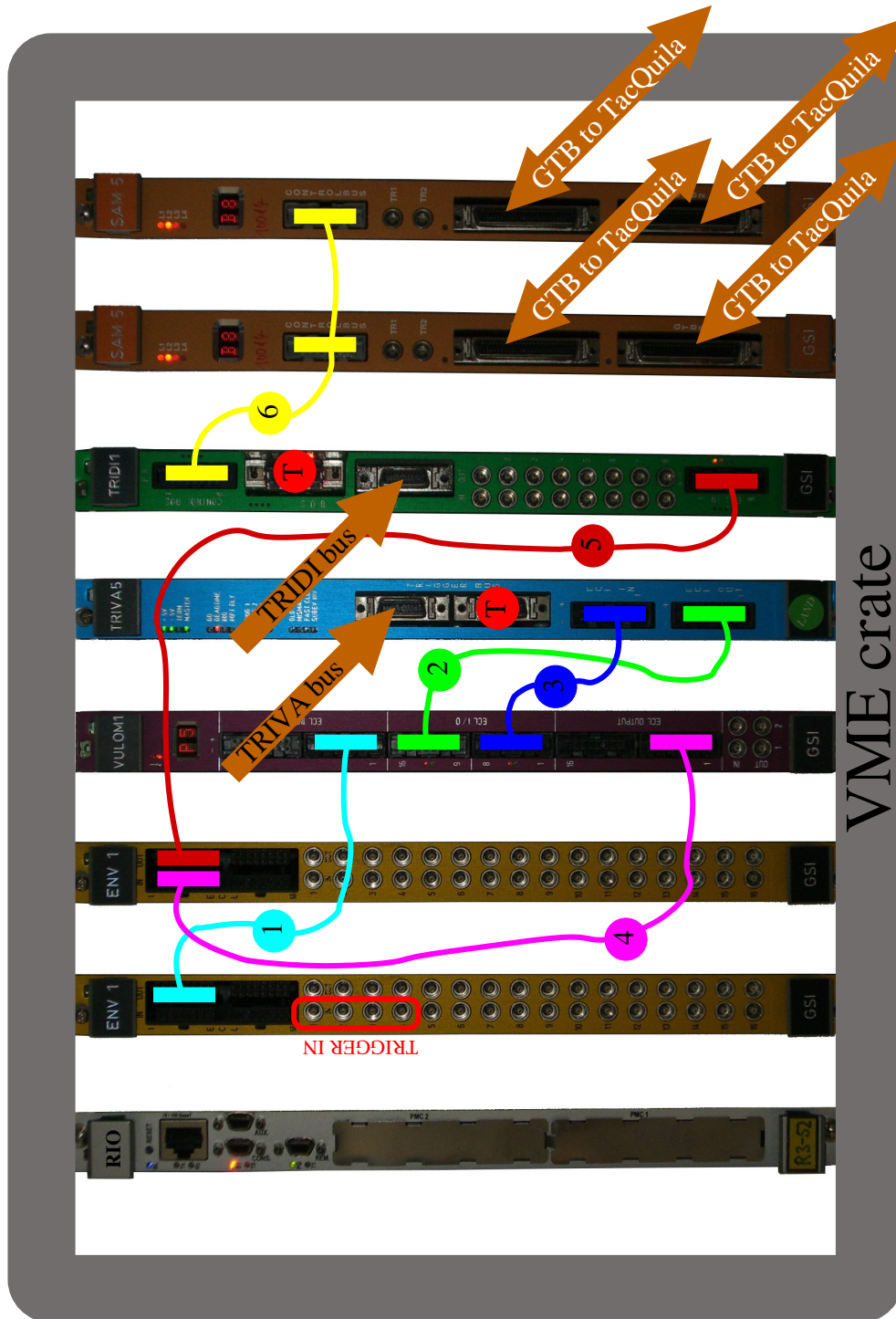
Figure B.44: Shown is exemplary how the VME crate for a TacQuila readout system could look like. For details see explanations in the text.

In the following paragraph it will be discussed how the TacQuila VME crate has to be cabled, the used numbers/labels refer to figure B.44. In the common LAND-DAQ we have four trigger those can be connected to the ENV*, see red-box in figure B.44. The ENV delivers the triggers to the VULOM (cable-1), which then does together with the TRIVA† (I/O interconnections: cable-2 and cable-3) the dead-time blocking. The dead-time free triggers are then in the here shown example connected again to an ENV (cable-4) to be able to monitor them on a scope. From the ENV the signal is routed to the TRIDI‡ (cable-5). The TRIDI delivers the trigger to the SAM (cable-6) which then distributes it via the GTB to the TacQuilas. For the interconnection between the TRIDI and the SAM one has to be a bit careful. The SAM has always to see a trigger 1, this can be achieved by either changing software-wise the mapping of the TRIDI or one does the same hardware wise using e.g. a FAN-In-FAN-Out.

Furthermore, one has to be aware that the mapping between the TRIDI-inputs and the outputs on the TRIDI-Ctrl-Bus is done in a cross-like manner:

$$
\begin{array}{ccc}
\text{TRIDI IN} & \leftrightarrow & \text{Ctrl Bus} \\
1 & \leftrightarrow & 5 \\
2 & \leftrightarrow & 6 \\
3 & \leftrightarrow & 7 \\
4 & \leftrightarrow & 8 \\
5 & \leftrightarrow & 1 \\
6 & \leftrightarrow & 2 \\
7 & \leftrightarrow & 3 \\
8 & \leftrightarrow & 4 \\
\end{array}
$$

This is only important if one wants to look at signals in between the TRIDI and the SAM. Since the mapping on the Ctrl-bus-inputs of the SAM are adapted to this cross-mapping the signal routing works if one inter-connects TRIDI and SAM using a standard flat 8-pin cable.

The VME crate used for LAND holds at the moment two SAMs, see figure B.44. These two SAMs are used to have at least three GTB chains for the three LAND TacQuila VME crates. As a consequence different HEX addresses have to be used for the device addressing on the VME bus for those SAMs. Currently this is 5 for the first SAM and 6 for the second. This offers four GTB connections (GTB_5_0, GTB_5_1, GTB_6_0 and GTB_6_1) out of which we currently use three. One GTB chain is used for each TacQuila crate. The connection is done in the following way:

- GTB_6_0 → TacQuila crate 1 (top),

---

* $\underline{\text{E}}$CL $\underline{\text{N}}$IM level converter embedded in a $\underline{\text{V}}$ME-module
† VME $\underline{\text{TRI}}$gger Synchronizing Module
‡ VME $\underline{\text{TRI}}$gger $\underline{\text{DI}}$stribution Module

- GTB_6_1 →TacQuila crate 2 (middle),
- GTB_5_0 → TacQuila crate 3 (bottom).

This means, all 20 modules on GTB_6_0 and GTB_6_1 are used for LAND. The modules one GTB_5_0 are split into two groups. The first five are also used for LAND, while the last five are used for Veto and as spare modules, see also Sec. B.3.1 and B.3.2 in particular figure B.23 shows how the modules are arranged. This information is needed to do the mapping from TacQuila channels to detector channels. If the full list for the mapping of each individual channels is needed please contact D. Rossi.

The TRIDI and TRIVA trigger bus-connectors have to be terminated (see red circles, which are labeled with 'T' in figure B.44). On the TRIVA bus the following signals are present:

$$1 \rightarrow \text{physics trigger}$$
$$2 \rightarrow \text{off spill trigger}$$
$$3 \rightarrow \text{clock}$$
$$4 \rightarrow \text{tcal}$$

On the TRIDI bus the triggers are ordered in the following way:

$$6 \rightarrow \text{clock}$$
$$7 \rightarrow \text{tcal}$$
$$8 \rightarrow \text{physics}$$

To trigger the 17th channel for physics events the trigger should never be taken from the TRIDI bus but from the original source using a direct cable. The signals coming via the TRIDI or TRIVA bus have a jitter since they are synchronized to the internal clock of the corresponding module.

Furthermore, one has to remember, that the output trigger type which the SAM delivers to the TacQuilas has always to be 1, this means one has to do the mapping accordingly. To see the current mapping which is used for a certain SAM one has to log-on to the RIO which is controlling the VME crate of that SAM and do e.g.:

`R3-30:/land/usr/land/tridis/ ./tridis2_rio3 -a3 -sl` if one is using a RIO3 and the HEX address of the TRIDI is 3, for more information see the help function of this program.

The SAM needs a certain firmware to work in conjunction with a TacQuila readout, how to change this firmware can, e.g., be found here:

`/u/land/lynx.landexp/SAM5/HowTo_flash_a_SAM5.txt`

The here presented VME setup explains all possible connections, which might not all be used at the same time. In stand-alone mode the TRIDI and TRIVA bus will e.g.

not be connected, while if the TacQuilas are readout in the main LAND DAQ the local VULOM is not needed. In a minimal setup one could operate the TacQuilas having only a RIO, TRIVA and SAM in the VME crate.

B.8 Miscellaneous

In the following chapter the needed cabling will be summarized for a full system, the SN* of all systems which are currently in use will be given and furthermore, the exact 'names' of the used parts to build (cable) the system will be tabulated.

B.8.1 Needed Cabling

To show what cabling is needed for one TacQuila system a possible design for a next generation front panel is shown in figure B.45.
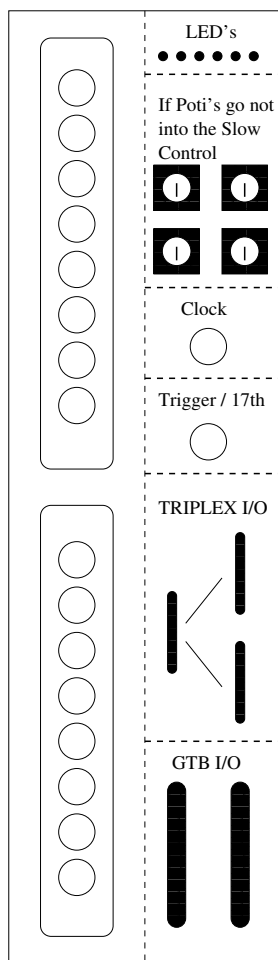
Figure B.45: Shown is how the front panel of a next generation TacQuila-system could look like. This displays nicely which connections are needed.

---

*Serial Number

The individual connections shown in figure B.45 are:

- The TacQuilas are readout via GTB. A cable has to be connected from the SAM to one TacQuila (in our setup the most right one in each crate). The other TacQuilas are daisy-chained to this one*. The last module in the chain will be called number 1 in the data. The bus has to be terminated at the end of the chain.

- Each TacQuila has to be connected to the clock, see figure B.25 and figure B.47.

- The 17th channel of each TacQuila has to be connected, see figure B.25 and figure B.46.

- Each TacQuila board has to be connected to the the lv power distribution. This is the only connection which is not shown in figure B.45, since this would stay at the backside of the module.

- The TRIPLEX-interface has to be connected to the I^{2}C-to-USB-converter, see figure B.16.

- The I^{2}C-to-USB-converter has to be connected to the USB over IP server.

- The TRIPLEX cards have to be connected among each other, see Sec. B.3.

- The pulser input should be connected to the TRIPLEX interface. The Triplex pulser events can be used to determine the pedestal. This is the only way to create a zero-charge event.
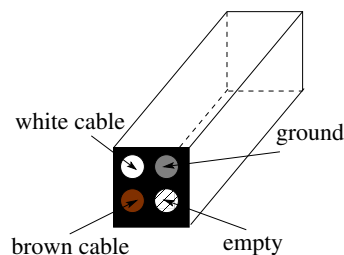
Figure B.46: The connector for the 17th channel on the TacQuila board is shown. It is indicated how to connect the 3-pin cable which is used to feed the 17th channel.

---

*The developers had up to 30 systems in one chain, but we faced data transfer problems having more then 10.
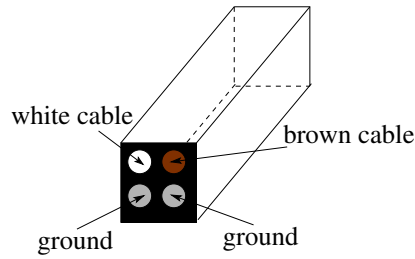
Figure B.47: The connector for the clock on the TacQuila board is shown. It is indicated how to connect the 4-pin cable which is used for the clock.

B.8.2 Used TacQuila Systems

Building up the new LAND readout electronics 30 TacQuila systems have been mounted in 3 Crates. In this section the SN of all sub-modules will be given. This information should in the future be integrated into the LAND-cabling-documentation.

position	TRIPLEX	FEE	TacQuila	QDC	HEX	used for
C1t1	..2	1539	514	2514	8	LAND
C1t2	..5	1509	430	2530	3	LAND
C1t3	..14	1534	509	2509	3	LAND
C1t4	..3	1516	526	2532	5	LAND
C1t5	..9	1501	502	2502	E	LAND
C1t6	.2	1536	507	2507	2	LAND
C1t7	..13	1535	508	2508	2	LAND
C1t8	.14	1511	515	2515	1	LAND
C1t9	..15	1519	516	2516	E	LAND
C1t10	..6	1515	505	2505	E	LAND
C2t1	SN11	1512	503	2503	5	LAND
C2t2	SN4	1513	512	2512	9	LAND
C2t3	.4	1529	537	2537	E	LAND
C2t4	..10	1518	528	2528	E	LAND
C2t5	..8	1514	511	2511	2	LAND
C2t6	.8	1531	504	2504	9	LAND
C2t7	.14	1517	506	2506	4	LAND
C2t8	.9	1532	518	2518	2	LAND
C2t9	.6	1533	510	2510	9	LAND
C2t10	SN3	1526	538	2006	4	LAND

position	TRIPLEX	FEE	TacQuila	QDC	HEX	used for
C3t1	SN6	1520	513	2513	4	LAND
C3t2	..11	1503	533	2533	5	LAND
C3t3	..4	1506	522	2527	7	LAND
C3t4	SN14	1540	529	2539	D	LAND
C3t5	SN12	1504	519	2519	6	LAND
C3t6	.7	1530	540	2536	8	VETO
C3t7	???	1528	523	2540	3	VETO
C3t8	.5	1508	520	2011	4	VETO
C3t9	.7	1524	527	2529	3	-
C3t10	.15	1502	531	2531	6	-

Table B.9: The SN of all used electronic boards are shown. It is also shown were each TacQuila system is located and which Hex-Address the TRIPLEX has to have to fit into the TRIPLEX tree.

B.8.3 Used Material

In this section the 'names' of the used material will be mentioned, this might be useful if somebody in the future is looking e.g. for a certain connector for upgrades or maintenance of the system.

- connector for GTB-cable: `ERNI #024403 / SMCB 50F AB VV 3-01`,

- connector for TRIPLEX-cable: `ERNI #214346 / SMCB 26F AB VV 6-01`,

- connector for CLOCK-cable at Clock-Distr.: `LEMO / FF A.0S.302.CLAK 57`,

- connector for cable from TRIPLEX to QDC: `ODU 525.060.035.040.010`,

- connector for lv cable: `Phoenix FKC 2.5/10-ST-5,08-RF`,

- connector for 17th channel at SIS-Clock-Distr.: `LEMO / FGG.00.302.CLAD35`.

The different cable have the following length:

- GTB-cable to next neighbor: 15 cm,

- CLOCK-cable from CLOCK-Distr. to TacQuila: 90 cm,

- TRIPLEX-cable to next neighbor: 17 cm,

- TRIPLEX-cable to rest (e.g over next neighbor etc.): 32 cm,

- 17th-channel-cable from SIS-Clock-Distr. to TacQuila: 100 cm.

B.9   Known Issues

- Miscounting of clock cycle counter. This effect was correlated with an offset for the charge measurement as long as the QDC was un-gated, this effect is now unfortunately gone. The effect is rate dependend (here the rate on the FEE is important, not the trigger rate). This effect is still under investigation and not understood. An illustration of the problem is given in figure B.48. The amount of events which encounter this problem which was expected by the developers can be seen in figure B.50.

- QDC is not reset after the readout.

- As a consequence of the above mentioned point the chosen resistance (R) is important since it defines the disintegration-time, we did some tests using different resistances, but there is no final decision taken yet.

- Amplifier on FEE is in principle not needed if TacQuilas are used to readout a PMT which is coupled to a scintillator. A new FEE version is currently being developed.

- Energy measurement is missing if we do not have the time. Hakan's request for cross-triggering.

- At the edges of the TAC spectrum there is a non-linearity, see figure B.27 and figure B.49.

- At the moment the three cables used to connect the mother-clock to the daughter-clock modules do not have the same length, this adds of course a phase shift. Theoretically this should not create problems. However, it would be nice to keep the system as simple as possible, so this should be changed in the future.

- Change slow control from LabView to EPICS; use multiplexing at the moment only K. Koch knows how this works.

- Because +VV and -VV have been inverted the labeling and color code of the cables is here wrong. This has to be changed (capacitors have already been replaced).

- Write cabling documentation.

- `tacset.txt` contains two parameters which are not needed: threshold and generator, this causes only confusion.

- Heiko and Michael reported that the minimum for the clock cycle counter is 8. smaller values are not possible. could that be connected to the 8 clock cycles delay

between the trigger at the comparator on the FEE and the readout of the QDC? since this is also 8 cycles? maybe something went wrong in the FPGA code.

- A scaler for the 17th on the TacQuila board would be helpfull.

- Next version of TRIPLEX should be modified. Register addressing and baseline modifications can be done better.

- Sensing for lv distribution has to be implemented.
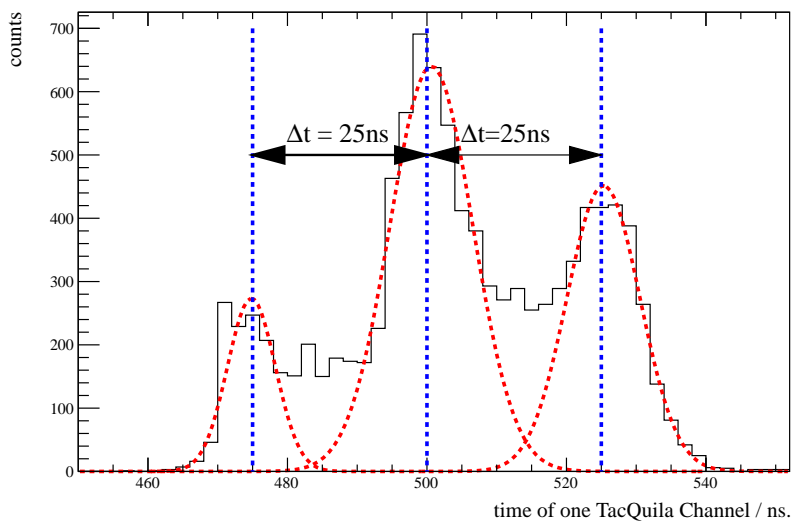
Figure B.48: Shown is the time of one LAND-PMT on SYNC level for a cosmic run taken during s394 (AsyEos). One would expect one broad peak, but two side peaks which are shifted by $\sim$25 ns (one clock cycle) are clearly visible.

145
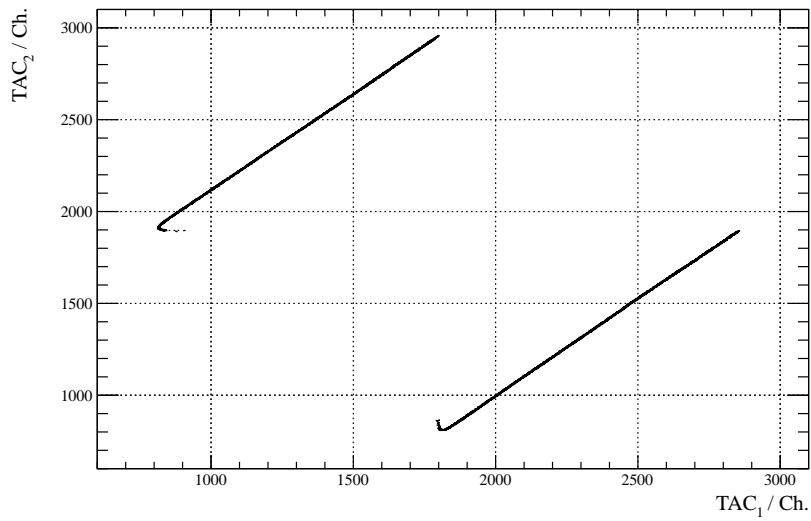
Figure B.49: Shown is a TAC_1 vs. TAC_2 spectrum for a TRIPLEX pulser measurement. The channels are on purpose chosen such that the delay is approximately half a clock cycle. The non-linearity at the edges are clearly visible. This bug is called 'hook'. The amount of events in the hook itself is smaller 1%, however, the range for which two correlations are visible is in the order of 1 ns, which is $\sim 4\%$ of the TAC range .
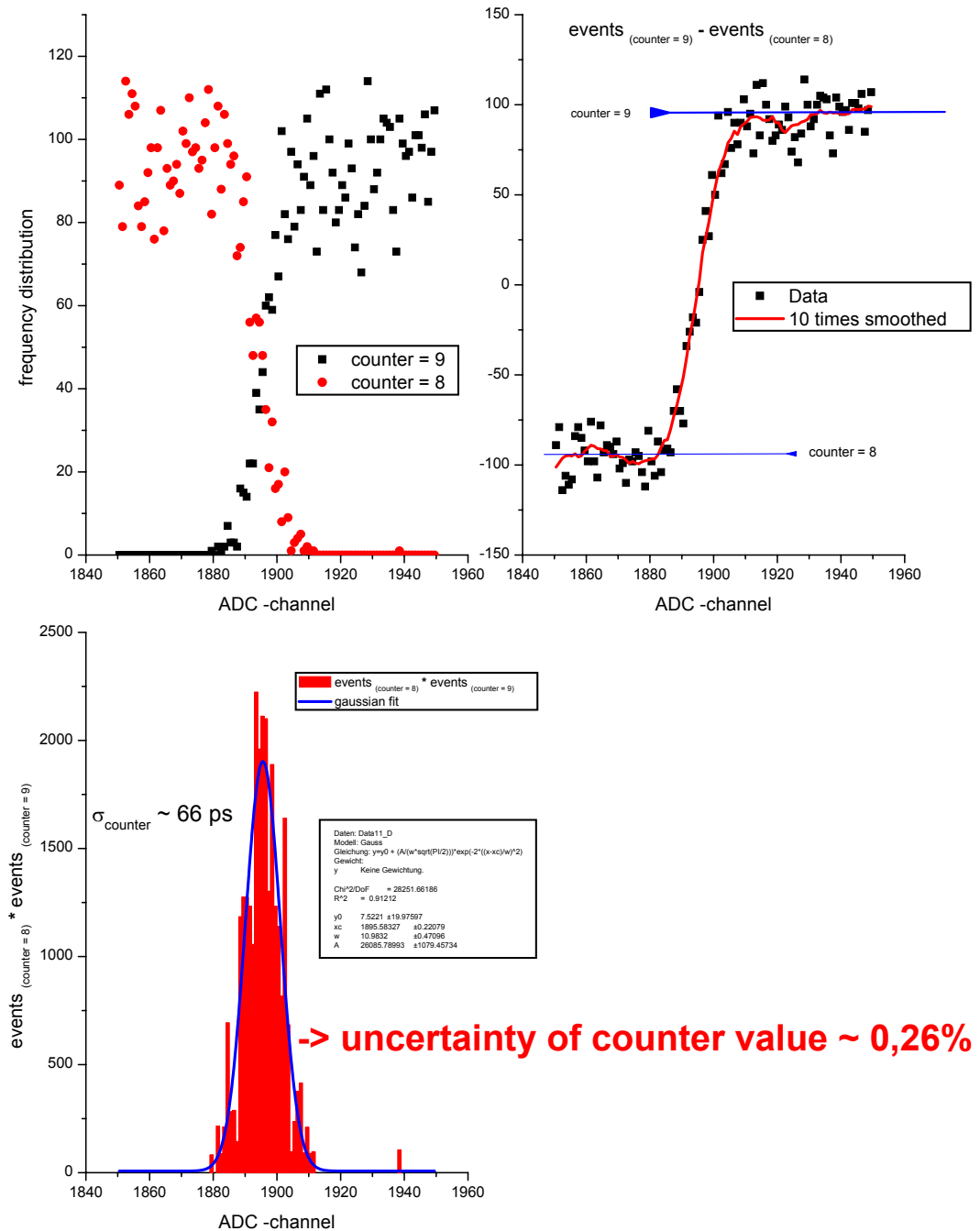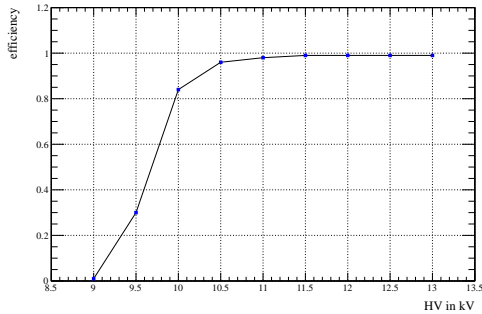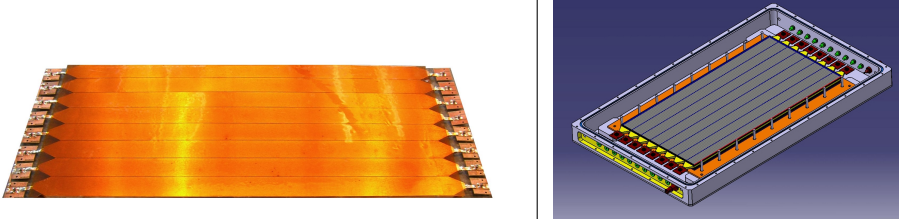
Figure B.50: Shown is the percentage which is expected by the developers for the amount of events which have a wrong clock counter.

Appendix C
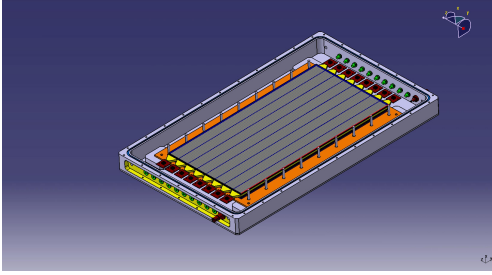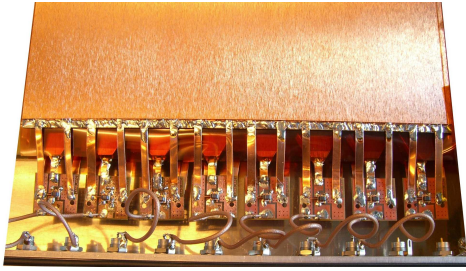
Data Sheets of MRPC Prototypes

prototype name	GSI-1
tested during	beam time @HZDR: 03/02/09 - 04/02/09
number of strips (structured anode)	8
anode strip width	25 mm
strip length	40 cm
active area	800 cm^2
number of gaps	2 · 4
gap size	0.3 mm
glass plate thickness	0.5 mm
HV	C layer on glass (Graphite Spray, OKS)
anode (iron/steel plate) thickness	4 mm
anode strip distance	0.3 mm (glue in between)
outer electrode thickness	2 mm

comments:

-four upper strips long, triangular strip-end which is not inside the active area, coupled with transformator.

-four lower strips short, rectangular shape two with transformator, one with resistances and one directly coupled to FEE

pictures:

results:

Note: at that time the HZDR DAQ could only read out 4 channels at the same time

time resolution:	≈85 ps
efficiency /voltage:	≈98 % @12kV (determined using scalers)
cross talk at n.n.:	≈96 %
amplitude of crosstalk:	≈54 %

prototype name	GSI-2
tested during	beam time @HZDR: 15/06/09 - 19/06/09
number of strips (structured anode)	8
anode strip width	25 mm
strip length	40 cm
active area	800 cm^2
number of gaps	$2 \cdot 4$
gap size	0.3 mm
glass plate thickness	0.5 mm
HV	Lycron Spray
anode (iron/steel plate) thickness	4 mm
anode strip distance	0.3 mm (gas in between)
outer electrode thickness	2 mm

comments:
-all 8 strips the same.
-longer than active area and with triangular strip end.
-all strips are coupled with transformator to readout.

pictures:

results:	
time resolution:	≈89 ps
efficiency /voltage:	≈83 % @6.75kV
cross talk at n.n.:	≈30 %
amplitude of crosstalk:	≈6 %

prototype name	GSI-3
tested during	beam time @HZDR: 15/06/09 - 19/06/09
number of strips (structured anode)	8
anode strip width	25 mm
strip length	40 cm
active area	800 cm^2
number of gaps	$2 \cdot 4$
gap size	0.3 mm
glass plate thickness	0.5 mm
HV	Lycron Spray
anode (iron/steel plate) thickness	4 mm
anode strip distance	0.6 mm (gas in between)
outer electrode thickness	2 mm

comments:

-all 8 strips the same.

-longer than active area and with triangular strip end.

-all strips are coupled with transformator to readout.

pictures:

results:	
time resolution:	$\approx$74 ps
efficiency /voltage:	$\approx$77 % @6.75kV
cross talk at n.n.:	$\approx$16 %
amplitude of crosstalk:	$\approx$5 %

prototype name	GSI-4
tested during	beam time @HZDR: 30/08/09 - 02/09/09
number of strips (structured anode)	8
anode strip width	25 mm
strip length	40 cm
active area	800 cm^2
number of gaps	2 · 4
gap size	0.3 mm
glass plate thickness	1.0 mm
HV	Lycron Spray
anode (iron/steel plate) thickness	4 mm
anode strip distance	0.3 mm (gas in between)
outer electrode thickness	2 mm

comments:
-all 8 strips the same.
-longer than active area and with triangular strip end.
-all strips are coupled with transformator to readout.

results:	
time resolution:	≈108 ps (problems with readout of right side)
efficiency /voltage:	≈97 % @ 12.0kV
cross talk at n.n.:	≈92 %
amplitude of crosstalk:	≈16 %

prototype name	GSI-5
tested during	beam time @HZDR: 30/08/09 - 02/09/09
number of strips (structured anode)	8
anode strip width	25 mm
strip length	40 cm
active area	800 cm^2
number of gaps	$2 \cdot 3$
gap size	0.3 mm
glass plate thickness	0.5 mm
HV	Europlex
anode (iron/steel plate) thickness	4 mm
anode strip distance	0.6 mm (gas in between)
outer electrode thickness	2 mm
comments: -all 8 strips the same. -longer than active area and with triangular strip end. -all strips are coupled with transformator to readout. -HV : last glass plate = Europlex, 2mm thick, conductive on both sides; R = 64 k.	
results:	
Due to problems with the HV the prototype never worked.	

prototype name	GSI-6
tested during	@TSL-Uppsala: 03/11/09 - 13/11/09
	@HZDR: 25/01/10 - 28/01/10
number of strips (structured anode)	8
anode strip width	25 mm
strip length	40 cm
active area	800 cm^2
number of gaps	2 · 4
gap size	0.3 mm
glass plate thickness	1.0 mm
HV	Lycron Spray
anode (iron/steel plate) thickness	4 mm
anode strip distance	1.0 mm (GFK material glued)
outer electrode thickness	2 mm

comments:
-all 8 strips the same.
-simplest solution, strip ends rectangular, no transformators.

pictures:

results:

Not analyzed yet.

prototype name	GSI-7
tested during	@TSL-Uppsala: 03/11/09 - 13/11/09
	@HZDR: 25/01/10 - 28/01/10
number of strips (structured anode)	8
anode strip width	25 mm
strip length	40 cm
active area	800 cm^2
number of gaps	2 · 4
gap size	0.3 mm
glass plate thickness	1.0 mm
HV	Lycron Spray
anode (iron/steel plate) thickness	4 mm
anode strip distance	0.6 mm (GFK material glued)
outer electrode thickness	2 mm
comments: -all 8 strips the same. -triangular strip ends rectangular, no transformators.	
pictures:	
results:	
Not analyzed yet.	

prototype name	GSI-8
tested during	@TSL-Uppsala: 03/11/09 - 13/11/09
	@HZDR: 25/01/10 - 28/01/10
number of strips (structured anode)	8
anode strip width	25 mm
strip length	40 cm
active area	800 cm^2
number of gaps	$2 \cdot 4$
gap size	0.3 mm
glass plate thickness	1.0 mm
HV	Lycron Spray
anode (iron/steel plate) thickness	4 mm
anode strip distance	1.0 mm (GFK material glued)
outer electrode thickness	2 mm
comments: -all 8 strips the same. -triangular strip ends rectangular, coupled transformators.	
pictures:	
results:	
For the analysis on this prototype see section 2.1 and ref. [CAB$^+$12]	

Appendix D

Acronyms

ADC	<u>A</u>nalog to <u>D</u>igital <u>C</u>onverter
ALADIN	<u>A</u> Large <u>A</u>cceptance <u>DI</u>pole mag<u>N</u>et
ATIMA	<u>AT</u>omic <u>I</u>nteraction with <u>MA</u>tter
a.u.	<u>a</u>rbitrary <u>u</u>nits
BANL	<u>BA</u>ker's <u>N</u>ominal <u>L</u>ikelihood
BAPL	<u>BA</u>ker's <u>P</u>oisson <u>L</u>ikelihood
BEPL	<u>BE</u>vington's <u>P</u>oisson <u>L</u>ikelihood
BuTiS	<u>Bu</u>nch-phase <u>Ti</u>ming <u>S</u>ystem
CALIFA	<u>CAL</u>orimeter for the <u>In</u> <u>F</u>light detection of γ rays and light charged p<u>A</u>rticles
CB	<u>C</u>rystal <u>B</u>all
clk	<u>cl</u>oc<u>k</u>
CPLD	<u>C</u>omplex <u>P</u>rogrammable <u>L</u>ogic <u>D</u>evice
DAC	<u>D</u>igital to <u>A</u>nalogue <u>C</u>onverter
DAQ	<u>D</u>ata <u>A</u>c<u>Q</u>uisition
DSSSD	<u>D</u>ouble <u>S</u>ided <u>S</u>ilicon <u>S</u>trip <u>D</u>etector
DTF	<u>D</u>icke (engl. thick) <u>T</u>ime of <u>F</u>light wall
ECL	<u>E</u>mitter <u>C</u>oupled <u>L</u>ogic
EE	<u>E</u>xperiment <u>E</u>lectronic Department
EFT	<u>E</u>ffective <u>F</u>ield <u>T</u>heory
ELBE	<u>E</u>lectron <u>L</u>inac for beams with high <u>B</u>rilliance and low <u>E</u>mittance
ENV	<u>E</u>CL <u>N</u>IM level converter embedded in a <u>V</u>ME-module
EPICS	<u>E</u>xperimental <u>P</u>hysics and <u>I</u>ndustrial <u>C</u>ontrol <u>S</u>ystem
ESPE	<u>E</u>ffective <u>S</u>ingle <u>P</u>article <u>E</u>nergy
FAIR	<u>F</u>acility for <u>A</u>ntiproton and <u>I</u>on <u>R</u>esearch
FaBu	<u>Fa</u>st <u>Bu</u>s (electronics), LeCroy digitizers
FEE	<u>F</u>ront <u>E</u>nd <u>E</u>lectronics

FLNR	Flerov Laboratory of Nuclear Reactions
FOPI	FOur PI experiment
FPGA	Field Programmable Gate Array
FRIB	Facility for Rare Isotope Beams
FRS	FRagment Seperator
GANIL	Grand Accélérateur National d'Ions Lourds
GEANT	GEometry ANd Tracking
GFI	Großer FIber detector, german for: 'large fibre detecor'
GLAD	GSI Large Acceptance Dipole
GND	GrouND; voltage connected to ground
GRP	Glass-fibre Reinforced Plastic
GSI	Gesellschaft für SchwerIonenforschung
GS	Ground State
GTB	GeräTeBus, engl. Device Bus
GUI	Graphical User Interface
HADSHOPOMO	HADes SHOwer POwer MOnitor
HGS-HIRe	Helmholtz Graduate School for Hadron and Ion Research
HV	High-Voltage
HZDR	Helmholtz-Zentrum Dresden-Rossendorf
I^{2}C	Inter-Integrated Circuit; is a multi-master serial single-ended computer bus
ICM	Ionization Chamber Monitor
IP	Internet Protocol
ISOL	Ion Source On Line
JINR	Joint Institute for Nuclear Research
KVI	Kernfysisch Versneller Instituut
LBNL	Lawrence Berkeley National Laboratory
LAND	Large Area Neutron Detector
LEG	LAND Event Generator
LEVCON	programmable LEVel CONverter
lmd	list mode data
lv	low voltage
LVTTL	Low Voltage Transistor-Transistor Logic
MBS	Multi Branch System; GSI Data AcQuisition software
MFP	Multi Function Peripheral
MRPC	Multi-gap Resisitve Plate Chamber
MSU	Michigan State University
Mul	Multiplicity
NeuLAND	Neu (engl. new) Large Area Neutron Detector. Successor of LAND

NDF	Number of Degree of Freedom
NIM	Nuclear Instrumentation Module standard
NSCL	National Superconducting Cyclotron Laboratory
NTF	New Time of Flight wall
NuSTAR	Nuclear STructure, Astrophysics and Reactions
PAW	Physics Analysis Workstation
PECL	Positive Emitter Coupled Logic
PhD	Philosophiae Doctor
PID	Particle IDentification
POS	POSition, detecor which is nowadays used for the incoming timing
PPC	Parallel Plate Chamber
PMT	Photo Multiplier Tube
PSP	Position Sensitive Pin-diode
QDC	charge (Q) to Digital Converter
R&D	Research & Development
R³B	Reactions with Relativistic Radioactive Beams
RIB	Radiactive Ion Beam
RIBF	Rare Isotope Beam Factory
RIPS	RIKEN Projectile Fragment Separator
RIKEN	The Institute of Physical and Chemical Research, japanese abbreviation
ROLU	Rechts Oben Links Unten, german for: right, up, left, down
RPC	Resistive Plate Chamber
SAM	Steuerungs und Auslese Modul, engl. Control and readout module
SEETRAM	SEcondary-Electron TRAnsmission Monitor
SINP	Saha Institute of Nuclear Physics
SIS	Schwer Ionen Synchrotron
SISSI	Superconducting Intense Source for Secondary Ions
SN	Serial Number
SPE	Single Particle Energy
SPIRAL	Système de Production d'Ions Radioactifs Accélérés en Ligne, in engl. System for Producing Online Accelerated Radioactive Ions
TAC	Time to Amplitude Converter
TDC	Time to Digital Converter; TDC = TAC+ADC
TFBC	Thin Film Breakdown Counters
TFW	Time of Flight Wall
ToF	Time of Flight
TRIDI	VME TRIgger DIstribution Module
TRIVA	VME TRIgger Synchronizing Module

TRLO	TRigger LOgic
TSL	The Svedberg Laboratory
TTL	Transistor-Transistor Logic
UCESB	Unpack and Check Every Single Bit
UNILAC	UNIversal Linear ACcelerator
VME	or VMEbus Versa Module Europe
VULOM	VME Universal LOgic Module
VV	Vor-Verstärker; engl. Preamplifier

Bibliography

[Aum05a] T. Aumann. Nuclear structure at the dripline. *Nuclear Physics A*, 752:289–298, April 2005.

[Aum05b] T. Aumann. Reactions with fast radioactive beams of neutron-rich nuclei. *European Physical Journal A*, 26:441–478, December 2005.

[Aum07] T. Aumann. Prospects of nuclear structure at the future GSI accelerators. *Progress in Particle and Nuclear Physics*, 59:3–21, July 2007.

[BAB$^+$07] T. Baumann, A. M. Amthor, D. Bazin, B. A. Brown, C. M. F. , III, A. Gade, T. N. Ginter, M. Hausmann, M. Matoš, D. J. Morrissey, M. Portillo, A. Schiller, B. M. Sherrill, A. Stolz, O. B. Tarasov, and M. Thoennessen. Discovery of ^{40}Mg and ^{42}Al suggests neutron drip-line slant towards heavier isotopes. *NATURE*, 449:1022–1024, October 2007.

[BC84] S. Baker and R.D. Cousins. Clarification of the use of CHI-square and likelihood functions in fits to histograms. *Nuclear Instruments and Methods in Physics Research*, 221:437–442, April 1984.

[BEE$^+$92] Th. Blaich, Th. W. Elze, H. Emling, H. Freiesleben, K. Grimm, W. Henning, R. Holzmann, G. Ickert, J. G. Keller, H. Klingler, W. Kneissl, R. König, R. Kulessa, J. V. Kratz, D. Lambrecht, J. S. Lange, Y. Leifels, E. Lubkiewicz, M. Proft, W. Prokopowicz, C. Schütter, R. Schmidt, H. Spies, K. Stelzer, J. Stroth, W. Walus, E. Wajda, H. J. Wollersheim, M. Zinser, and E. Zude. A large area detector for high-energy neutrons. *Nuclear Instruments and Methods in Physics Research Section A: Accelerators, Spectrometers, Detectors and Associated Equipment*, 314(1):136 – 154, 1992.

[BGI$^+$03] K. Boretzky, A. Grünschloß, S. Ilievski, P. Adrich, T. Aumann, C. A. Bertulani, J. Cub, W. Dostal, B. Eberlein, T. W. Elze, H. Emling, M. Fallot, J. Holeczek, R. Holzmann, C. Kozhuharov, J. V. Kratz, R. Kulessa, Y. Leifels, A. Leistenschneider, E. Lubkiewicz, S. Mordechai, T. Ohtsuki, P. Reiter, H. Simon, K. Stelzer, J. Stroth, K. Sümmerer, A. Surowiec, E. Wajda, and

W. Walus. Two-phonon giant resonances in ^{136}Xe, ^{208}Pb, and ^{238}U. *Physical Review C*, 68(2):024317, August 2003.

[BM69]   A. Bohr and B. R. Mottelson. *Nuclear Structure*, volume 1. W. A. Benjamin, New York, 1969.

[Bor11]   K. Boretzky. Technical Report for the Design, Construction and Commissioning of NeuLAND: The High-Resolution Neutron Time-of-Flight Spectrometer for R3B. private communication, 2011.

[BR69]   P.R. Bevington and D.K. Robinsons. *Data Reduction and Error Analysis for the Physical Sciences*. McGraw-Hill, New York, 2nd edition, 1969.

[BR05]   B. A. Brown and W. A. Richter. Magic numbers in the neutron-rich oxygen isotopes. *Physical Review C*, 72(5):057301, November 2005.

[BR06]   B. A. Brown and W. A. Richter. New "USD" Hamiltonians for the sd shell. *Physical Review C*, 74(3):034315, September 2006.

[BST12]   T. Baumann, A. Spyrou, and M. Thoennessen. Nuclear structure experiments along the neutron drip line. *Reports on Progress in Physics*, 75(3):036301, March 2012.

[CAB$^+$12]   C. Caesar, T. Aumann, D. Bemmerer, K. Boretzky, Z. Elekes, D. Gonzalez-Diaz, J. Hehner, M. Heil, M. Kempe, V. Maroussov, O. Nusair, R. Reifarth, D. Rossi, H. Simon, D. Stach, A. Wagner, D. Yakorev, and A. Zilges. NeuLAND MRPC-based detector prototypes tested with fast neutrons. *Nuclear Instruments and Methods in Physics Research Section A: Accelerators, Spectrometers, Detectors and Associated Equipment*, 661, Supplement 1(0):S145 – S148, 2012. X. Workshop on Resistive Plate Chambers and Related Detectors (RPC 2010).

[Cer]   Cern. ROOT. http://root.cern.ch/.

[CFA$^+$12a]   G. Christian, N. Frank, S. Ash, T. Baumann, D. Bazin, J. Brown, P. A. Deyoung, J. E. Finck, A. Gade, G. F. Grinyer, A. Grovom, J. D. Hinnefeld, E. M. Lunderberg, B. Luther, M. Mosby, S. Mosby, T. Nagi, G. F. Peaslee, W. F. Rogers, J. K. Smith, J. Snyder, A. Spyrou, M. J. Strongman, M. Thoennessen, M. Warren, D. Weisshaar, and A. Wersal. Exploring the Low-Z Shore of the Island of Inversion at N=19. *Physical Review Letters*, 108(3):032501, January 2012.

[CFA+12b] G. Christian, N. Frank, S. Ash, T. Baumann, P. A. Deyoung, J. E. Finck, A. Gade, G. F. Grinyer, B. Luther, M. Mosby, S. Mosby, J. K. Smith, J. Snyder, A. Spyrou, M. J. Strongman, M. Thoennessen, M. Warren, D. Weisshaar, and A. Wersal. Spectroscopy of neutron-unbound ^{27,28}F. *Physical Review C*, 85(3):034327, March 2012.

[Chu12] L. Chulkov. R-Matrix Theory. private communication, 2012.

[CSC+07] M. Ciobanu, A. Schuttauf, E. Cordier, N. Herrmann, K. D. Hildenbrand, Y. J. Kim, Y. Leifels, M. Marquardt, M. Kis, P. Koczon, X. Lopez, M. Petrovici, J. Weinert, and X. J. Zhang. A Front-End Electronics Card Comprising a High Gain/High Bandwidth Amplifier and a Fast Discriminator for Time-of-Flight Measurements. *IEEE Transactions on Nuclear Science*, 54:1201–1206, August 2007.

[CSdL88] R. Cardarelli, R. Santonico, A. di Biagio, and A. Lucci. Progress in resistive plate counters. *Nuclear Instruments and Methods in Physics Research A*, 263:20–25, January 1988.

[CSG+98] J. Cub, G. Stengel, A. Grünschloß, K. Boretzky, T. Aumann, W. Dostal, B. Eberlein, Th. W. Elze, H. Emling, G. Ickert, J. Holeczek, R. Holzmann, J. V. Kratz, R. Kulessa, Y. Leifels, H. Simon, K. Stelzer, J. Stroth, A. Surowiec, and E. Wajda. A large-area scintillating fibre detector for relativistic heavy ions. *Nuclear Instruments and Methods in Physics Research Section A: Accelerators, Spectrometers, Detectors and Associated Equipment*, 402(1):67 – 74, 1998.

[Ct05] J. C. Cornell and the SPIRAL Collaboration. Radioactive beam facilities in Europe: current status and future development. *eprint arXiv:nucl-ex/0501030*, January 2005.

[DAB+00] S. Dangtip, A. Ataç, B. Bergenwall, J. Blomgren, K. Elmgren, C. Johansson, J. Klug, N. Olsson, G. A. Carlsson, J. Söderberg, O. Jonsson, L. Nilsson, P.-U. Renberg, P. Nadel-Turonski, C. L. Brun, F.-R. Lecolley, J.-F. Lecolley, C. Varignon, P. Eudes, F. Haddad, M. Kerveno, T. Kirchner, and C. Lebrun. A facility for measurements of nuclear cross sections for fast neutron cancer therapy. *Nuclear Instruments and Methods in Physics Research A*, 452:484–504, October 2000.

[DB10] P. Descouvemont and D. Baye. The R-matrix theory. *Reports on Progress in Physics*, 73(3):036301, March 2010.

[Ebe98]   B. Eberlein. *Aufbruchreaktionen des Halo-Kerns* ^8He. PhD thesis, Johannes Gutenberg-Universität Mainz, Germany, 1998.

[EK03]   H.G. Essel and N. Kurz. GSI Multi-Branch System User Manual. http://web-docs.gsi.de/~mbs/v43/manual/gm_mbs_i.pdf, 2003.

[Ele09]   Z. Elekes. MRPC simulations. private communication, 2009.

[FS11]   B. Friman and A. Schwenk. Three-body interactions in Fermi systems. *ArXiv e-prints*, January 2011.

[GAB+92]   H. Geissel, P. Armbruster, K. H. Behr, A. Brünle, K. Burkard, M. Chen, H. Folger, B. Franczak, H. Keller, O. Klepper, B. Langenbeck, F. Nickel, E. Pfeng, M. Pfützner, E. Roeckl, K. Rykaczewski, I. Schall, D. Schardt, C. Scheidenberger, K. H. Schmidt, A. Schröter, T. Schwab, K. Sümmerer, M. Weber, G. Münzenberg, T. Brohm, H. G. Clerc, M. Fauerbach, J. J. Gaimard, A. Grewe, E. Hanelt, B. Knödler, M. Steiner, B. Voss, J. Weckenmann, C. Ziegler, A. Magel, H. Wollnik, J. P. Dufour, Y. Fujita, D. J. Vieira, and B. Sherrill. The GSI projectile fragment separator (FRS): a versatile magnetic system for relativistic heavy ions. *Nuclear Instruments and Methods in Physics Research Section B: Beam Interactions with Materials and Atoms*, 70(1-4):286 – 297, 1992.

[GJK+90]   D. Guillemaud-Mueller, J. C. Jacmart, E. Kashy, A. Latimier, A. C. Mueller, F. Pougheon, A. Richard, Y. E. Penionzhkevich, A. G. Artuhk, A. V. Belozyorov, S. M. Lukyanov, R. Anne, P. Bricault, C. Détraz, M. Lewitowicz, Y. Zhang, Y. S. Lyutostansky, M. V. Zverev, D. Bazin, and W. D. Schmidt-Ott. Particle stability of the isotopes ^{26}O and ^{32}Ne in the reaction 44 MeV/nucleon ^{48}Ca+Ta. *Physical Review C*, 41:937–941, March 1990.

[GMSZ11]   L. V. Grigorenko, I. G. Mukha, C. Scheidenberger, and M. V. Zhukov. Two-neutron radioactivity and four-nucleon emission from exotic nuclei. *Physical Review C*, 84(2):021303, August 2011.

[Gon06]   González-Díaz, D. *Research and Developments on Timing RPCs. Application to the ESTRELA Detector of the HADES Experiment at GSI.* PhD thesis, University of Santiago de Compostela, Spain, 2006.

[HBB+08]   C. R. Hoffman, T. Baumann, D. Bazin, J. Brown, G. Christian, P. A. Deyoung, J. E. Finck, N. Frank, J. Hinnefeld, R. Howes, P. Mears, E. Mosby, S. Mosby, J. Reith, B. Rizzo, W. F. Rogers, G. Peaslee, W. A. Peters, A. Schiller, M. J. Scott, S. L. Tabor, M. Thoennessen, P. J. Voss, and

T. Williams. Determination of the N=16 Shell Closure at the Oxygen Drip Line. *Physical Review Letters*, 100(15):152502, April 2008.

[HBB⁺09] C. R. Hoffman, T. Baumann, D. Bazin, J. Brown, G. Christian, D. H. Denby, P. A. Deyoung, J. E. Finck, N. Frank, J. Hinnefeld, S. Mosby, W. A. Peters, W. F. Rogers, A. Schiller, A. Spyrou, M. J. Scott, S. L. Tabor, M. Thoennessen, and P. Voss. Evidence for a doubly magic ^{24}O. *Physics Letters B*, 672:17–21, February 2009.

[HBB⁺11] C. R. Hoffman, T. Baumann, J. Brown, P. A. Deyoung, J. E. Finck, N. Frank, J. D. Hinnefeld, S. Mosby, W. A. Peters, W. F. Rogers, A. Schiller, J. Snyder, A. Spyrou, S. L. Tabor, and M. Thoennessen. Observation of a two-neutron cascade from a resonance in ^{24}O. *Physical Review C*, 83(3):031303, March 2011.

[Hol12] J. Holt. Theoretical calculations for neutron-rich oxygen isotopes using 'nn+3n' interactions. private communication, 2012.

[HV11] M. Heine and V. Volkov. Photogrammetry. private communication, 2011.

[Jam] F. James. http://wwwasd.web.cern.ch/wwwasd/cernlib/mc/genbod.html.

[Jan09] Robert V. F. Janssens. NUCLEAR PHYSICS Unexpected doubly magic nucleus. *NATURE*, 459(7250):1069–1070, JUN 25 2009.

[Joh06] H. T. Johansson. The DAQ always runs. Master's thesis, Chalmers University of Technology, Göteborg, Sweden, 2006.

[Joh10] H. T. Johansson. *Hunting Tools Beyond the Driplines*. PhD thesis, Chalmers University of Technology, Göteborg, Sweden, 2010.

[JPST01] R.K Jain, A.V Prokofiev, A.N Smirnov, and L Tommasino. Measurement of high energy neutrons by fission reactions. *Radiation Measurements*, 34:129 – 132, 2001. Proceedings of the 20th International Conference on Nuclear Tracks in Solids.

[JSH49] J. H. D. Jensen, H. E. Sueß, and O. Haxel. Modellmäßige Deutung der ansgezeichneten Nucleonenzahlen im Kernbau. *Naturwissenschaften*, 36:155–156, May 1949.

[KHS⁺05] K. Koch, H. Hardel, R. Schulze, E. Badura, and J. Hoffmann. A New TAC-Based Multichannel Front-End Electronics for TOF Experiments With Very High Time Resolution. *IEEE Transactions on Nuclear Science*, 52:745–747, June 2005.

[Kie81]   J. Kieffer. A Modular Stand-Alone Monitor and Control System (Samac). *IEEE Transactions on Nuclear Science, vol. 28, issue 1, pp. 646-650*, 28:646–650, 1981.

[KM91]   J.G. Keller and E.F. Moore. Shower Recognition and Particle Identication in LAND. GSI Scientic Report 1991, p39, Darmstadt, 1992, 1991.

[KNP+09]   R. Kanungo, C. Nociforo, A. Prochazka, T. Aumann, D. Boutin, D. Cortina-Gil, B. Davids, M. Diakaki, F. Farinon, H. Geissel, R. Gernhäuser, J. Gerl, R. Janik, B. Jonson, B. Kindler, R. Knöbel, R. Krücken, M. Lantz, H. Lenske, Y. Litvinov, B. Lommel, K. Mahata, P. Maierbeck, A. Musumarra, T. Nilsson, T. Otsuka, C. Perro, C. Scheidenberger, B. Sitar, P. Strmen, B. Sun, I. Szarka, I. Tanihata, Y. Utsuno, H. Weick, and M. Winkler. One-Neutron Removal Measurement Reveals ^{24}O as a New Doubly Magic Nucleus. *Physical Review Letters*, 102(15):152501, April 2009.

[Lan12]   C. Langer. *Coulomb Dissociation of ^{31}Cl and ^{32}Ar - constraining the rp process.* PhD thesis, Johann Wolfgang Goethe-Universität Frankfurt am Main, Germany, 2012.

[LB09]   T. Le Bleis. *Experimental Study of Collective Electric Dipole Mode in Neutron-Rich Nickel Nuclei.* PhD thesis, University of Strasbourg, France, 2009.

[LDK+12]   E. Lunderberg, P. A. DeYoung, Z. Kohley, H. Attanayake, T. Baumann, D. Bazin, G. Christian, D. Divaratne, S. M. Grimes, A. Haagsma, J. E. Finck, N. Frank, B. Luther, S. Mosby, T. Nagi, G. F. Peaslee, A. Schiller, J. Snyder, A. Spyrou, M. J. Strongman, and M. Thoennessen. Evidence for the ground-state resonance of ^{26}**O**. *Phys. Rev. Lett.*, 108:142503, Apr 2012.

[Lei97]   A. Leistenschneider. Entwicklung eines Schauererkennungsalgorithmus für den Neutronendetektor-LAND. Master's thesis, Johann Wolfgang Goethe-Universität Frankfurt am Main, Germany, 1997.

[Lei11]   Y. Leifels. LAND shower algorithm. private communication, 2011.

[LQB+85]   M. Langevin, E. Quiniou, M. Bernas, J. Galin, J. C. Jacmart, F. Naulin, F. Pougheon, R. Anne, C. Détraz, D. Guerreau, D. Guillemaud-Mueller, and A. C. Mueller. Production of neutron-rich nuclei at the limits of particles stability by fragmentation of 44 MeV/u ^{40}Ar projectiles. *Physics Letters B*, 150:71–74, January 1985.

[LT58]   A. M. Lane and R. G. Thomas. R-Matrix Theory of Nuclear Reactions. *Reviews of Modern Physics*, 30:257–353, April 1958.

[May48]   M. G. Mayer. On Closed Shells in Nuclei. *Physical Review*, 74:235–239, August 1948.

[MJP⁺09]   K. Mahata, H.T. Johansson, S. Paschalis, H. Simon, and T. Aumann. Position reconstruction in large-area scintillating fibre detectors. *Nuclear Instruments and Methods in Physics Research Section A: Accelerators, Spectrometers, Detectors and Associated Equipment*, 608(2):331 – 335, 2009.

[NC]   NuSTAR-Collaboration. Nustar proposals. http://www-linux.gsi.de/∼wwwnusta/tech_report/.

[OSH⁺10]   T. Otsuka, T. Suzuki, J. D. Holt, A. Schwenk, and Y. Akaishi. Three-Body Forces and the Limit of Oxygen Isotopes. *Physical Review Letters*, 105(3):032501, July 2010.

[OST01]   A. Ozawa, T. Suzuki, and I. Tanihata. Nuclear size and related topics. *Nuclear Physics A*, 693:32–62, October 2001.

[OUF⁺02]   T Otsuka, Y Utsuno, R Fujimoto, BA Brown, M Honma, and T Mizusaki. Frontiers and challenges of nuclear shell model. *EUROPEAN PHYSICAL JOURNAL A*, 15(1-2):151–155, SEP-OCT 2002. 3rd International Conference on Exotic Nuclei and Atomic Masses, HAMEENLINNA, FINLAND, JUL 02-07, 2001.

[Pan12]   V. Panin. *Fully Exclusive Measurements of Quasi-Free Single-Nucleon Knock-out Reactions in Inverse Kinematics*. PhD thesis, Technische Universität Darmstadt, Germany, 2012.

[PBB⁺07]   A. V. Prokofiev, J. Blomgren, O. Bystrom, C. Ekstrom, S. Pomp, U. Tippawan, V. Ziemann, and M. Osterlund. The TSL neutron beam facility. *RADIATION PROTECTION DOSIMETRY*, 126(1-4):18–22, 2007. 10th International Symposium on Neutron Dosimetry, Uppsala, SWEDEN, JUN 12-16, 2006.

[PBL⁺12]   P. Pawlowski, J. Brzychczyk, Y. Leifels, W. Trautmann, P. Adrich, T. Aumann, C. O. Bacri, T. Barczyk, R. Bassini, S. Bianchin, C. Boiano, K. Boretzky, A. Boudard, A. Chbihi, J. Cibor, B. Czech, M. De Napoli, J.-E. Ducret, H. Emling, J. D. Frankland, T. Gorbinet, M. Hellström, D. Henzlova, S. Hlavac, J. Immè, I. Iori, H. Johansson, K. Kezzar, S. Kupny, A. Lafriakh, A. Le Fèvre, E. Le Gentil, S. Leray, J. Łukasik, J. Lühning, W. G. Lynch, U. Lynen, Z. Majka, M. Mocko, W. F. J. Müller, A. Mykulyak, H. Orth, A. N. Otte, R. Palit, S. Panebianco, A. Pullia, G. Raciti, E. Rapisarda, D. Rossi, M.-D. Salsac, H. Sann, C. Schwarz, H. Simon, C. Sfienti, K. Sümmerer, M. B.

Tsang, G. Verde, M. Veselsky, C. Volant, M. Wallace, H. Weick, J. Wiechula, A. Wieloch, and B. Zwiegliński. Neutron recognition in LAND detector for large neutron multiplicity. *eprint arXiv:1203.5608*, March 2012.

[PKGR12] M. Pfützner, M. Karny, L. V. Grigorenko, and K. Riisager. Radioactive decays at limits of nuclear stability. *Reviews of Modern Physics*, 84:567–619, April 2012.

[PPP71] V. V. Parkhomchuck, Y. N. Pestov, and N. V. Petrovykh. A spark counter with large area. *Nuclear Instruments and Methods*, 93:269, 1971.

[RCa] R3B-Collaboration. Direct reactions of light exotic beams measured in complete kinematics at R3B. http://gsi.de/informationen/wti/library/scientificreport2010/ PAPERS/PHN-NUSTAR-NR-04.pdf.

[RCb] R3B-Collaboration. Technical Proposal for the Design, Construction, Commissioning and Operation of R3B A universal setup for kinematical complete measurements of Reactions with Relativistic Radioactive Beams. http://www.gsi.de/forschung/kp/kr/R3B/Technical Proposal.pdf.

[Ros09] D. M. Rossi. *Investigation of the Dipole Response of Nickel Isotopes in the Presence of a High-Frequency Electromagnetic Field.* PhD thesis, Johannes Gutenberg-Universität Mainz, Germany, 2009.

[Ros11] D. Rossi. LAND calibration and reconstruction. private communication, 2011.

[SC81] R. Santonico and R. Cardarelli. Development of resistive plate counters. *Nuclear Instruments and Methods in Physics Research*, 187(2-3):377 – 380, 1981.

[Sch11] H. Scheit. Experimentelle Untersuchungen der Kernstruktur weitab der Stabilität. Vortrag im physikalischen Kolloquium der TU Darmstadt, 2011.

[Sch12a] A. Schwenk. Neutron-rich matter in the laboratory and the cosmos. Vortrag, DPG-Frühjahrstagung Mainz 2012, 2012.

[Sch12b] A. Schwenk. Theoretical calculations for neutron-rich oxygen isotopes including three body forces. private communication, 2012.

[Sim11] H. Simon. LAND calibration and reconstruction. private communication, 2011.

[Sim12] J. Simonis. Theoretical calculations for neutron-rich oxygen isotopes using 'nn+3nres' interactions. private communication, 2012.

[SLN+99] H. Sakurai, S. M. Lukyanov, M. Notani, N. Aoi, D. Beaumel, N. Fukuda, M. Hirai, E. Ideguchi, N. Imai, M. Ishihara, H. Iwasaki, T. Kubo, K. Kusaka, H. Kumagai, T. Nakamura, H. Ogawa, Y. E. Penionzhkevich, T. Teranishi, Y. X. Watanabe, K. Yoneda, and A. Yoshida. Evidence for particle stability of ^{31}F and particle instability of ^{25}N and ^{28}O. *Physics Letters B*, 448:180–184, February 1999.

[TAA+97] O. Tarasov, R. Allatt, J. C. Angélique, R. Anne, C. Borcea, Z. Dlouhy, C. Donzaud, S. Grévy, D. Guillemaud-Mueller, M. Lewitowicz, S. Lukyanov, A. C. Mueller, F. Nowacki, Y. Oganessian, N. A. Orr, A. N. Ostrowski, R. D. Page, Y. Penionzhkevich, F. Pougheon, A. Reed, M. G. Saint-Laurent, W. Schwab, E. Sokol, O. Sorlin, W. Trinder, and J. S. Winfield. Search for ^{28}O and study of neutron-rich nuclei near the N = 20 shell closure. *Physics Letters B*, 409:64–70, February 1997.

[TS11] Michael Thoennessen and Bradley Sherrill. From isotopes to the stars. *NATURE*, 473(7345):25–26, MAY 5 2011.

[UOMH99] Y. Utsuno, T. Otsuka, T. Mizusaki, and M. Honma. Varying shell gap and deformation in N∼20 unstable nuclei studied by the Monte Carlo shell model. *Physical Review C*, 60(5):054315, November 1999.

[Vog08] E. Vogt. The Early Days of R-Matrix Theory. http://www.jinaweb.org/events/azura08/talks/Vogt-The Early Days of R-Matrix Theory.pdf, 2008.

[VZ06] A. Volya and V. Zelevinsky. Continuum shell model. *Physical Review C*, 74(6):064314, December 2006.

[Wam11] F. Wamers. *Quasi-Free-Scattering and One-Proton-Removal Reactions with the Proton-Dripline Nucleus ^{17}Ne at Relativistic Beam Energies*. PhD thesis, Technische Universität Darmstadt, Germany, 2011.

[Wei] H. Weick. Atima. http://www-linux.gsi.de/∼weick/atima/.

[YAB+11] D. Yakorev, T. Aumann, D. Bemmerer, K. Boretzky, C. Caesar, M. Ciobanu, T. Cowan, Z. Elekes, M. Elvers, D. Gonzalez Diaz, R. Hannaske, J. Hehner, M. Heil, M. Kempe, V. Maroussov, O. Nusair, H. Simon, M. Sobiella, D. Stach, A. Wagner, A. Zilges, and R3B Collaboration. Prototyping and tests for an MRPC-based time-of-flight detector for 1 GeV neutrons. *Nuclear Instruments and Methods in Physics Research A*, 654:79–87, October 2011.

171

[YBR12] D. Yakorev, D. Bemmerer, and RB Collaboration. Work on a large-area MRPC-based time-of-flight detector for high energy neutrons. *Journal of Physics Conference Series*, 337(1):012035, February 2012.

[ZHN⁺97] M. Zinser, F. Humbert, T. Nilsson, W. Schwab, H. Simon, T. Aumann, M. J. G. Borge, L. V. Chulkov, J. Cub, T. W. Elze, H. Emling, H. Geissel, D. Guillemaud-Mueller, P. G. Hansen, R. Holzmann, H. Irnich, B. Jonson, J. V. Kratz, R. Kulessa, Y. Leifels, H. Lenske, A. Magel, A. C. Mueller, G. Münzenberg, F. Nickel, G. Nyman, A. Richter, K. Riisager, C. Scheidenberger, G. Schrieder, K. Stelzer, J. Stroth, A. Surowiec, O. Tengblad, E. Wajda, and E. Zude. Invariant-mass spectroscopy of ^{10}Li and ^{11}Li. *Nuclear Physics A*, 619:151–176, February 1997.

Acknowledgement

Physics is becoming so unbelievably complex that it is taking longer and longer to train a physicist. It is taking so long, in fact, to train a physicist to the place where he understands the nature of physical problems that he is already too old to solve them.

<div align="right">Eugene Wigner</div>

I don't want to argue with Wigner of course and i certainly still know very little, but I guess the complexer the subject the better the teachers should be. So the following paragraph is devoted to those who contributed in different ways to my education during the last ~ten years and helped me with my first steps in the complex world of (nuclear) physics, of course in particular during the last time as a PhD student. Either directly by teaching me physics and related things or indirectly by being supportive and encouraging and making me believe that it is always worth to continue learning.

The work presented in this document would not have been possible without the help, guidance and support of many other people, so first of all i would like to thank all those who contributed to the success of this work. Particular i would like to thank my supervisor Prof. Dr. Thomas Aumann for giving me the opportunity to join his research group at GSI and TU Darmstadt, for being always enthusiastic, giving me confidence that nice physics results can be extracted and all the long discussions about the analysis. Many thanks also to my second referee(s). Being first enrolled at University of Mainz the second referee was Prof. Dr. Frank Maas. Thanks a lot for all the nice PhD-Committee-Meetings and for giving valuable input to this work. Changing the University to TU Darmstadt Prof. Dr. Joachim Enders accepted to be second referee for my thesis, thanks a lot for this. Thanks for the interest in the thesis, the good supervision and all the advises also on bureaucratic issues.

Many thanks go also to HGS-HIRe for offering a scholarship, lecture weeks and giving

Lebenslauf

Name:	Christoph Caesar
Adresse:	Lortzingstraße 3, 64546 Mörfelden
Geburtsdatum:	05. Dezember 1982
Geburtsort:	Mainz, Deutschland
Staatsangehörigkeit:	deutsch
Familienstand:	verheiratet

<u>Schule</u>

1989-1993:	Friedrich-von-Schiller-Grundschule, Wiesbaden
1993-1999:	Gerhart-Hauptmann-Gymnasium, Wiesbaden
1999-2002:	Carl-von-Ossietzky-Oberstufengymnasium, Wiesbaden
06/2002:	Abitur, Gesamtnote: 2.1

<u>Zivildienst</u>

2002-2003:	MSHD/Deutsches Rotes Kreuz, Kreisverband Wiesbaden E. V.

<u>Universität</u>

2003-2005:	Grundstudium Dipl. Physik (Johannes-Gutenberg-Universität-Mainz)
04/2005	Vordiplom, Note: gut
2005	Begin des Hauptstudiums Dipl. Physik
09/2006-01/2007	Praktikum am National Superconducting Cyclotron Laboratory (NSCL) der Michigan State University (MSU), Michigan, USA
09/2007	mündliche Diplom-Prüfung, Note: sehr gut
01/2008-10/2008	Aufenthalt am NSCL zur Anfertigung der Diplomarbeit
12/2008	Diplom Physik, Gesamt-Note: sehr gut
Seit 01/2009	Promotion in der AG Aumann; TU Darmstadt/GSI

Eidesstattliche Erklärung

Hiermit erkläre ich, dass ich die vorliegende Dissertation selbständig verfasst, keine anderen als die angegebenen Hilfsmittel verwendet und bisher noch keinen Promotionsversuch unternommen habe.

<div align="right">

Christoph Caesar;

Darmstadt, im Juli 2012

</div>